



**FREE AND HINDERED-ROTATION OF
HELIUM EXCIMERS IN LIQUID HELIUM VIA
A BULK EXPERIMENT**

by

Luis Guillermo Mendoza Luna (M.Sc.)

Thesis submitted for the degree of
Doctor of Philosophy
at the University of Leicester

Condensed Matter Physics Group
Department of Physics and Astronomy
University of Leicester

July 2015

Acknowledgments

First and foremost I thank my Family for their constant support throughout my whole academic career: their unconditional love has always been my main motivation in life.

I thank the Mexican Consejo Nacional de Ciencia y Tecnología (CONACYT) for sponsoring me with a gorgeous, highly-coveted scholarship that is a real privilege amongst Mexican students. It enabled me to fulfil my lifelong goal of pursuing a PhD abroad; now it has come the time for me to honor the promise I have made upon accepting the sponsorship and return home and work to the best of my capabilities for the development of Mexican science and the shaping of a country well-suited to the challenges of the 21st century.

I acknowledge the enormous contribution to my education made by the Universidad Nacional Autónoma de México; their efforts and commitment in providing the Mexican people with a high-standard education have not been in vain. Among the many people involved in that undertaking, I am most grateful for the support given to me by Dr Patricia Goldstein Menache, Dr María de los Ángeles Ortiz Flores, Dr Fernando Matías Moreno Yntriago and Dr Rosa María Méndez Vargas, to whom I also thank for endorsing my scholarship application.

I dearly thank Javier Medina and Caroline Berry for their warm and welcoming attitude to me upon my arrival in the United Kingdom.

I also acknowledge the University of Leicester, its Physics Department and the Condensed Matter Group for taking me on as a graduate student. Thanks to my supervisor Dr Klaus von Haeften for his trust in giving me the opportunity to join his research group and his advice throughout this course. I also thank Dr Mark Watkins and Stuart Thornton for their help and the lessons they delivered along with their assistance. I acknowledge fellow PhD students Michael McNally for useful discussions and Nagham Shiltagh for her assistance during the final phase of experimentation in my project. Many thanks to Andrew Underhill, Nick Boldra and Phil Stapleton from the Mechanical Workshop of the Physics Department and Nick Dorsey from the Electrical Support Laboratory for their patience and their continued technical support of my project. I acknowledge Phil Worth, Nigel Fisher and Kiri Humphreys for their clerical support and Cleo Bowen and the Erasmus program for

funding for traveling to Grenoble, France in order to further my training.

I acknowledge the Space Research Centre and the late Dr George Fraser for granting me access to their premises towards the completion of my project; thanks to Dr Jonathan Lapington for his support during my experimentation. I am especially indebted to Robert Limpenny for his assistance in vacuum and cryogenics; without it, my project would have suffered heavily and its successful completion would have been at stake; I also thank him for his proofreading of relevant sections of this work. I acknowledge the assistance provided by Dr Gauthier Torricelli and his teaching me the use of the Heliox fridge. Also thank Dr Tim Foster from Oxford Instruments for his technical support.

I deeply appreciate the friendship I struck up with Dr Virgil Taillandier, for which I can only say: *Merci beacoup!* Also I do thank the generosity of Ms Idah Mapako and her family towards me.

Special thanks to Dr Fred Aitken for his Mathematica program to reproduce the phase diagram of ^4He and to Dr Nelly Bonifaci for her software to simulate the transition of interest of this work and to both for useful discussions.

This work is dedicated to the memory of Manuel Adrián Meza Ríos and María de los Ángeles Ortiz Flores.

Abstract

Free and hindered-rotation of helium excimers in liquid helium via a bulk experiment

Luis Guillermo Mendoza Luna

Superfluidity is a many-body quantum effect observed for the first time in liquid helium. In the context of modern nanoscience, a natural question is whether superfluidity exists at the nanoscale and if so, under what conditions it occurs.

Superfluidity can be probed by means of a torsional pendulum immersed in liquid helium: a decrease in the moment of inertia of the pendulum was observed during the superfluid transition. By replacing the torsional pendulum with a carbonyl sulfide molecule embedded in helium droplets, Grebenev and coworkers explored superfluidity at the nanoscale. They established that 60 ^4He atoms is the threshold to observe superfluidity.

The thermodynamic conditions necessary for this transition could not be ascertained in Grebenev's work since in the helium droplet technique the transition into the superfluid state is impossible to control. One possible way around this experimental limitation is to perform a bulk experiment and embed short-lived helium excimers because all other molecules would freeze. The excimers are in Rydberg states and emit fluorescence sensitive to their environment.

In this work, helium excimers have been produced in bulk liquid helium using corona discharges. A wide range of the phase diagram of helium has been probed via fluorescence spectroscopy of Rydberg excimers for the first time: molecular transitions in gaseous, supercritical, vapor and normal liquid phases have been studied systematically. Depending on the thermodynamic conditions, sharp as well as broadened spectra have been observed. The linewidths and lineshifts of a transition of interest have been interpreted on the basis of a model that considers emission from two kinds of excimer: on the one hand, excimers embedded in voids and fully solvated in liquid helium exhibiting hindered rotation, and on the other hand, excimers residing in larger gas pockets within the liquid helium, exhibiting free rotation. The relative contributions of each species of excimer have been estimated in a ratio of approximately 1:5. Hindered transitions were identified for pressures and temperatures in the vapor phase, before helium liquefies. These points in the phase diagram

show the formation of clusters between excimers and ground-state helium atoms, indicating that the He_2^* -He interaction is stronger than that of He-He.

Contents

1	Introduction	1
1.1	Helium and superfluidity: the two fluid model	1
1.2	The Andronikashvili experiment	4
1.3	The problem of free rotations in superfluids and non-superfluids . . .	4
1.4	Spectroscopy of excimers in liquid helium	7
1.5	Relevance of this work	8
1.6	Objectives	8
2	Methodology and theory	11
2.1	Need to control He-molecule interaction	11
2.2	Matrix isolation spectroscopy	11
2.3	Generation of electronic excitations in bulk helium	12
2.3.1	Features of a high density discharge	13
2.4	Previous experiments using the corona discharge method	14
2.5	Quantum mechanics of a diatomic molecule	14
2.6	Electronic structure of diatomic molecules	20
2.6.1	Vibrations	21
2.6.2	Rotations	21
2.7	Classification of electronic states and multiplet structure	21
2.8	Coupling of rotations and electronic motion and Hund's coupling cases	22
2.8.1	Hund's coupling case (b)	23
2.8.2	Hund's coupling case (d)	23
2.9	Excimers	24
2.9.1	Formation of excimers	24
2.9.2	Electronic structure of helium excimers	25
2.9.3	Electronic structure of the transition of interest	27
2.10	Excimers in liquid helium	29
2.11	Snowballs and cavities in liquid helium	30
3	Overview: setup of a new experiment	33
3.1	Radiation minimization	33

3.1.1	Estimation of the radiation heat load	34
3.2	Convection minimization and pumping system	34
3.3	Conduction minimization	35
3.3.1	Heatsinking and cryogenic cables	35
3.3.2	Calculation of the heat contribution via conduction due to a temperature gradient	36
3.3.3	Thermal conductivity of materials at low temperatures	38
3.3.4	Joule heating contribution	38
3.4	Total heat transfer rate into the setup	39
3.5	Wet and mechanical refrigerators	39
3.6	Heliox AC-V He-3 refrigerator	40
3.6.1	Operation of the Heliox AC-V He-3 refrigerator	41
3.7	General layout of the experiment	41
3.8	Cryogenic spark cell	42
3.9	Optical layout	44
3.10	Gas installation	46
3.11	Thermometer and pressure transducer	48
3.12	Electrical layout	48
3.13	Preparation of the tip	49
3.14	Assembly of the setup	49
3.14.1	Assembly of the spark cell	49
3.14.2	Assembly of the rest of the setup	50
3.15	Experimental procedure	51
3.16	Methodology of the data collection	54
4	Results and discussion	57
4.1	Experimental history	57
4.1.1	Experiment from 22-May-2014	57
4.1.2	Supercritical gas phase data	58
4.1.3	Liquid phase data	58
4.1.4	80 K data	59
4.2	Treatment of the spectra	59
4.3	Glow discharge calibration spectra and normalization	61
4.3.1	Line positions of the molecular transition of interest	63
4.4	Gas-phase experiments	63
4.5	Supercritical phase	65
4.6	Subcritical phase (gas and normal liquid helium)	66
4.7	Linewidth versus pressure	73
4.8	Line-shift versus pressure	76

4.9	Error determination in this experiment	80
4.10	Structural model and discussion	82
4.10.1	Formation of clusters	82
4.10.2	Linewidth and lineshift revisited	83
4.10.3	Simulation of the different contributions to the spectra	84
4.10.4	Distribution and localization of energy in a corona discharge in cryogenic helium	87
4.10.5	Rotational constants	87
5	Conclusions and outlook	88
	Appendices	90
A	Operation of the pumping station	91
B	Operation of the Heliox AC-V refrigerator	93
C	Atomic and molecular transitions of helium	94
D	Densities of liquid helium	95
E	Relevant physical constants and helium parameters	96
F	Shell-scripts and software	97
F.1	Script for normalization	97
F.2	Script for recalibration	99
F.3	Simulation of the spectrum	100
G	High-Voltage monitor	115
H	Tip after the experiments	117
I	NX designs and technical drawings	118

List of Figures

1.1	Schematic diagram of an interparticle potential for matrix species in Table 1.1.	2
1.2	Phase diagram of ^4He	3
1.3	The two-densities that arise from Landau's two-fluid model.	3
1.4	Andronikashvili's torsional pendulum immersed into He-II.	4
1.5	Summary of Grebenev's results.	5
1.6	Infrared spectra of OCS.	6
1.7	$d^3\Sigma_u^+ \rightarrow b^3\Pi_g$ (0-0) and $D^1\Sigma_u^+ \rightarrow B^1\Pi_g$ (0-0) transitions observed from emission via electron-bombarded dense gas at 150 torr (0.200 bar) and 4.2 K (panel(a)) and liquid helium at 1.7 K (panel (b)) by Dennis and coworkers.	8
1.8	Rotationally-resolved $b^3\Pi_g \leftarrow a^3\Sigma_u^+$ (0-0) absorption spectrum observed in electron-bombarded liquid helium.	9
1.9	Zhiling Li and coworkers' results.	9
2.1	Plane-tip electrode configuration.	13
2.2	Hund's case (b).	23
2.3	Hund's case (d).	24
2.4	Potential energy curves for states of He_2	26
2.5	Schematic energy levels of $^3\Sigma$ state as per Hund's coupling case (b).	27
2.6	Schematic energy levels of $^3\Pi$ state.	28
2.7	Structure of the $d^3\Sigma_u^+ \rightarrow b^3\Pi_g$ transition.	28
2.8	Emission spectrum of electron-bombarded liquid helium by Dennis and coworkers.	29
2.9	Schematic diagram of a He_2^* excimer enclosed in a bubble, characterized by a sharp interface between He_2^* and ground state He.	30
2.10	Schematic diagram of a He_2 excimer embedded in a gaseous environment.	31
2.11	Model of a He^+ snowball.	31
2.12	Schematic diagram of an electron bubble	32
3.1	Schematic diagram of the pumping station utilized in this experiment.	35

3.2	Thermal conductivities of different materials in the cryogenic regime.	39
3.3	Schematic diagram of the fridge utilized in this experiment.	41
3.4	Heliox AC-V refrigerator sending light into the spectrometer via mirrors and a lens.	42
3.5	Physical implementation of the plane-tip electrode array.	43
3.6	Cross-sectional view of the discharge region of the cell (assembled).	44
3.7	Schematic diagram of the optical system designed to couple the discharge light out of the vacuum chamber in the experiment.	45
3.8	Cross-sectional view of the cryogenic setup and physical realization of the system sketched in Fig. 3.7.	45
3.9	Top view of the light path.	46
3.10	Schematic diagram of the gas installation.	47
3.11	Electric diagram of the experiment.	48
3.12	Assembled cryostat.	52
3.13	Final stage of the alignment procedure in the cryogenic regime (3.5 K).	53
3.14	Section of the PT diagram for the liquid and supercritical phases probed in this experiment.	56
4.1	Recalibrated wavelength versus row number in the glow discharge spectrum from 6-Jun-2014.	60
4.2	Fit of spectrum 4 from 22-Sept-2014 ($T = 3.8$ K, $P = 2.30$ bar) by Fityk.	61
4.3	Overview of a normalized and calibrated glow discharge spectrum.	62
4.4	Overview of the spectra for the 80 K isotherm.	64
4.5	Development of the $d^3\Sigma_u^+ \rightarrow b^3\Pi_g$ (0-0) transition as a function of pressure for the 80 K isotherm.	64
4.6	Supercritical data points from Fig. 3.14.	65
4.7	Development of the $d^3\Sigma_u^+ \rightarrow b^3\Pi_g$ (0-0) transition as a function of pressure for the 16 K isotherm.	66
4.8	Points from Fig. 3.14 that correspond to the subcritical phase of helium (which includes either normal liquid or vapor).	67
4.9	Typical emission spectrum in the cryogenic regime.	69
4.10	Development of the $d^3\Sigma_u^+ \rightarrow b^3\Pi_g$ (0-0) transition as a function of pressure for the 3.8, 4 K and 5 K isotherms.	70
4.11	Zoom-in of the Q-branch and P(2) of Fig. 4.10.	71
4.12	$D^1\Sigma_u^+ \rightarrow B^1\Pi_g$ (0-0) transition observed in the luminescence spectrum of ^3He (top panel) and ^4He (bottom panel) droplets.	73
4.13	Linewidth of the P- rotational lines for isotherms in different phases of helium.	74

4.14	Linewidth of the P- rotational lines for 5.2, 16 and 80 K isotherms as a function of the number density.	75
4.15	Linewidth of the P- rotational lines for selected isotherms below the critical point of helium.	75
4.16	Linewidth of the Q-branch for isotherms in various thermodynamic states of helium as a function of pressure.	76
4.17	Comparison of the line broadening of P- and Q- rotational lines for 3.8, 4, 5, 16 and 80 K for Q- and P-branches.	77
4.18	Line-shift of the Q-branch for isotherms in the 5 K- 80 K temperature bracket as a function of pressure.	78
4.19	Line-shift of the Q-branch (top panel) and P-lines (bottom panel) for isotherms in the 3.8 K- 5 K interval as a function of pressure.	79
4.20	Hypothesized phase diagram for the excimer-helium mixed system.	80
4.21	Results of the simulation of the transition of interest for representative temperatures and pressures.	86
D.1	Reported densities of helium in the normal liquid and vapor regimes.	95
G.1	Electric diagram of the HV monitor designed by Nick Dorsey.	115
G.2	Additional shunt resistor and voltmeter to measure the current in our setup.	116
H.1	Top view of the tungsten tip recorded with the FIB technique.	117

Chapter 1

Introduction

1.1 Helium and superfluidity: the two fluid model

Helium is a fully quantum-mechanical substance due to the weak interaction between helium atoms and their light mass [105]. One of the manifestations of the quantum character of helium is the existence of different phase diagrams for its two different isotopes [119].

In order to understand why helium is markedly quantum-mechanical while other noble gases are classical in comparison we turn our attention to the inter-particle helium-helium potential in a helium matrix. See Fig. 1.1 for an example of such a typical curve. It is characterized by a potential well depth (ϵ) and a well minimum position (R_m); both parameters for ^3He and ^4He are much smaller than the corresponding parameters for other species (like Xe, Kr, Ar). Cf. Table 1.1.

Matrix species	ϵ (K)	R_m (\AA)	α (\AA^3)	Λ^*	V_0/R_0^3	T_{tp} (K)
Xe	283	4.37	4.01	0.06	0.933	161
Kr	201	4.01	2.48	0.11	0.951	116
Ar	143	3.76	1.64	0.20	0.976	83.8
Ne	43.3	3.09	0.397	0.62	1.09	24.6
H ₂	34.8	3.44	0.803	1.97	1.32	14.0
^4He	11.0	2.97	0.205	2.87	1.87	no t.p.
^3He	11.0	2.97	0.205	3.31	2.82	no t.p.

Table 1.1: Comparison of different properties of common matrix materials. α is the dipole polarizability, Λ^* is the de Boer parameter [105], V_0/R_0^3 is the ratio of the measured volume per atom at $T = 0$ K and the volume expected for a classical solid, T_{tp} is the triple-point temperature. This Table corresponds to Table 1 reproduced from [105].

Helium is the only substance that remains liquid at absolute zero; this effect is attributed to helium's large zero point energy and the concomitant delocalization of its wavefunction. At 0.4 K the thermal de Broglie wavelength [69] of ^4He (defined

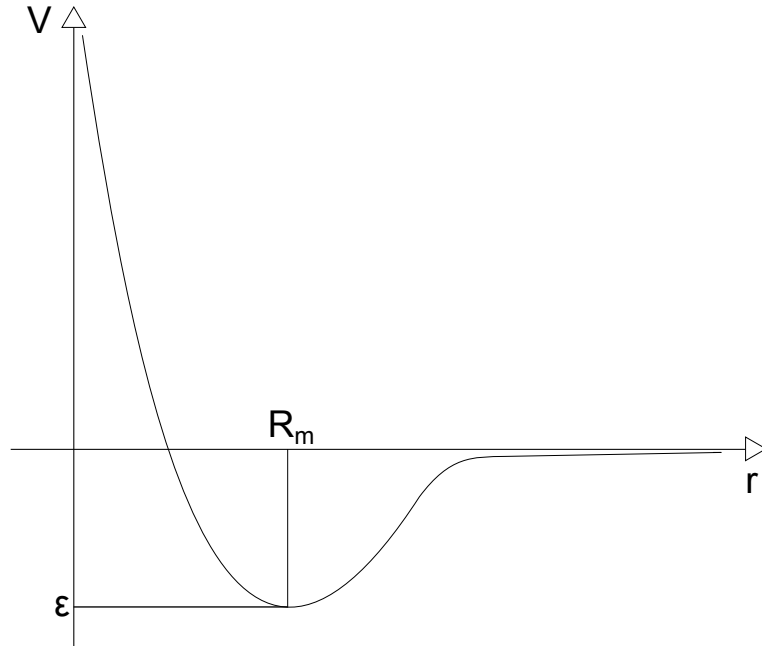


Figure 1.1: Schematic diagram of an interparticle potential for matrix species in Table 1.1.

as $h/\sqrt{2\pi m_{\text{He}} k_B T}$ is 13.8 Å, greater than the internuclear separation (3.56 Å). See Table E.1 in Appendix E.

Another remarkable manifestation of the quantum character of helium is superfluidity, discovered in the late 1930's by Kapitza [66]. Superfluidity is a many-body quantum effect; its most distinctive features are the frictionless flow of the superfluid, a very high heat conductivity, the fountain effect¹ and quantized vortices [30]. ³He and ⁴He are the best known substances that display superfluidity although Bose-Einstein condensates (BEC's) and sections of neutron stars are known to display superfluid properties as well [60, 89, 20].

The highest temperature at which superfluidity occurs is designated the lambda-temperature T_λ (see Table E.1 in Appendix E); differences in the superfluid character of the different helium isotopes arise because they obey different spin statistics. Liquid helium below the lambda point is usually called He-II.

In order to account for the observed superfluidity effects, Tisza put forward the idea of separating the density of He-II into two parts using two velocity distributions [104]. Landau then proposed an accurate quantitative description of superfluid dynamics: He-II behaves like a mixture of two fluids, one normal and the other superfluid (that is, with no friction) [77, 76]; in more precise terms it could be said that He-II exhibits two different flows, one which corresponds to a regular viscous fluid and the other one to a superfluid, with no momentum transfer between them

¹The fountain effect consists of an upward flow through an open-ended capillary embedded in superfluid liquid helium upon heating the helium by means of a coil inside a bulb [11].

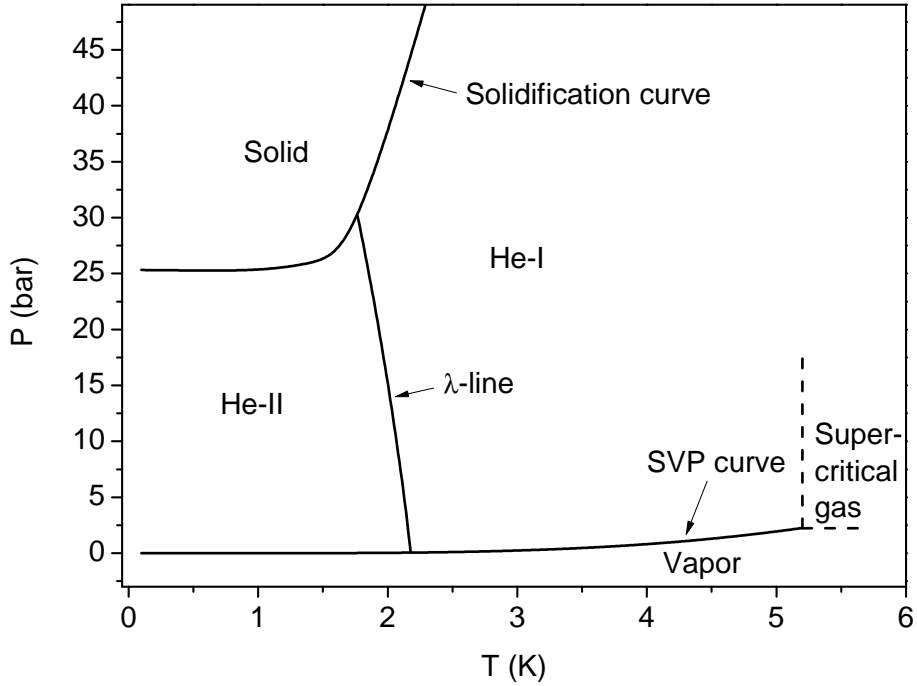


Figure 1.2: Phase diagram of ${}^4\text{He}$. He-I corresponds to the normal liquid helium and He-II designates superfluid liquid helium. This diagram was produced utilizing empirical formulas by Dr F. Aitken [6].

[78]. Cf. [64] for a comparison between the approaches of Tisza and Landau on the two-fluid model.

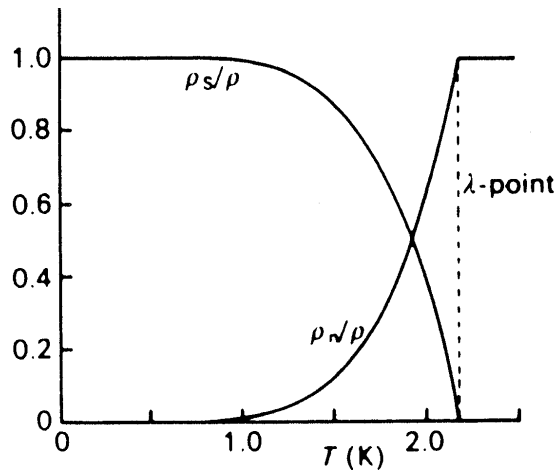


Figure 1.3: The two-densities that arise from Landau's two-fluid model. For any temperature it can be seen that the sum of the different densities is constant. The superfluid fraction shows a strong temperature dependence between 1 K and the λ -point of helium. Figure taken from [49].

1.2 The Andronikashvili experiment

One of the most striking confirmations of the two-fluid model was provided by Andronikashvili as early as 1946 [12, 13].

In his experiment a torsional pendulum was immersed into He-II (see Figure 1.4); Andronikashvili observed that the moment of inertia of the disks decreased sharply upon reduction of the temperature below T_λ .

This experiment can be explained using the two-fluid model: if He-II possesses a superfluid component then it can account for the missing moment of inertia (the decrease in the moment of inertia of the pendulum means that the superfluid fraction is not contributing to the moment of inertia).

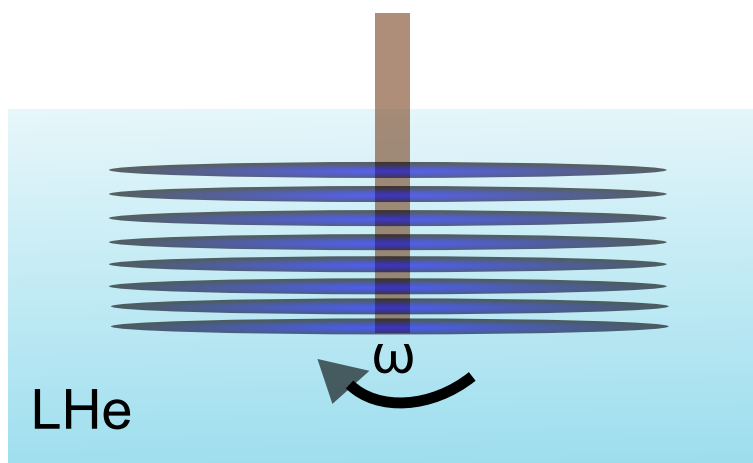


Figure 1.4: Andronikashvili's torsional pendulum immersed into He-II.

1.3 The problem of free rotations in superfluids and non-superfluids

Experiments have been carried out where single molecules have been embedded into He clusters of various sizes [46, 33, 53, 54, 51, 48, 100]. The rotational motion of molecules can be assessed and interpreted using the formalism of Matrix Isolation Spectroscopy (MIS)². In short, these experiments consist of a supersonic expansion of helium through a μm -diameter nozzle at large stagnation pressures and cryogenic temperatures. Helium condenses into clusters of different sizes depending on the conditions of the nozzle. Then, the clusters capture molecules. The molecule-cluster complex can then be ionized and probed using lasers via depletion spectroscopy³ [45].

²See Section 2.2.

³In molecular beams signals are usually too weak to be detected by measuring absorption via transmission of an incident light signal. Depletion spectroscopy methods look at the variation of a different parameter, for example the depletion of molecular beam energy, to assess the magnitude of absorption of light by particles in the beam.

In 1992 the group of Scoles attempted to measure the infrared spectrum of sulfur hexafluoride (SF_6) in helium droplets at high-resolution and using a line-tunable CO_2 laser but was unable to resolve the spectrum [46]; a couple of years later, using SF_6 molecules attached to large ^4He droplets, the group of J. P. Toennies repeated the experiment with a continuously tunable diode laser and found that the ν_3 vibrational band⁴ of SF_6 displayed a sharp rotational structure [33], which was interpreted as a signature of free rotation. By fitting a free-particle Hamiltonian with a rotational temperature of 0.37 K it was found that the moment of inertia of the molecule had increased by a factor of 2.8 with respect to the free molecule [53]. Today it is established that the increase of the effective moment of inertia is due to nonsuperfluid density [75], emerging from the interaction of the molecule with the helium bath. This non-superfluid density follows the rotation of the molecule, increasing its effective moment of inertia and thereby increasing the linewidth of the associated spectral lines. The symmetry of the molecule appears not to be affected.

For high rotational speeds this model is not applicable [86]. Also the magnitude and nature of the observed line broadening are not very well understood. Interaction between rotations and collective excitations such as rotons [52] and phonons [111] have been discussed.

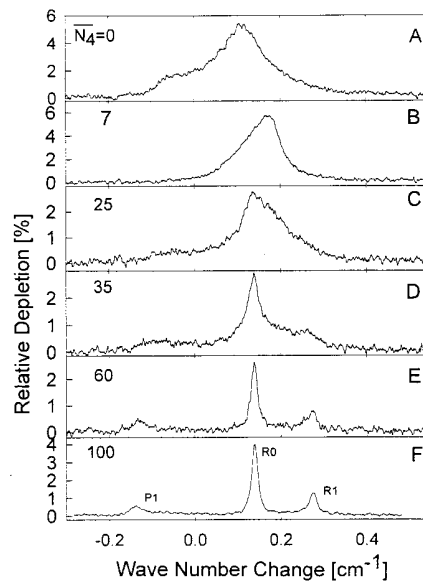


Figure 1.5: Summary of Grebenev's results. The different panels from top to bottom indicate the average number of added ^4He atoms added to a ^3He droplet from 0 (top panel) through 100 (bottom panel). As can be seen from panel E, upon addition of 60 ^4He atoms, the droplet acquires rotational resolution. Figure reproduced from Fig. 2 of [48].

To test for the possibility of a superfluid environment in the He droplets, an

⁴Cf. footnote 4 of Chapter 4 of [61]

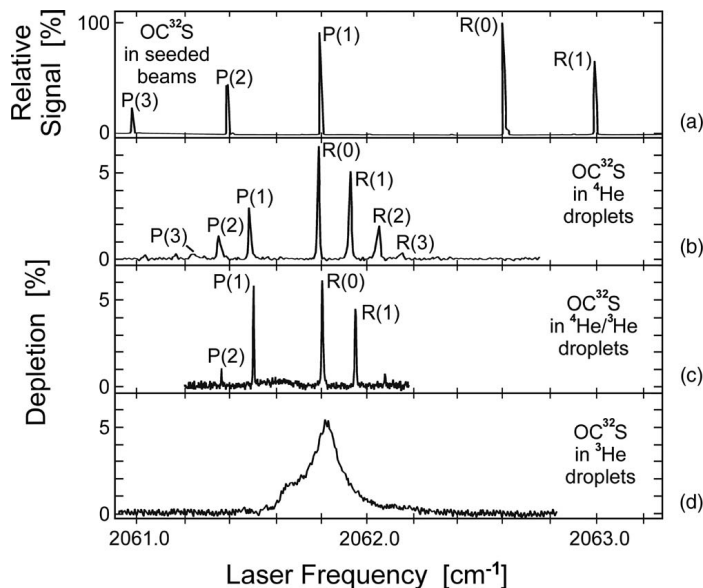


Figure 1.6: Infrared spectra of OCS. In panel (a) an Ar seeded beam was used; in (b) the size of the droplet is approximately 3×10^3 atoms; in (c) the size of the mixture is approximately 10^3 ^4He atoms and 10^4 ^3He atoms; in (d) the size of the droplet is about 12×10^3 . Figure reproduced from Fig. 1 of [94]. Experiments of OCS in mixed ^3He - ^4He show that the linewidth changes from 0.3 K to 0.15 K and hence the temperature is important for the structure of the normal liquid layer around OCS.

infrared absorption experiment with carbonyl sulfide (OCS) molecules was carried out in isotopically-selected helium droplets in 1998 [48]. The IR absorption spectrum of OCS embedded in pure ^4He droplets was measured and it was observed that it exhibits sharp rotational lines. In contrast, OCS within pure ^3He droplets displays a featureless, broadened spectrum which was interpreted as the OCS not rotating freely within the droplet; this interpretation was attributed to a normal liquid state which is justified by the fact that the rotational temperature of ^3He droplets is 0.15 K [51], very well above T_λ for ^3He . Furthermore, experiments with mixed ^3He - ^4He droplets were performed. Upon increase of the number of ^4He atoms in the mixed droplets attached to the OCS- ^3He droplet, changes in the absorption spectrum were observed and at about 60 atoms a sharp spectrum was recovered, leading Grebenev *et al.* to establish 60 atoms as the onset of superfluidity (See Fig. 1.5). It was also found that the observed sharp spectra can again be fitted with a free-rotor Hamiltonian with a rotational constant 2.7 times larger than the free molecule and a rotational temperature of 0.37 K.

The experiments with mixed ^3He - ^4He droplets also showed different linewidths of OCS in pure ^4He (at 0.44 K) and mixed ^3He - ^4He (at 0.15 K) droplets, suggesting that the temperature affected the coupling of the rotating molecule to the superfluid helium.

The foregoing discussion is summarized in Table 1.2, where a direct comparison

of the approaches explained above is explicitly made.

Andronikashvili's experiment	Molecule in He_n/liquid He
Macroscopic	Microscopic
Two-fluid model	Interface large compared to rotor; hence, local two-fluid model
Observable: torsional frequency	Observable: Infrared spectra (MIS)

Table 1.2: Comparison between Andronikashvili's and the molecular probe approaches.

1.4 Spectroscopy of excimers in liquid helium

An excimer is a diatomic molecule with one of its two atoms in an excited electronic state [21]. The term excimer is limited to cases in which both components are the same atom. The term exciplex refers to the both components being different atoms; however, in common usage excimer covers both situations.

Excimers live only for limited time, typically on the nanosecond timescale [31]. They often emit a fluorescence spectrum that is sensitive to the environment [28, 109]. $n = 3$ He₂^{*} excimers have a lifetime of tens of nanoseconds [88, 91], where n represents the principal quantum number of the state.

A bulk experiment would be most convenient for exploring superfluidity in the microscopic scale because temperature and pressure can be changed; controlling both thermodynamical parameters has an obvious effect on the phase of helium but modifying the temperature, in particular, allows control over the nonsuperfluid phase of helium.

The spectroscopy of excimers in liquid helium has been studied before by other authors and bore divergent results, as shall be seen below.

Dennis and coworkers have observed, in an electron-excited beam impinging upon liquid helium, rotationally unresolved emission in the liquid phase pertaining to the $d^3\Sigma_u^+ \rightarrow b^3\Pi_g$ (0-0) and $D^1\Sigma_u^+ \rightarrow B^1\Pi_g$ (0-0) molecular transitions of helium (see Fig. 1.7).

In an analogous experiment, Hill *et al.* (see Fig. 1.8) observed a rotationally resolved absorption spectrum for the $b^3\Pi_g \leftarrow a^3\Sigma_u^+$ (0-0) transition. Similarly, but this time in an emission experiment, Li and coworkers working with liquid helium probed via excimers generated by corona discharge excitations observed a rotationally resolved spectrum for the same transitions studied by Dennis (see Fig. 1.9). Two questions arise as to why in Dennis' experiment no rotational resolution is observed but in Hill's and Li's it is and also why no changes in the rotational constants

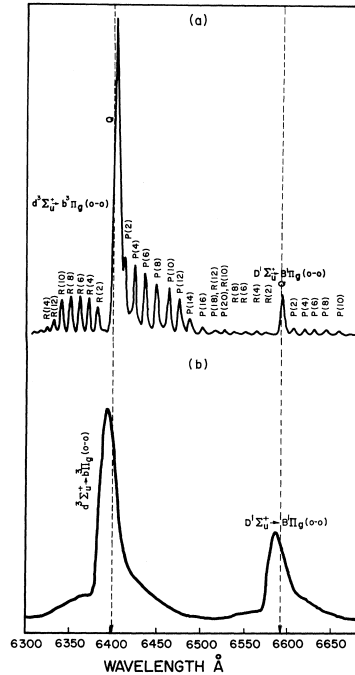


Figure 1.7: $d^3\Sigma_u^+ \rightarrow b^3\Pi_g$ (0-0) and $D^1\Sigma_u^+ \rightarrow B^1\Pi_g$ (0-0) transitions observed from emission via electron-bombarded dense gas at 150 torr (0.200 bar) and 4.2 K (panel(a)) and liquid helium at 1.7 K (panel (b)) by Dennis and coworkers. Reproduced from Fig. 3 of [28].

of helium were observed. The present work aims to address the aforementioned shortcomings in the literature.

1.5 Relevance of this work

The understanding of molecular rotations plays a major role in the study of the interactions of matter. This work furthers the understanding of the interaction between molecular rotation and a gaseous, liquid or solid environment. The purpose of this research is to investigate the microscopic origin and other microscopic manifestations of superfluidity (such as the onset of superfluidity), sometimes called nanosuperfluidity, which is customarily understood as the almost unhindered rotation of molecules [105, 74].

1.6 Objectives

The purpose of this PhD thesis is to answer the following questions:

- Why 60 ^4He atoms are needed to make OCS rotate freely?
- How can we explain the rotational line broadening in superfluid helium?

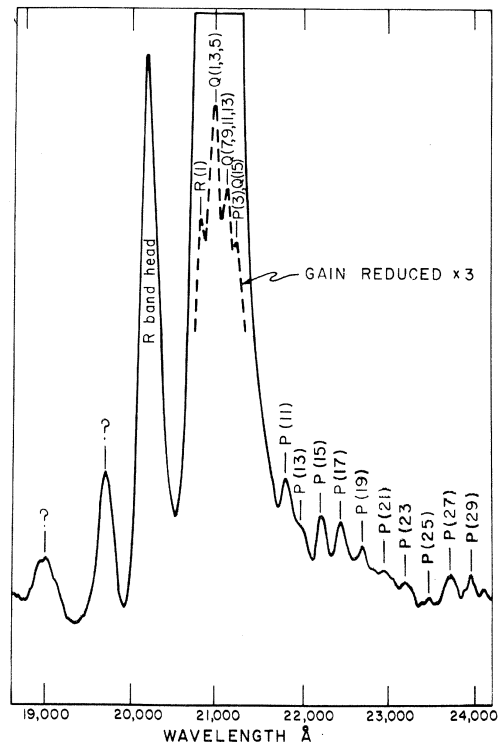


Figure 1.8: Rotationally-resolved $b^3\Pi_g \leftarrow a^3\Sigma_u^+$ (0-0) absorption spectrum observed in electron-bombarded liquid helium. Reproduced from Fig. 1 of [58].

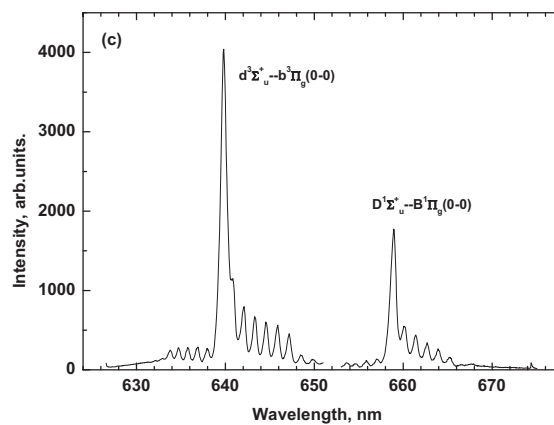


Figure 1.9: Zhiling Li and coworkers' results. Fluorescence spectrum recorded from corona discharge emission in liquid helium at 4.2 K and 1 bar. Plot taken from Fig. 1 of [81].

- Can we control the interaction between a molecule and helium by changing the pressure and temperature?
- Is it possible to observe a change in the rotational constants as a function of the interaction between excimer and environment?
- Clarify why previous experiments in bulk helium show sharp lines or broad features.

Chapter 2

Methodology and theory

2.1 Need to control He-molecule interaction

A way to further the understanding of the microscopic manifestations of superfluidity is to perform a “microscopic” Andronikashvili experiment using a nanoscale rotor in the form of a molecule. The most straightforward realization of this program is an experiment where a species (like SF₆ or OCS in the helium-droplet experiments) is deposited directly into bulk liquid helium. This cannot be done, though, because any foreign particles in liquid helium will condense at the container walls or agglomerate to clusters due to the low temperature.

A solution to this problem is the helium-droplet method. However, in a helium-droplet experiment the temperature of molecules embedded in the cluster is fixed. From the two-fluid model, superfluidity properties depend on the temperature and pressure of the helium. Hence, in order to understand nanosuperfluidity it is necessary to control the thermodynamic state of the molecule and the helium-droplet technique turns out not to be suitable for this purpose. Being able to modify at will the pressure and temperature of the helium means that the average distance between the probes (via pressure) and their kinetic energy (via temperature) can be controlled.

In the following sections a methodology for carrying out this experimental program will be outlined. In what follows a “*” means an excited state of either an atomic or a molecular species.

2.2 Matrix isolation spectroscopy

Embedding and isolating a molecule in a solid matrix was first done with the purpose of investigating properties of single molecules. This conceptual and experimental framework came to be known as Matrix Isolation Spectroscopy [116].

The embedding operation carried the unwanted effect of creating an interaction between host and guest. While the research in the past was primarily devoted to gain a better understanding of the host, it implicitly had to address the nature of this interaction as well. However, the solute-matrix interactions can be brought into the spotlight and become the object of study; matrix isolation spectroscopy can then be thought of as a technique to study the interaction of a single solute and a matrix. This was possible in practice due to the appearance of molecular cluster beam machines, allowing to embed single molecules into clusters, the availability of proper lasers and the invention of adequate detection techniques.

Rare-gas atoms have been demonstrated as convenient environments for the experimental realization of such matrices [105, 45]. An early example of the influence of a matrix environment on a molecule embedded in it was the observed changes in the spectrum of SF₆ due to its positioning at the surface of argon clusters [44].

One of the modern research applications of helium is its use as a liquid-helium matrix in the form of droplets flying in a molecular beam [105]. The work by Scoles and coworkers is inscribed in this framework [46]; they were among the first to embed a foreign molecule into helium clusters.

The examples cited above show that changes in an emission/absorption spectrum with respect to pure/gas-phase benchmarks are indicative of an interaction with the environment. The work on molecules embedded onto the surface of argon clusters showed differences with respect to the gas phase and the bulk spectrum, reflecting the changes of structure at the molecule-matrix interface. Hence, upon addition of a molecule into a matrix (or, more generally, an environment), one can either use the molecule as a probe of properties of the matrix or investigate phenomena at the molecule-matrix interface, i.e. interactions. Both viewpoints are adopted in this work to investigate properties of superfluidity at the nanoscale.

2.3 Generation of electronic excitations in bulk helium

In order to circumvent the problems mentioned above we have used an electrical discharge called corona discharge to continuously generate excited helium atoms (He*) and excited helium molecules (He₂*, and sometimes called excimers) in Rydberg states [87], which will be employed as molecular probes [82, 80]. This choice is motivated by the fact that excimers decay on a nanosecond time scale so they are not affected by condensation.

2.3.1 Features of a high density discharge

A key feature of corona discharges is that they can be ignited at high pressures (densities) [42]. A popular geometry of a corona discharge consists of a tip and a plane electrode with cylindrical symmetry separated out by a certain distance and typically embedded in a fluid [115]. See Fig. 2.1. The problem of calculating the electric field of such a setup can be treated exactly [80, 26].

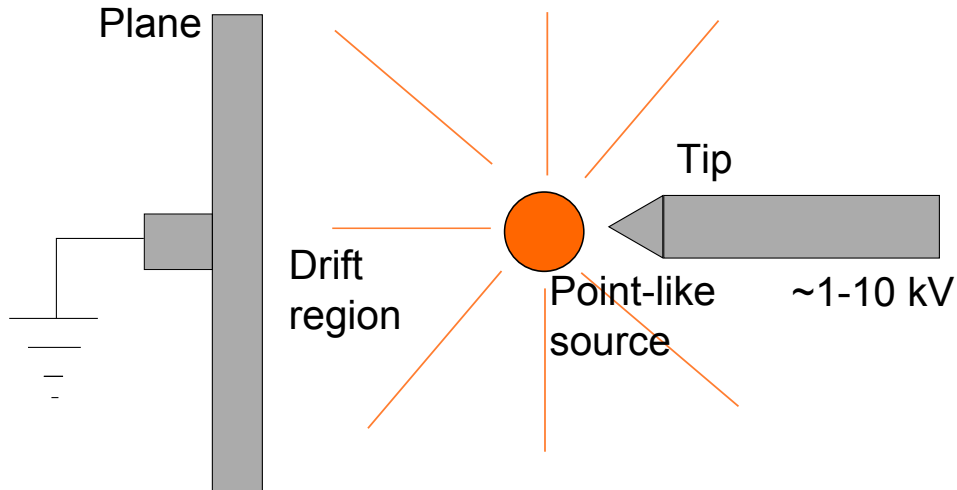


Figure 2.1: Plane-tip electrode configuration.

For a point-plane geometry, the coronal current and potential difference across the cell are related quadratically [96] as follows:

$$I = C_t \mu \epsilon \frac{(V - V_0)^2}{d}, \quad (2.1)$$

where I represents the current, C_t is a constant, μ is the mobility, $\epsilon = \epsilon_0 \epsilon_r$ is the dielectric constant, V is the potential difference and V_0 is the threshold voltage.

The corona discharge in negative polarity is an example of a charge generation process called field electron emission [35], which refers to the emission of electrons by an electrostatic field.

Upon the application of a high voltage across a tip-plane electrode array, a strong divergent electric field is formed around the tip. This in turn generates an ionization zone in which charge carriers are generated and the dielectric surrounding the electrode becomes conductive, while more distant regions do not. When the dielectric near the point tip becomes conductive, it increases the apparent size of the conductor tip. Since the new conductive region is less sharp than the original tip, the ionization may not extend past this local region. Outside this region of ionization and conductivity, the charged particles slowly find their way to an oppositely charged object and are neutralized.

In a corona discharge, ionization is limited to a small region around the electrode,

where the breakdown field strength is exceeded. In the rest of the dielectric medium, we just have a current of slow-moving ions and clusters finding their way to a suitable counter-electrode, such as the walls of the cell. If the geometry and the electric field are such that the ionized region continues to grow until it reaches another conductor at a lower potential, a low resistance conductive path between the two will be formed, resulting in an electric arc. The corona discharge may be maintained as long as the breakdown field strength is exceeded in some region, that is, as long as the voltage of the electrode or the charge density of the charged insulator is high enough.

In summary, the high voltage across the electrodes effectively injects electrons into the cell which transfer energy into the system promoting He atoms into higher energy excited states, ionizing them and thus leading to the formation of excimers, as the electrons transfer their kinetic energy to the surrounding atoms.

2.4 Previous experiments using the corona discharge method

The partner group based in Grenoble, France, led by Nelly Bonifaci, have developed an early version of a spark cell [80]. With it they carried out systematic studies of the atomic lines emitted by helium, mainly the $3^3S \rightarrow 2^3P$ atomic line centered at 706.5 nm [80, 92, 10, 99, 97]. See Table C.1 in Appendix C. They have studied the emission characteristics of said line as a function of temperature and pressure in both (normal) liquid and gaseous phases of helium. One of their most important contributions is the analysis of the asymmetric shape of this atomic transition [10].

They have also found a sharp rotational structure of the $d^3\Sigma_u^+ \rightarrow b^3\Pi_g$ transition centered at 640 nm at 4.2 K (liquid), 6 K (supercritical gas) and 300 K (gas) [81, 82, 80]. Preliminary experiments indicated the possibility of a variation in the positions of the peaks of the rotational lines of that transition potentially related to a changing effective moment of inertia.

2.5 Quantum mechanics of a diatomic molecule

In this Section we briefly present the quantum mechanical theory of rotations and vibrations of diatomic molecules. Special emphasis will be placed on the linear rotor and zero spin particles. The exposition of this Section is based on [55].

The simplest model is that of a two-particle system of masses m_1 and m_2 bound to the ends of a rigid rod of length r . By transforming the coordinate system [43] one can readily see that this is equivalent to a single particle of mass

$$\mu = \frac{m_1 m_2}{m_1 + m_2} \quad (2.2)$$

attached to a rigid rod of length r pivoted at one end [35] and with moment of inertia $I = \mu r^2$. The energy of this system is prescribed by classical mechanics as

$$E = \frac{1}{2} I \omega_{\text{rot}}^2 = \frac{P^2}{2I}, \quad (2.3)$$

with ω_{rot} the angular velocity of the rotation and $P = I\omega$ the classical angular momentum of the system.

Quantizing, Eq. 2.3 becomes

$$\hat{H} = \frac{\hat{L}^2}{2I}, \quad (2.4)$$

with \hat{H} and \hat{L} the Hamiltonian and angular momentum quantum-mechanical operators. The model just described is known as simple rigid rotor.

The solution of the Schrödinger eigenvalue equation with the above Hamiltonian is [35]

$$E_J = \frac{J(J+1)\hbar^2}{2I} \quad (2.5)$$

where the quantum number J is a non-negative integer (excluding spin) and $\hbar = h/2\pi$ [35]. The energy levels of the rigid linear rotor are not equally spaced and, furthermore, the relative separations vary as the square of the quantum number.

In this framework and according to quantum theory, emission occurs when a rotator changes from a higher to a lower (rotational) energy level. The wavenumber associated with the transition is

$$\frac{E' - E''}{hc}, \quad (2.6)$$

where, following [55], a single prime mark denotes the upper state and a double prime mark denotes the lower state.

The rotational term $F(J)$ (in cm^{-1}) is defined as

$$F(J) = \frac{E}{hc} = \frac{h}{8\pi^2 c I} J(J+1) = BJ(J+1), \quad (2.7)$$

which defines the rotational constant B as

$$B = \frac{h}{8\pi^2 c I}. \quad (2.8)$$

The selection rules that hold for the J -quantum number derive from the classical notion that for an optical dipole transition to happen a change of dipole moment

must occur. In our notation this means that

$$\Delta J = J' - J'' = \pm 1. \quad (2.9)$$

Vibrations of the molecule have also to be taken into account to describe the diatomic molecule spectrum. The relative motion of one atom with respect to the other can be reduced to the harmonic vibration of an atom about an equilibrium position similarly to what has been done for rotations; from classical mechanics, the potential energy of the simple harmonic oscillator (SHO) is

$$V = \frac{1}{2}kx^2; \quad (2.10)$$

quantizing, we obtain the following Hamiltonian:

$$\hat{H} = \frac{1}{2}k\hat{x}^2 = \frac{1}{2}m\omega_{\text{osc}}^2\hat{x}^2, \quad (2.11)$$

where ω_{osc} represents the angular frequency of vibration. The solution of the eigenvalue equation produces the following energy levels

$$E_v = \hbar\omega_{\text{osc}} \left(v + \frac{1}{2} \right), \quad (2.12)$$

with $v = 0, 1, 2, 3, \dots$. Unlike the energy levels of the linear rotor, the energy levels of the SHO are equally spaced. The term values for vibration are given by

$$G(v) = \frac{E_v}{hc} = \omega \left(v + \frac{1}{2} \right), \quad (2.13)$$

where $\omega = \hbar\omega_{\text{osc}}/hc = \omega_{\text{osc}}/2\pi c$ is the vibrational frequency measured in cm^{-1} . The vibrational selection rule is

$$\Delta v = v' - v'' = \pm 1. \quad (2.14)$$

There are other effects that influence the spectrum of a diatomic molecule, namely:

1. Anharmonicity of the potential. The SHO is a fair model for any system in the neighborhood of a minimum of potential energy. However, the farther from the equilibrium position, the lesser the adequacy of said model. One could try a Taylor expansion around the minimum and the next term in the approximation is a cubic term as in the following equation (the potential centered at zero for convenience)

$$V(x) = fx^2 - gx^3, \quad (2.15)$$

with $g > 0$ and smaller than f . The vibrational term value becomes

$$G(v) = \omega_e \left(v + \frac{1}{2} \right) - \omega_e x_e \left(v + \frac{1}{2} \right)^2 + \omega_e y_e \left(v + \frac{1}{2} \right)^3 + \dots, \quad (2.16)$$

where x_e , y_e and so on are constants. Each successive coefficient in the last Equation is much smaller than the previous one.

2. Nonrigidity of the rotator. The deviation from the ideal rigid rotor case arises from considering that the idea of vibrations in a diatomic molecule is not compatible with the image of a rigid rotor. The model is then replaced by a massless spring connecting the two atoms; as a result of the centrifugal force, the internuclear distance increases with increasing rotational speed (or, in quantum-mechanical terms, with increasing J quantum number), and so the rotational constant B in Eq. 2.8 must bear a dependence on J , decreasing with increasing J , which can be shown to adopt the form of a factor by $[1 - uJ(J + 1)]$. u turns out to be very small compared to 1 and the F term value becomes

$$F(v) = BJ(J + 1) - DJ^2(J + 1)^2. \quad (2.17)$$

The coefficient D is, with the above choice of signs, positive and is usually called “centrifugal distortion”.

3. Vibrating rotor. In this model, both rotations and vibrations take place and are thus to be both included in the Hamiltonian. For simplicity, any coupling between vibration and rotation is ignored. Under this scheme, a series of the rotational levels of the form 2.17 exists for each vibrational level. In this model, the rotational constant B and centrifugal distortion D bear a dependence on v , given by

$$B_v = B_e - \alpha_e \left(v + \frac{1}{2} \right) + \dots \quad (2.18)$$

$$D_v = D_e - \beta_e \left(v + \frac{1}{2} \right) + \dots \quad (2.19)$$

Then, the rotational F terms for a given vibrational level are given by

$$F_v(J) = B_v J(J + 1) - D_v J^2(J + 1)^2 + \dots \quad (2.20)$$

In conclusion, the term values for a vibrating rotor are

$$T = G(v) + F_v(J) = \omega_e \left(v + \frac{1}{2} \right) - \omega_e x_e \left(v + \frac{1}{2} \right)^2 + \omega_e y_e \left(v + \frac{1}{2} \right)^3 + \dots + B_v J(J+1) - D_v J^2(J+1)^2 + \dots \quad (2.21)$$

In this model, the same selection rules apply as for the individual systems.

4. Symmetric top molecules. They are briefly discussed for the sake of completeness because the quantum number Λ that appears in the treatment of this problem is identical to the Λ quantum number that appears in the treatment of the electronic structure of a diatomic molecule. The symmetric top model as such will not be employed in this work.

The symmetric top in this context is defined as a diatomic molecule with two of its principal moments of inertia equal and the other different, all of them non-zero; in contrast, in a linear rotor, two moments of inertia are equal (and non-zero) and the third is equal to zero.

The term energy levels for this system are given by

$$F(J) = BJ(J+1) + (A-B)\Lambda^2, \quad (2.22)$$

where Λ represents the projection of the total angular momentum along the axis with different moment of inertia.

The rotational constants A and B are defined as

$$B = \frac{h}{8\pi^2 c I_B} \quad (2.23)$$

$$A = \frac{h}{8\pi^2 c I_A}, \quad (2.24)$$

with I_B designating the moment of inertia of the molecule about an axis perpendicular to the internuclear axis (this was I in the rigid rotor model). The only possible values of the J quantum number are $\Lambda, \Lambda + 1, \Lambda + 2, \dots$

A centrifugal term $-DJ^2(J+1)^2$ can be added to account for the non-rigidity of the molecule. Also, a formula analogous to Eq. 2.20 can be written down for each vibrational level of the vibrating symmetric top.

5. Intensity distribution of rotational transitions. The intensity of a spectral line depends not only on the transition probability as expected from Quantum Mechanics but also on the number of molecules in the initial state.

Assuming thermal equilibrium (which is a fair assumption in most situations, except for our experiments, as shall be seen later) and a Maxwell-Boltzmann distribution, the number of molecules that have a classical vibrational energy between E and $E + dE$ is proportional to $e^{-E/kT}$. Applying this to the vibrational levels we get a population in the state designated by v proportional to $e^{-G(v)/hckT}$.

In rotations, the number of molecules in the rotational level J is proportional to $(2J + 1)e^{-F_v(J)/hckT}$ (assuming a vibrating linear rotor). The prefactor in the last exponential is due to the $(2J + 1)$ -fold degeneracy of the rotational levels.

6. Symmetry properties of the rotational levels. It has been established that the complete eigenfunction of a molecule is a product of electronic, vibrational and rotational contributions [35].

In this Section we investigate the eigenfunction properties under the $\mathbf{r} \rightarrow -\mathbf{r}$ (reflection about the origin) operation. Vibrational wavefunctions are unchanged since under this operation the distance between atoms remains unchanged. For rotations, and using the usual notation for spherical coordinates [14], this operation is equivalent to replacing θ by $\pi - \theta$ and ϕ by $\pi + \phi$; linear rotor eigenfunctions change by a factor $(-1)^J$ called parity. Electronic wavefunctions can change sign or not under this operation. A rotational level is positive (negative) if the total wavefunction (that is, the product of electronic, vibrational and rotational eigenfunctions) remains unchanged (changes by a sign) under the reflection at the origin operation.

The following selection rule holds: positive levels combine only with negatives and viceversa; transitions between two positive or two negative levels are forbidden. Symbolically this reads

$$+ \rightarrow - \tag{2.25}$$

$$- \rightarrow + \tag{2.26}$$

$$+ \not\rightarrow + \tag{2.27}$$

$$- \not\rightarrow -. \tag{2.28}$$

When dealing with homonuclear molecules, another important symmetry to consider is the exchange symmetry. When acted upon by the exchange operator of nuclei, the total eigenfunction changes by a factor of ± 1 , and is referred to as symmetric (if it remains unchanged) or antisymmetric (if it changes by

a factor of -1). Symmetric states can be paired off with either even- or odd- J levels; similarly for antisymmetric states.

If the identical nuclei have zero nuclear spin (such is the case for ^4He) it can be shown that the following selection rule holds: there is a perfectly rigorous absence of transitions between symmetric and antisymmetric states. In symbolic terms:

$$\text{sym} \not\leftrightarrow \text{antisym}. \quad (2.29)$$

Furthermore, for a homonuclear diatomic with zero-spin nuclei, and hence formed by bosons, from Pauli Exclusion Principle it follows that no antisymmetric states are populated.

If the nuclear spin is not zero, then the last selection rule does not hold rigorously; this implies intensity alternations in the observed band spectra that can be accounted for using symmetry arguments and population densities arising from them. Since this work is aimed at ^4He , this avenue shall not be investigated further.

2.6 Electronic structure of diatomic molecules

This Section aims to discuss the generalities of the electronic structure of diatomic molecules with no intention to be an exhaustive review of the topic; the contents of this Section follow the structure of the corresponding chapter in [55]. The concepts laid down here will be useful when discussing the electronically excited states of He_2 .

Ignoring magnetic interactions, the energy of a molecule is the sum of kinetic and potential energies of both electrons and nuclei. Due to the smallness of the electron mass compared to the nuclear mass (this ratio is about 1:2000 for the hydrogen atom), the electrons in a molecule can be assumed to move much more rapidly than the nuclei; this argument is known as Born-Oppenheimer's approximation. From this follows that the sum of electronic energy and Coulomb potential of the nuclei acts as the potential energy under whose influence the nuclei carry out their vibrations. The curves representing the variation of the effective potential energy of the nuclei with internuclear distance are designated as potential energy curves. Each electronic state is characterized by a definite potential curve which may have (stable molecular state) or not (unstable molecular state) a minimum.

The Schrödinger eigenvalue equation of a diatomic molecule is customarily solved by resolving the wavefunction ψ into an electronic part ψ_e (bearing dependence only on electron's coordinates) and a vibrational-rotational (that is, nuclear) part

ψ_{vr} (bearing dependence only on the coordinates of the nuclei). This operation produces two separate equations for the wavefunctions ψ_e and ψ_{vr} , respectively. The former and its associated eigenvalue E^{el} depend on the internuclear separation as a parameter.

From said resolution of the wavefunction and employing Born-Oppenheimer's approximation, the total energy of a molecule can be written (in term symbols) as

$$T = T_e + G + F, \quad (2.30)$$

where G and F can adopt the form given above if a vibrating rotor model is assumed. In a molecule the energy levels are more complicated than in an atom because of the existence of vibrational and rotational degrees of freedom additional to the electronic ones. This additional complexity leads to the existence of bands.

2.6.1 Vibrations

The discussion regarding the vibrational rotor presented in the foregoing Section still holds valid in the context of transitions between different electronic states. There are no vibrational selection rules governing the present transitions.

2.6.2 Rotations

Upper and lower states may have different electronic orbital angular momenta Λ . If at least one of them has $\Lambda \neq 0$ the new selection rule for rotational transitions is

$$\Delta J = J' - J'' = 0, \pm 1. \quad (2.31)$$

If $\Lambda = 0$ in both electronic states, then the $\Delta J = 0$ transition is forbidden. The selection rule above sets the definition for the branches of a rotational transition:

$$\Delta J = 0 \quad \text{Q-branch} \quad (2.32)$$

$$\Delta J = -1 \quad \text{P-branch} \quad (2.33)$$

$$\Delta J = 1 \quad \text{R-branch} \quad (2.34)$$

2.7 Classification of electronic states and multiplet structure

In a diatomic molecule, neglecting spin effects, electrons are not subject to a central field force (as they approximately are in an atom), but rather to an axially symmetric

field of force determined by the internuclear axis; hence, only one of the components of the orbital angular momentum is a conserved quantity. Under these conditions the orbital angular momentum \mathbf{L} precesses with a constant component $\hbar M_L$ about the internuclear axis. From angular momentum theory, M_L ranges from $-L$ to L in integer steps [35]. Furthermore, in diatomic molecules, states with different sign of M_L have the same energy and are therefore degenerate.

In the usual notation, $|M_L|$ is designated with the symbol Λ . The associated vector $\mathbf{\Lambda}$ represents the component of the electronic orbital angular momentum along the internuclear axis. The Λ quantum number can assume integer values from 0 through L . The different 0, 1, 2, 3, ... values of Λ are designated with Σ , Π , Δ , ... Π , Δ , ... states are doubly degenerate but Σ states are not.

When taken into account, the spin of the individual electrons leads to a multiplet structure of the spectral lines. The electron spins are coupled into a resultant \mathbf{S} . When $\Lambda \neq 0$, \mathbf{S} precesses about the internuclear axis and $\Sigma = M_S$ is conserved. In contrast to Λ , Σ can vary from $-S$ through S .

The total electronic angular momentum $\mathbf{\Omega}$ is the vector addition of $\mathbf{\Sigma}$ and $\mathbf{\Lambda}$. This vector sum is simplified by the fact that both vectors lie on the internuclear axis so an algebraic sum is enough in this case. The quantum number Ω , which describes the resultant electronic angular momentum about the internuclear axis, is defined as $|\Lambda + \Sigma|$. $2S + 1$ is called the multiplicity of a state; this magnitude is added to the term symbol as a left superscript.

The symmetry properties of the electronic eigenfunction are of great importance for the classification of molecular states. In a diatomic molecule, any plane through the internuclear axis is a plane of symmetry. Therefore the electronic eigenfunction of a (non-degenerate) Σ state changes by a factor of ± 1 when reflected at any plane passing through both nuclei. If the factor is positive, the state is designated as Σ^+ ; if it is -1 , the state is designated by Σ^- .

Another symmetry property that applies to homonuclear molecules is symmetry with respect to the center of symmetry. If the electronic eigenfunction remains unchanged it is said to be even (and designated by a “*g*” subscript, meaning *gerade* or “even” in German); if it changes sign it is said to be odd (and designated by a “*u*” subscript, meaning *ungerade* or “odd” in German).

2.8 Coupling of rotations and electronic motion and Hund’s coupling cases

The foregoing Sections dealt with the three motions of a diatomic molecule, electronic, vibrational and rotational ignoring the mutual interactions between them.

In certain cases of interest as we shall see in following chapters it is found that the interaction between rotational and electronic motion must be taken into account; then the so-called Hund's coupling cases arise. Cases (b) and (d) will be explored in detail as they will be shown to be important for the He_2 molecule.

2.8.1 Hund's coupling case (b)

When $\Lambda = 0$ and $S \neq 0$, the spin vector \mathbf{S} is not coupled to the internuclear axis at all because spin-orbit coupling vanishes in this case. Sometimes, especially for light molecules, even if $\Lambda \neq 0$, the spin vector \mathbf{S} may be very weakly coupled to the internuclear axis. This defines Hund's case (b)¹.

Angular momentum vectors $\mathbf{\Lambda}$ and \mathbf{R} (\mathbf{R} represents the rotation of the molecule) form a resultant \mathbf{N} , whose corresponding quantum number N can have integer values from Λ onwards (that is, $N \geq \Lambda$). \mathbf{N} and \mathbf{S} form a resultant designated by \mathbf{J} . From angular momentum theory, the only possible values for the quantum number J range from $|N - S|$ until $N + S$ in integer steps.

The good quantum numbers of Hund's coupling case (b) are Λ , N , S and J .

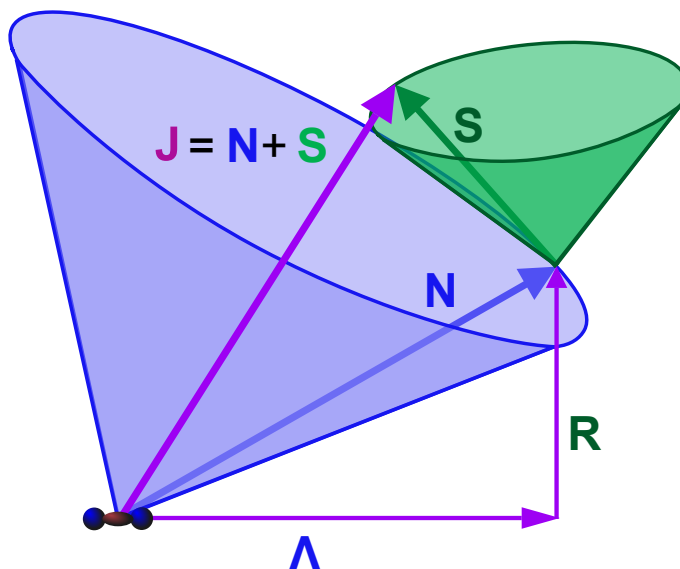


Figure 2.2: Hund's case (b).

2.8.2 Hund's coupling case (d)

This case arises when the coupling between \mathbf{L} and the internuclear axis is very weak while the interaction between \mathbf{L} and the axis of rotation is strong. The angular momenta \mathbf{L} and \mathbf{R} are added giving \mathbf{K} . This vector can be further coupled to \mathbf{S} in the same fashion as in case (b) to give \mathbf{J} .

¹In this work, the modern notation for Hund's coupling case (b) is adopted systematically. Cf. footnote 1a of Chapter V of [55].

The quantum number K can take on integer values between $|R - L|$ and $R + L$. There are $2L + 1$ different K values for each R , except when $R < L$. A good set of quantum numbers for this coupling case is L , R , K , S and J .

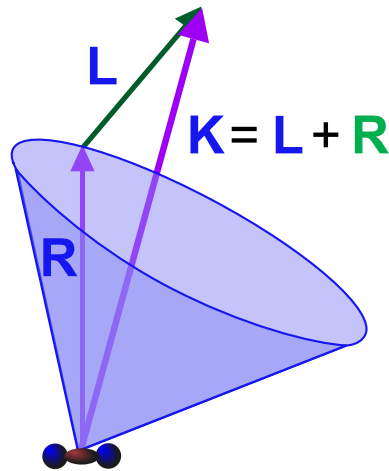


Figure 2.3: Hund's case (d).

This coupling case is an appropriate description for the electronic states of many Rydberg molecules, where the Rydberg electron interacts very weakly with the molecular core.

2.9 Excimers

2.9.1 Formation of excimers

The aim of this section is to describe a chain of processes that account for the physical generation of helium excimers in our corona discharge starting from atomic helium.

Molecular ions of helium and other rare gases were first identified by mass spectrometry. In particular, the existence of He_2^+ was established in helium relatively early [107].

Two successive reactions have been identified as responsible for the formation of He_2^+ in helium [16]:



This can be followed by associative ionization or Hornbeck-Molnar process (only possible for $n \geq 3$ states of helium) [15, 62, 113]:



Another way to produce the molecular helium ion is via a three-body process:



He ionization into He^+ ions can be produced via collisions with low $E \sim 25$ eV electrons:



The molecular He ion can then recombine with an electron for producing then a helium excimer



2.9.2 Electronic structure of helium excimers

It is well known that the potential energy curve for the ground state of the He_2 molecule is repulsive and thus unstable [18]. However, excited states are strongly bound and that enables us to study the spectroscopy of the helium molecule.

The electron has spin $1/2$. This means that a He atom can exist in states of total spin $S = 0$ or $S = 1$, known as singlet and triplet, respectively. The selection rule $\Delta S = 0$ is strictly enforced in dipole transitions and that means that there is a set of transitions involving singlet states and a different set involving triplet states; however, there is only one ground state and it is singlet, so there are no transitions from triplet levels down to the ground (singlet) state or, more precisely, said transitions have a very long lifetime. Similarly, the molecular levels of He_2 exist either as triplet or singlet and dipole transitions between them are ruled by the selection rule stated above. Notable molecular and atomic transitions of helium are listed in Appendix C.

The helium-helium intermolecular potential energy curves have been investigated extensively both theoretically and experimentally [31, 67, 41]. Over 60 electronic states are known for the He_2 molecule and they are Rydberg states [41]. They are states in which one electron is excited to an atomic (or molecular) orbital large in size compared with a usually singly-charged “core”. The energy of such states (both atomic and molecular) can be expressed as

$$T = \frac{RyZ_c^2}{n^{*2}} = \frac{RyZ_c^2}{(n - \delta)^2}. \quad (2.40)$$

Z_c is the charge on the core, Ry is the Rydberg constant (see Table E.1 in Appendix E) and δ is known as quantum defect and depends on l and n at low n values.

In Fig. 2.4 a reconstruction of the potential energy curves from experimental data

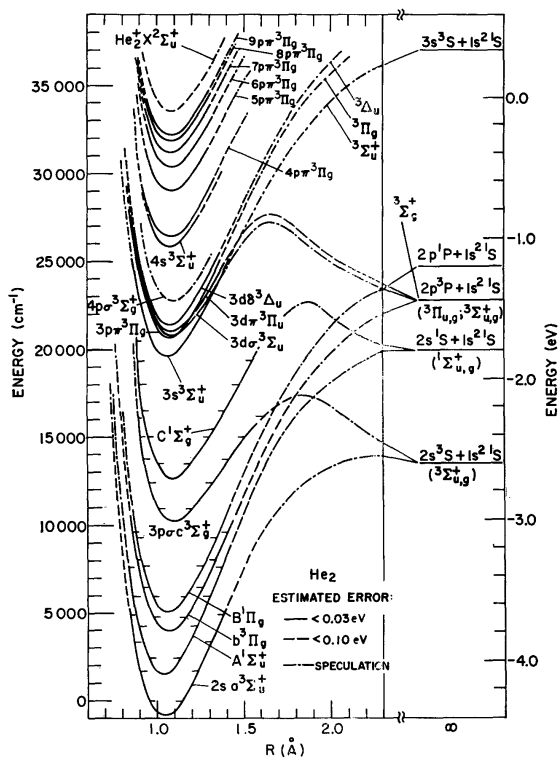


Figure 2.4: Potential energy curves for states of He_2 . Reproduced from Fig. 1 of [41]. Vibrational levels are indicated by horizontal lines at the edges of the corresponding curves.

by Ginter is shown. The repulsive $X^1\Sigma_g^+$ ground state [102] has been omitted. All electronic states observed (apart from the repulsive state) converge on the $X^2\Sigma_u^+$ state of He_2^+ . This diagram also shows the separated-atom limit for each of the potential energy curves.

The lowest-energy stable states correspond to the $a^3\Sigma_u^+$ and $A^1\Sigma_u^+$ states of He_2 and are associated with the 2s Rydberg orbital.

The $b^3\Pi_g$ and $B^1\Pi_g$ states of He_2 lie next in order of increasing energy and are associated with the 2p π Rydberg orbital. The $b^3\Pi_g$ exhibits partially resolved triplet splitting [41] and a transition from Hund's coupling case (b) (or (b')) to case (d) with increasing nuclear rotation.

The $c^3\Sigma_g^+$ and $C^1\Sigma_g^+$ states of He_2 are associated with the 3p σ orbital and it is known through theoretical calculations that said states exhibit potential maxima [31].

The vibrational ground state of 10 different electronic states, including $3sd^3\Sigma_u^+$ and $3sD^1\Sigma_u^+$ lie in a region of substantial crowding of electronic states. These states and higher-lying potential energy curves have been discussed in the literature [41].

2.9.3 Electronic structure of the transition of interest

In this Subsection the electronic dynamics of $d^3\Sigma_u^+ \rightarrow b^3\Pi_g$ will be analyzed following [81]. The energy levels involved in this transition are characterized by Hund's coupling case (b) and $S = 1$.

The upper molecular state Σ_u^+ being u implies that the only allowed values for the quantum number N are odd. Every N state is split into three different states with J values of $N - 1$, N and $N + 1$ and $N \geq \Lambda = 0$; see Fig. 2.5. The lower molecular state Π_g has even symmetry (due to it being g); the quantum number N can take on any integer value from $\Lambda = 1$ onwards and every N state is split into three levels with $J = N - 1$, $J = N$ and $J = N + 1$.

An energy level diagram of the $^3\Sigma$ state is shown in Fig. 2.5. The corresponding diagram for the $^3\Pi$ state is shown in Fig. 2.6 as it will be useful for discussing the transition of interest in this work.

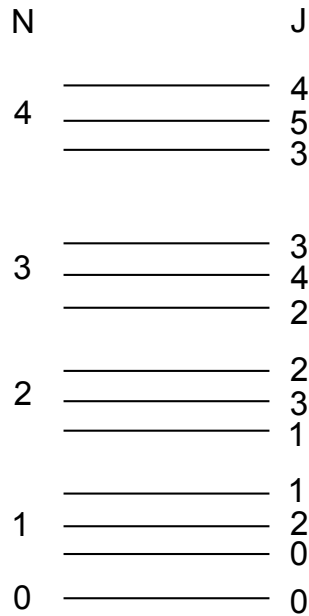


Figure 2.5: Schematic energy levels of $^3\Sigma$ state as per Hund's coupling case (b). Notice that the level with $J = N$ has maximum energy and $J = N - 1$ has the lowest energy [81]. Diagram reproduced from Fig. 101 (b) of [55]. If the state is u then only odd- N levels are populated; only even- N levels are populated if the state is g . The ordering of the J -levels for each N is determined by the spin-spin interaction [71] and the magnetic interaction of \mathbf{N} and \mathbf{S} [95]; see V.2 of [55].

The selection rules that hold for this transition are:

$$\Delta J = 0, \pm 1 \quad (2.41)$$

$$\Delta N = 0, \pm 1 \quad (2.42)$$

$$J' = 0 \not\leftrightarrow J'' = 0. \quad (2.43)$$

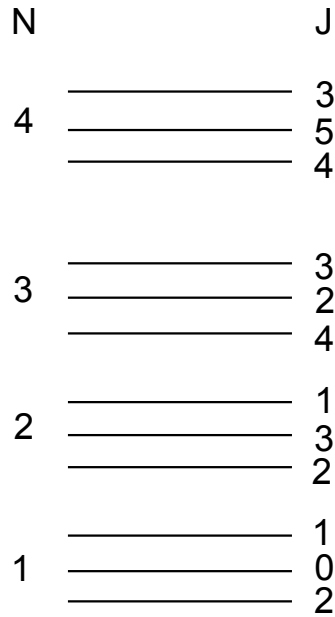


Figure 2.6: Schematic energy levels of ${}^3\Pi$ state. Diagram reproduced from Fig. 1 of [40]. The energy level structure is determined by considering spin-orbit, spin-other orbit and spin-spin interactions only [32].

A schematic representation of the transitions that make up the transition of interest is found in Fig. 2.7.

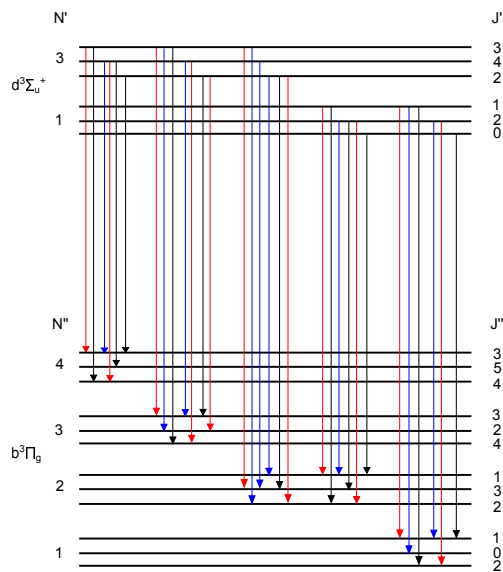


Figure 2.7: Structure of the $d^3\Sigma_u^+ \rightarrow b^3\Pi_g$ transition. This diagram is not to scale. Due to the *ungerade* character of the upper state, the only allowed values for the quantum number N' are odd. The transitions have been deduced using the selection rules (2.41), (2.42) and (2.43). P-lines are indicated in black; Q-lines are drawn in red and R-lines in blue. Lines with $\Delta N = \Delta J$ have high intensities and are called ‘general branches’ (see the measured spectra in Chapter 4); they are accompanied by ‘satellite transitions’, defined by $\Delta N \neq \Delta J$ [81].

Since the rotational constants of upper and lower states are very similar (see pp.

292-301 of [63] or Sec. 4.10.3 for the rotational constants of states $d^3\Sigma_u^+$ and $b^3\Pi_g$), the rotational lines of the Q-branch are close and cannot be resolved.

Intensities of the observed rotational bands are ruled by Hönl-London factors. They have been calculated for various spin states, $S = 1$ in particular, and are reported elsewhere [70] for the different branches of the transition.

2.10 Excimers in liquid helium

The available information regarding the interaction potential of He_2^* -He is relatively scarce [29] and so is the knowledge of the interaction potential of He^* -LHe [57]. Dennis and coworkers [28] established in 1969 the existence of discrete excited states in liquid helium by recording the emission spectrum of electron-bombarded liquid helium (see Fig. 2.8); the spectrum shows clear distinct (though rotationally unresolved) transitions that resemble those of helium in the gaseous phase. However, this observation is at odds with Hill *et al.*'s work [58], again with electron-bombarded liquid helium, in which they were able to resolve rotational structure. In both of the cited experiments the question remains as to how the electron-beam might have increased the local temperature of the light-emitting region. See Fig. 1.8.

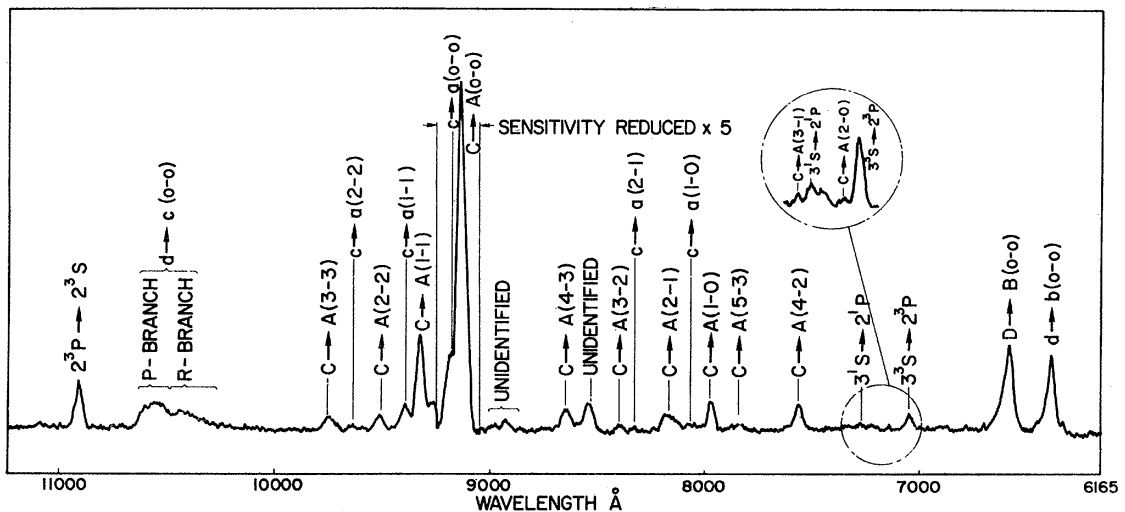


Figure 2.8: Emission spectrum of electron-bombarded liquid helium by Dennis and coworkers. Reproduced from Fig. 2 of [28]. Transitions were identified via a comparison to a calibrated emission spectrum of helium.

The observed spectrum in liquid helium is similar to atomic and molecular spectra in the gaseous phase of helium. In the spectrum different vibrational bands (with no rotational resolution) of various molecular transitions are apparent². The

²Before Dennis, Surko and Reif established the existence of excitations in liquid helium using an α -particle source [101].

atomic and molecular transitions were identified as due to He_2^* via comparison with the corresponding gas-phase spectrum; this was an unexpected finding as the expected result for a bulk rare gas was rather a completely unresolved spectrum. This evidence prompted them to hypothesize the existence of localized states due to a bubble around the excited helium molecule.

The existence of a bubble around a He atom or molecule in liquid helium was investigated theoretically by Hickman a few years later [56]. It was found that the cavity surrounding excited He atoms in liquid helium is smaller than the cavity surrounding a free electron. Hickman, Steets and Lane developed a model a few years later [57] that reproduces with fairly good accuracy the optical spectrum; this model is based on a classical calculation of the energy to form the bubble. Then, in 1971, rotational structure in an absorption line was observed [58].

Fig. 2.9 shows a schematic picture of a helium excimer in liquid helium; such species is in a state usually referred to as a Rydberg state. Since the He atoms are clustered around the helium excimer in liquid helium, in this work we adopt the convention of using interchangeably the terms bubble and cluster. Along the same lines, we say that the helium excimer is caged or solvated in the bubble within liquid helium. Said terms are henceforth used as synonyms in this work.

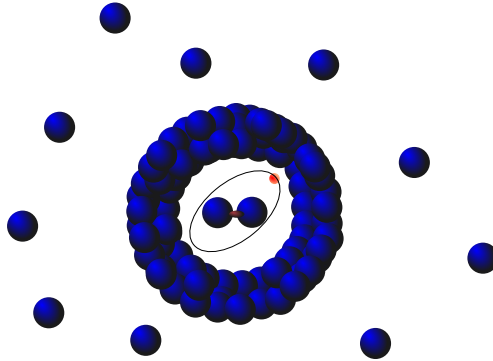


Figure 2.9: Schematic diagram of a He_2^* excimer enclosed in a bubble, characterized by a sharp interface between He_2^* and ground state He.

When a sample of liquid helium has been heated via an excitation (electron beam, synchrotron radiation, electrical discharge, etc.) it is possible that pockets of gaseous helium within the liquid helium may be formed. An example of this phenomenon will be seen in the following chapters. See Fig. 2.10.

2.11 Snowballs and cavities in liquid helium

When a positive electric charge such as He^+ or He_2^+ (other ions like Ar^+ or Pb^+ are also customarily used) is injected into liquid helium, the ion produces a strong electric field that polarizes the surrounding medium and drives some of it into the

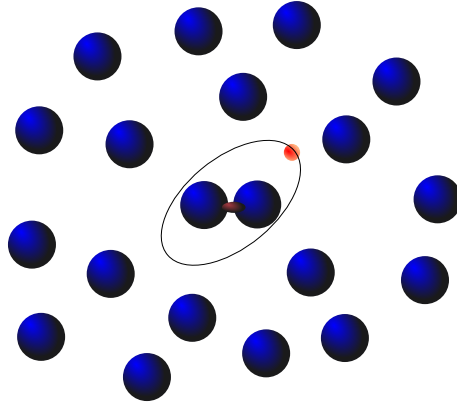


Figure 2.10: Schematic diagram of a He_2 excimer embedded in a gaseous environment.

immediate vicinity of the charge, thereby creating a region where the local density is much higher than in the rest of the liquid helium. This phenomenon is known as electrostriction [17]. The positive helium cluster is held together by electrostriction which can be calculated by semiclassical considerations [17]. This structure has been found to be a sphere of 6 Å radius, solid in its close proximity to the ion, and it is usually called “snowball” [24]. Recent work by us shows that at elevated temperature and low pressure the snowballs are liquid-like [8]. Further work by us shows that snowballs also exist in supercritical helium if pressure is high enough [103].

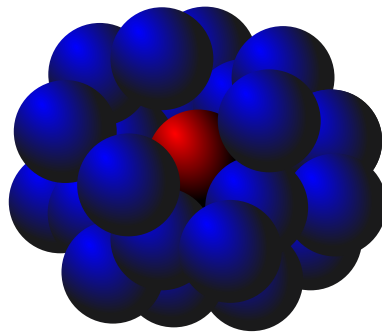


Figure 2.11: Model of a He^+ snowball.

In contrast, an electron injected into liquid helium forms around itself a void space via the Pauli Exclusion Principle, known as an “electron bubble” [73]. This is due to the small atomic polarizability of He which in turn implies that the e-He interaction can be modeled as a hard-sphere repulsion [59, 65]. The mechanism by which the electron results trapped in the void is still not completely understood but it can be modeled as a particle in an infinite potential well [24]. Much less attention has been paid to the fact that the electron also attracts helium atoms via the same electrostriction effects. These attractive forces build a region of higher helium density around the electron void, so that the whole system can be regarded

as a cluster. Evidence for this structure is the difference between the void radius [50, 47] and the hydrodynamic radius [9, 7].

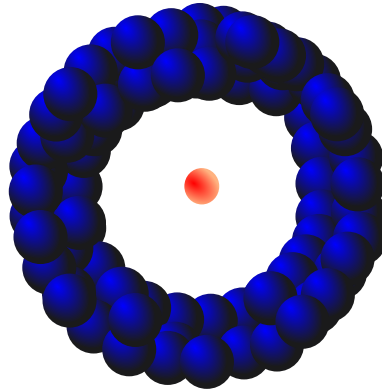


Figure 2.12: Schematic diagram of an electron bubble

It is important to emphasize that an excimer in liquid helium develops a void very similar to that of electrons, as it has just been discussed, but also some solvation layers whose density is expected to surpass that of liquid helium and that we will refer to as clusters in the forthcoming chapters.

Chapter 3

Overview: setup of a new experiment

The experiment requires the probing of the different thermodynamic phases of helium and so low temperatures are needed. The overarching goal in a low temperature experiment is to reduce the influx of heat while maximizing the cooling power of the refrigerator¹. Heat can be transferred by conduction, convection and radiation; hence, different measures can be taken to reduce undesired heat flow into the system.

3.1 Radiation minimization

Heatshields are customarily used in cryostats to reduce the effects of radiation. A heatshield is a metallic container in direct contact with a stage of the fridge at a certain temperature (and with a given cooling power). The heatshield is then nominally at the same temperature as the stage that it is attached to (although temperature gradients may arise when the material of the heatshield does not have a high enough thermal conductivity). Hence, the shielded surface is exposed to a surface at a lower temperature.

This technique can be iterated and so a typical fridge can feature several heatshields at decreasing temperatures, thereby damping the temperature gradient and reducing the temperature of the emitters in radiative contact with the coldest surface in the setup.

¹For the experiment to work the heat transfer from the environment should be less than the cooling power of the device. The cooling capacity (power) of a device is the rate of heat removal from the refrigerated space by a refrigeration system [23].

3.1.1 Estimation of the radiation heat load

A black body is defined by absorptivity a and emissivity ϵ both equal to unity and zero reflectivity.

The Stefan-Boltzmann's law [35] states that the total radiant energy emitted per second per unit area by a black body at temperature T is given by

$$E = \sigma T^4, \quad (3.1)$$

where $\sigma = 5.67 \times 10^{-8} \text{ W/m}^2\text{K}^4$ is the Stefan-Boltzmann constant.

To illustrate these concepts we will calculate the heat transfer rate from a room temperature environment (taken as 300 K) through a small orifice on a heatshield leading directly to the lowest temperature part of the setup. A 1 mm radius aperture would contribute 1.44 mW to the heatload. The choice of this example becomes clear in Fig. 3.8, where the optical setup is explained.

Also, assuming that the temperature across the heatshield in radiative contact with the coldest point in the setup is uniform (that is, neglecting any thermal gradient effect), 4 K in this example, then a heat load of 2.22 μW was found (the cylinder radius is 73.5 mm and height is 257.34 mm).

3.2 Convection minimization and pumping system

Pumping a vacuum jacket in the chamber that hosts the experiment greatly reduces conduction and convection caused by the gas within the container. Typical vacuum levels for cryogenic experiments lie in the range of 10^{-4} - 10^{-8} mbar.

In a cryogenic experiment the first stage of the pumping is usually achieved with mechanical pumps in a pumping station detached from the cryostat; in our experiment we have utilized a pumping station consisting of a turbomolecular pump backed by a rotary pump physically mounted on a cart. A diagram of the setup is shown in Figure 3.1.

The pumping station is highly modularized and features a system of valves that allow the user to start the turbopump even if the setup is disengaged from the refrigerator chamber, thus saving time every time the fridge is opened by not having to start the turbopump all over again. This is achieved by allowing the rotary pump to bypass the turbopump when pumping the chamber at atmospheric pressure.

The vacuum levels are measured in the pumping station at the points marked as channels 1, 2 and 3 with two Pirani gauges and a Penning gauge, respectively; gauges 2 and 3 are placed at the turbomolecular pump. The vacuum in the cryostat

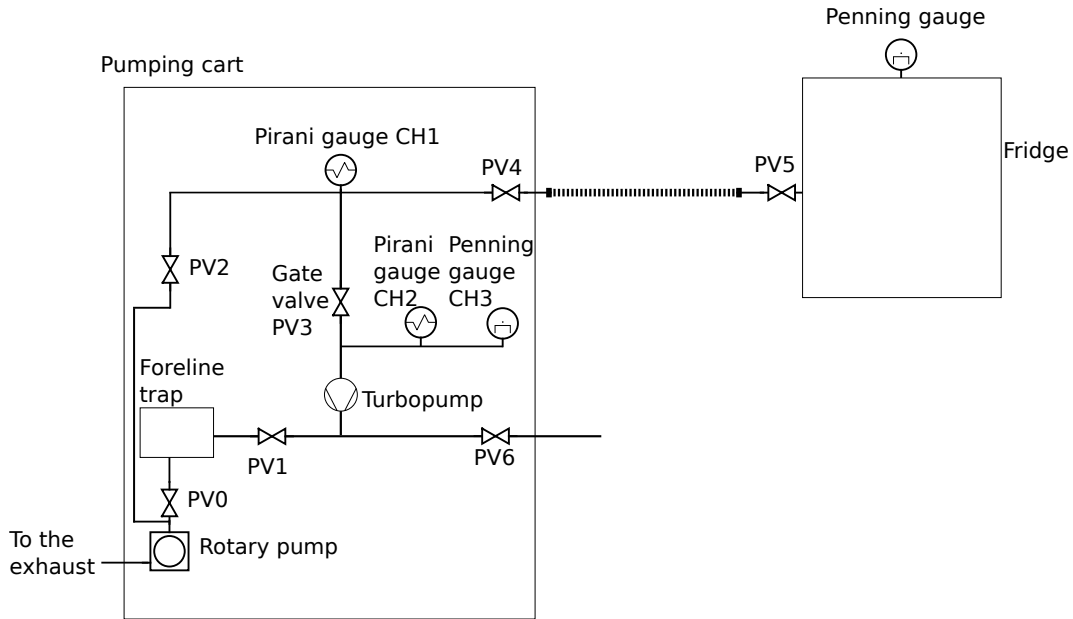


Figure 3.1: Schematic diagram of the pumping station utilized in this experiment. Symbols to draw this diagram were taken from [117].

chamber is measured via a Penning gauge at the bottom of the chamber.

The procedure for operating the pumping station is provided in Appendix A.

Once the vacuum in the chamber (measured via the Penning gauge) has reached 10^{-4} - 10^{-5} mbar, the cooling-down process can get started. Cooling provides additional pumping, as will be explained in Sec. 3.6.1, enabling the pressure in the vessel reach down to 10^{-6} mbar.

3.3 Conduction minimization

3.3.1 Heatsinking and cryogenic cables

In this experiment it is necessary to run cables down to the sample (or, more properly, the coldest part of the setup) while minimizing the loss of cooling power via the wires. In other words, the thermal link between a room temperature environment and the cold sample has to be attenuated insofar as possible. Copper is not well suited for this task but instead low cross-section cryogenic cables are customarily used.

The working principle of cryogenic wires (typically phosphor-bronze, constantan or nichromel) is they have a thermal conductivity fairly smaller than that of ordinary metals (see Table 3.2) so they can be deemed thermal insulators when compared to copper; however, this comes at a cost of an electrical resistivity larger than that of copper² (see Table 3.1). A commonly used material for insulating these cables is

²This is not an issue for the present application.

polyimide or formvar [4].

Material	Resistance per unit length (Ω/m)		
	4.2 K	77 K	305 K
32 AWG Phosphor bronze	3.34	3.45	4.02
34 AWG Copper	0.0076	0.101	0.81

Table 3.1: Electrical resistances per unit length of phosphor bronze and copper. Data from [4].

	T (K)	Phosphor bronze	Copper
	1	0.22	70
	4	1.6	300
	10	4.6	700
	20	10	1100
Thermal conductivity ($W/m \cdot K$)	80	25	600
	150	34	410
	300	48	400

Table 3.2: Thermal conductivities of phosphor bronze and copper. Data from [4].

In order to reduce the thermal gradient between the ends of a cable, one of them at room temperature and the other one typically at a few kelvin, the idea of precooling is exploited. It consists of different cables inside the fridge being heatsunk, that is they are wrapped around copper bobbins bolted on to the various stages of the fridge (which are usually at 4 K and 80 K); the efficiency with which the wires are cooled down depends on the number of turns, the craftsmanship of the heatsinking and the cooling power of the heatshields. At least 5 turns of a wire around a bobbin are recommended for an efficient heatsinking [4].

3.3.2 Calculation of the heat contribution via conduction due to a temperature gradient

In this subsection a model calculation of the heat gain to the experiment via conduction is performed. The treatment of the heat transfer rate by solids is based upon [114].

Given a solid of cross-section A subject to a temperature gradient $\partial T/\partial x$, the heat transfer rate \dot{Q} is given by

$$\dot{Q} = \lambda(T)A \frac{\partial T}{\partial x}, \quad (3.2)$$

where $\lambda(T)$ is the temperature-dependent thermal conductivity of the solid; it describes the ability of a material to conduct heat at temperature T . $\lambda(T)$ at very low

temperatures is highly-dependent on the composition of the metal.

If the ends of a solid bar of uniform cross-section A and length l are at temperatures T_1 and T_2 then

$$\dot{Q} = \frac{A}{l} \int_{T_1}^{T_2} \lambda(T) dT. \quad (3.3)$$

Given the practical difficulty of calculating the above integral, we can use the mean value theorem for integrals [98] to deduce that

$$\bar{\lambda} = \frac{1}{T_2 - T_1} \int_{T_1}^{T_2} \lambda(T) dT. \quad (3.4)$$

In practice, $\bar{\lambda}$ has been measured for various materials and significant pairs of temperatures [114].

	$\bar{\lambda}$				
T_2	300	300	77	4	1
T_1	77	4	4	1	0.1
Nylon	0.31	0.27	0.17	0.006	0.001
Pyrex glass	0.82	0.68	0.25	0.06	0.006
Machinable glass ceramic	2	1.6	1.3	0.03	0.004
Graphite (AGOT)	-	-	-	0.0025	0.0002
18/8 Stainless steel	12.3	10.3	4.5	0.2	0.06
Constantan (60 Cu, 40 Ni)	20	18	14	0.4	0.05
Brass (70 Cu, 30 Zn)	81	67	26	1.7	0.35
Copper (phosphorus deoxidized)	190	160	80	5	(1)
Copper (electrolytic)	410	570	980	200	(40)

Table 3.3: Mean values of thermal conductivities for various materials with ends at different pairs of temperatures. Table reproduced from Table 5.1 of [114]. Temperatures in K; mean values of thermal conductivity in $W/m \cdot K$.

From the last two equations it follows that

$$\dot{Q} = \frac{A}{l} \bar{\lambda} (T_1 - T_2). \quad (3.5)$$

The considerations from this Section are relevant for calculating the heat load contribution due to the gas supply line. This can be done in the following fashion: we have used $1/16''$ outer diameter tubing with $0.020''$ wall thickness. The length of tubing between the stages of the fridge (at 77 K and 4 K) is about 1.5 m. Hence, from Eq. (3.5) and using the data from Table 3.3 for stainless steel, the heat transfer rate from the 77 K via stainless steel plumbing is less than 0.5 mW.

3.3.3 Thermal conductivity of materials at low temperatures

The purpose of this section is to illustrate how the thermal conductivity³ of several relevant materials, especially oxygen-free high conductivity copper (OFHC), evolves with temperature. We will employ an empirical model developed by NIST that is suitable for various metals in a range of temperatures up to 300 K [84]. In what follows, \log denotes common logarithm, that is, logarithm to the base 10. Also, the convention of entering dimensionless quantities in mathematical functions has been overlooked so the coefficients used below in Eqs. (3.6) and (3.8) have been chosen by NIST to produce a correct fit for the observed conductivities in SI units. The model for the thermal conductivity, k , is given by

$$\log k = a + b\Theta + c\Theta^2 + d\Theta^3 + e\Theta^4 + f\Theta^5 + g\Theta^6 + h\Theta^7 + i\Theta^8, \quad (3.6)$$

where

$$\Theta = \log T; \quad (3.7)$$

in this model the coefficients are determined experimentally. The above model does not hold for OFHC, for which the appropriate equation is

$$\log k = \frac{2.2154 - 0.88068 T^{0.5} + 0.29505 T - 0.048310 T^{1.5} + 0.003207 T^2}{1 - 0.47461 T^{0.5} + 0.13871 T - 0.020430 T^{1.5} + 0.001281 T^2}. \quad (3.8)$$

Fig. 3.2 shows that k is a non-linear function of the temperature. It also shows that the thermal conductivity of OFHC is at least two orders of magnitude above other materials. This justifies the choice of this metal for the design of the spark cell to be explained below and in other cryogenic applications. It should also be mentioned that the presence of impurities can easily modify reported values of the thermal conductivity at low temperature [84].

3.3.4 Joule heating contribution

The operation of the electrode-tip array featured in this experiment makes the most important contribution to the heat load on the fridge because of Joule heating.

Typical voltages of operation (in the liquid helium regime) are, as will be explained later, about 10 kV and typical currents are of the order of 1 μ A. A first estimation of the Joule heating contribution is, then, about 10 mW.

³From here on out designated by k , following [84].

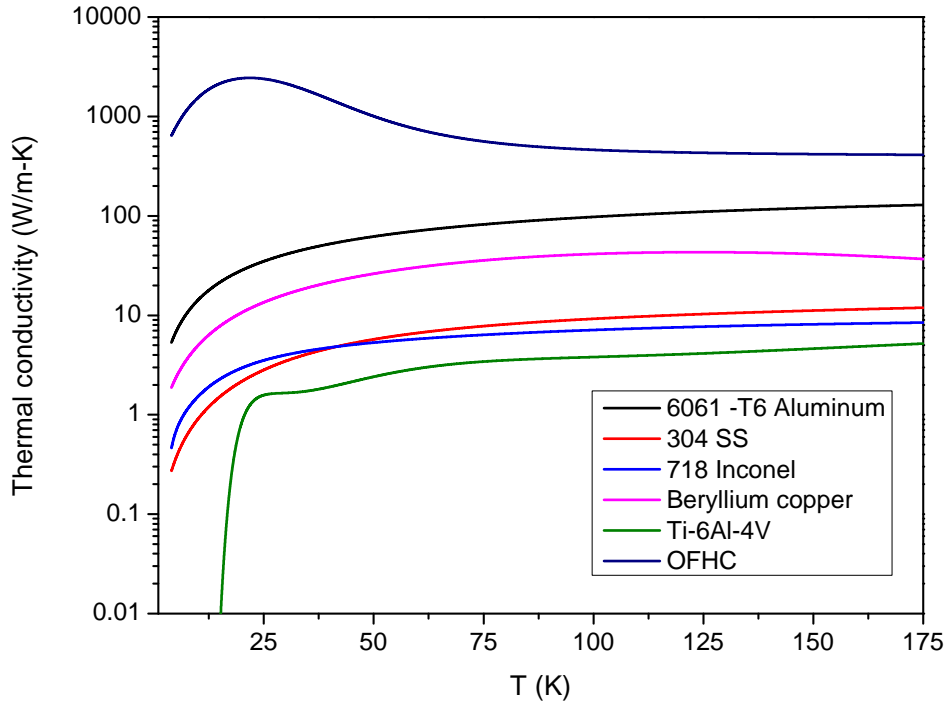


Figure 3.2: Thermal conductivities of different materials in the cryogenic regime. The curves shown have been calculated using Eqs. (3.6) and (3.8) utilizing the coefficients from [84].

3.4 Total heat transfer rate into the setup

In previous sections the radiation (both from the pinhole and the 4 K heatshield), conduction (via the stainless steel plumbing) and Joule-heating contributions have been estimated and have been found to lie in the mW or μ W regime.

The convection and conduction contributions via the low-pressure gas in the vacuum chamber have been neglected. The heat load from the high-pressure gas into the cell has not been calculated but from an intuitive point of view it can be estimated to be lower than the heat load due to conduction via the pipes.

Hence, it is reasonable to assume that the cooling power of the second stage of the refrigerator (0.3 W) will be enough to counteract the heat transfer from the various sources mentioned above into the cold cell.

3.5 Wet and mechanical refrigerators

This section gives a brief overview on the principles of refrigeration based on [118, 90].

Two methods exist relying on similar physical principles for attaining low temperatures in a cryogenic experiment [118]. In the first method cryogenics (like liquid nitrogen and helium) absorb the heat from the sample and will ultimately boil off

taking away the heat. The heat is transferred to the cryogen by conduction. These methods demand a constant resupply of cryogen. We will not be concerned with such fridges in the present work.

By contrast, mechanical refrigerators are based in a closed refrigeration cycle of a cryogen (usually helium) in the gas phase. These coolers do not need to be topped up. However, generally these devices have a lower cooling power than the wet cryostats [118].

There are two kinds of mechanical fridges: Gifford-McMahon and Pulse tube refrigerators. Both kinds of devices feature a compressor (outside the fridge) and an expansion chamber inside the fridge. They both compress helium gas at room temperature in the compressor, then send it into the cryostat where it is expanded to produce a cooling effect via the Joule-Thomson effect. A GM cooler uses a piston in the expansion chamber; a pulse tube cooler replaces the moving piston with acoustic pulses in the helium gas [118]. These devices operate, then, on the basis of the so-called ideal vapor-compression refrigeration cycle [23]; however, mechanical fridges in this mode of operation can only produce temperatures of 4 K.

For attaining lower temperatures the fact that reducing the pressure reduces the boiling point is exploited. Pumping in a mechanical cooler is customarily achieved using a sorption pump. The working principle of a charcoal sorption pump is that it adsorbs helium at low temperatures, but it can be driven off by heating the charcoal above 20 K. Then it is allowed to cool, pumping the helium out of a 1 K (for a ^4He line) or 300 mK (in a typical ^3He line) reservoir, which has a cooling effect on the pot⁴.

Given the high cost of ^3He , it is usually kept in closed lines where it is continuously recycled, avoiding any wastage to atmosphere.

3.6 Heliox AC-V He-3 refrigerator

In our experiments we have utilized a Heliox AC-V He-3 refrigerator. A schematic diagram of this device is shown in Fig. 3.3. The insert that makes up the bulk of the machine is contained (while it is operational) in the outer vacuum chamber (OVC).

The Heliox AC-V He-3 is a mechanical refrigerator and its working principle is as described above. This fridge performs an ideal vapor-compression refrigeration cycle via a compressor and a pulse tube cooler [112] on a ^4He line (not shown on the figure) to cool down to 4 K a gold-plated copper plate known as the second stage of the fridge. The cooling power of the second stage is 0.3 W [112].

There exists a thermal link between the sorption pump (designated by the

⁴The pot and other parts of the mechanical fridge we have employed will be explained in Sec. 3.6.

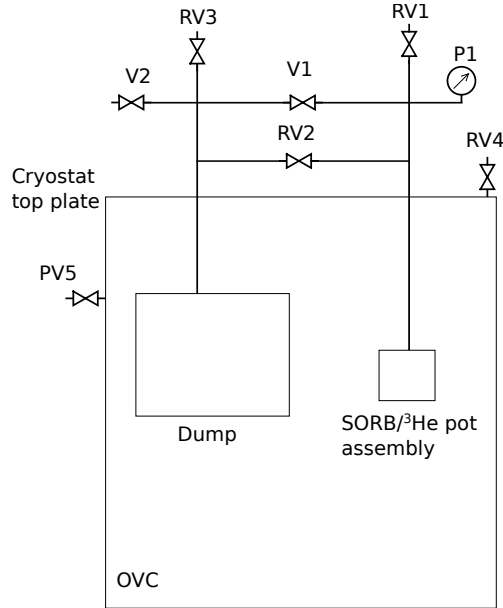


Figure 3.3: Schematic diagram of the fridge utilized in this experiment. Figure reproduced from [3].

acronym SORB) in the ^3He line and the second stage via a thermal switch that can be alternatively closed or opened⁵. The ^3He line is divided into two sections: the “dump” and the “pot”, separated by valves as per Fig. 3.3. The dump is a large volume used to release any excess pressure in the gas line. The pot side of the gas line contains the SORB and, at the bottom of the line, the pot is where liquid ^3He is condensed. Pressure in the pot is monitored through P1.

3.6.1 Operation of the Heliox AC-V He-3 refrigerator

To cool down the Heliox AC-V fridge, the OVC has to be sealed and evacuated down to the range of 10^{-4} or 10^{-5} mbar. V1 can be open when the fridge is at room temperature.

The refrigerator can be started by simply starting the compressor and the cooling water. After approximately 24 hours of operation under normal conditions the so-called cryogenic pumping sets in⁶.

3.7 General layout of the experiment

Fig. 3.4 features a schematics of the fridge and its position relative to the spectrometer; the optics to couple light into the spectrograph is also shown. The Heliox AC-V

⁵In practice this is achieved by operating a resistor.

⁶Cryogenic pumping means that the (cryogenically) cold surfaces will freeze out any remaining impurities and start collecting them at the cold surfaces, thus acting as pumps. It is detected when the pressure in the OVC drops when the fridge is isolated, that is, when PV5 is shut.

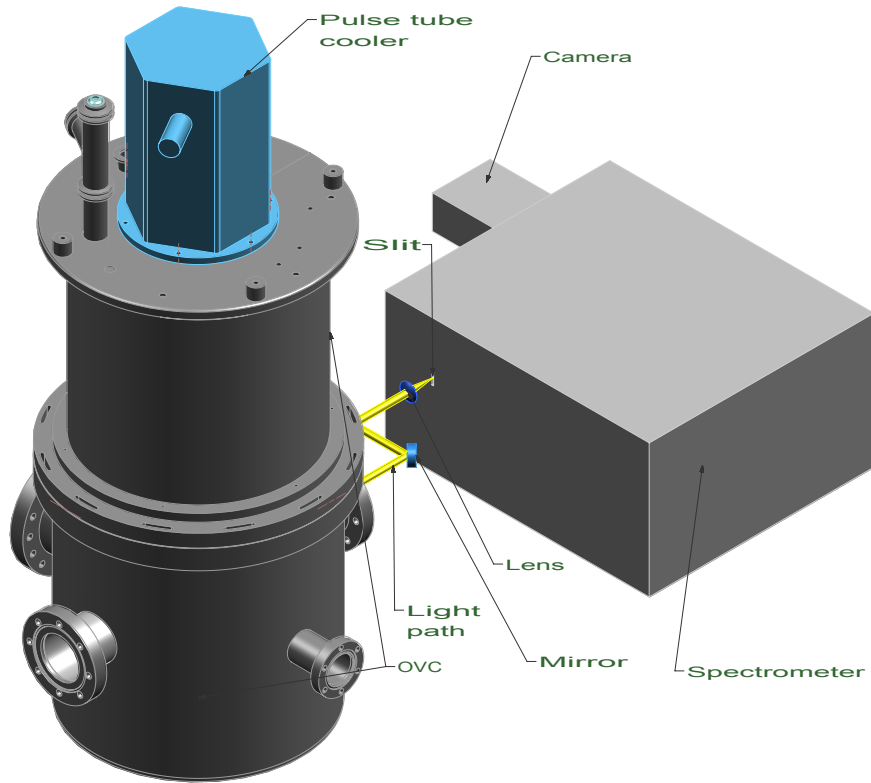


Figure 3.4: Heliox AC-V refrigerator sending light into the spectrometer via mirrors and a lens.

fridge was designed and assembled by Oxford Instruments (O. I.). The equipment was used off-the-shelf with minor modifications described below.

3.8 Cryogenic spark cell

Technical drawings for the cell and other utilized components have been provided in Appendix I.

The spark cell, the heart of this experiment, builds upon the experience gained from the Grenoble group [80]. The original Grenoble design was amended rather than reproduced; the main difference is that the new spark cell is smaller than the original cell; the chief reason to do so was to reduce the plane-tip separation (6-10 mm in that design).

A first, exploratory cell was built using stainless steel and was used to conduct gas-phase experiments on it. This cell featured a tip-plane separation of about 4-6 mm and it was found that it was possible to generate an electrical discharge under those conditions.

A brand new cell was designed to carry out the sub/supercritical experiments. The material chosen for building the cell is OFHC for its exceptionally high thermal conductivity at low temperatures. The physical dimensions of the cell were kept to

a minimum in order to enhance cooling; the available volume for the helium is 4 ml.

The cell has to meet some requirements for this experiment; such requirements impose constraints on the design of the cell. They can be summarized as follows:

1. The cell is to be bolted on to the pot of the Heliox refrigerator.
2. A low ignition voltage, which in turn implies a low Joule heating.
3. Minimization of the consumption of helium.
4. Minimization of thermal load due to mass of cell (lump of copper and attached accessories).

The spark cell features four ports or windows. In one of the windows sits a flange with a system to feed (helium) gas into the cell; the next two, opposing flanges accommodate a plane-tip electrode configuration with typical separations of 4-6 mm. The flat electrode and the tip bearer are both made of stainless steel and the former has cylindrical symmetry; the tips are made of tungsten and have an initial tip radius as good as 200-250 nm (from TEM). The plane electrode is earthed while the tip electrode can be brought to a positive or negative potential (or polarity). This cell is able to produce currents of the order of hundreds of μA (at room temperature), it is able to sustain the discharge for a several hours and gets a discharge in liquid helium started at approximately 10 kV (negative polarity)⁷. See Fig. 3.5. The manufacturing of the tips will be explained in Section 3.13. On the fourth flange of the cell, opposite the gas inlet flange, sits a lens which couples the light out of the setup.



Figure 3.5: Physical implementation of the plane-tip electrode array. The tungsten tip (in black) has been spot welded on to the stainless steel pin. The flat electrode is grounded and the tip can be either at positive or negative polarity with respect to ground; in our experiments the polarity of the tip was chosen negative.

The seals are made of indium; this is a material of choice in the cryogenic regime because it provides at high pressures a low leak-rate seal and does not decay at low temperatures. The flat electrode and the tip electrode bearer are held in place by

⁷Only negative polarity is systematically investigated in this work.

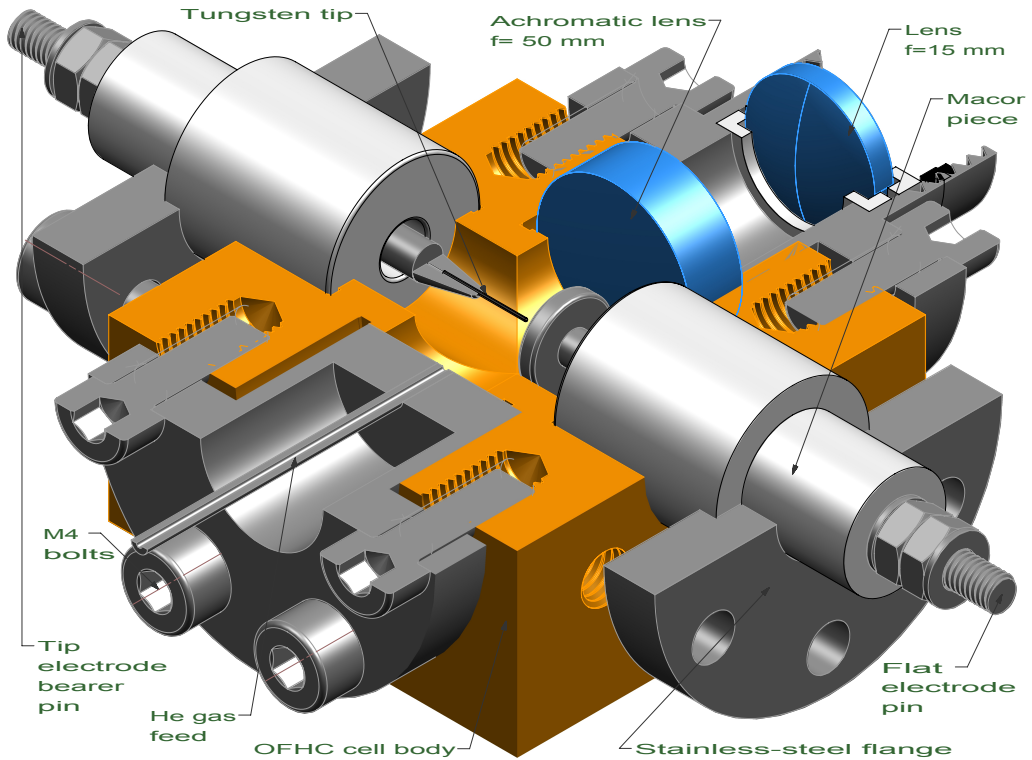


Figure 3.6: Cross-sectional view of the discharge region of the cell (assembled).

a Macor ceramic piece. Macor is both an electric and thermal insulator with little thermal expansion or outgassing [1]. Indium stretches out upon compression either by the macor ceramics holding the electrodes or the lens. A cross-section of the copper cell design is shown in Fig. 3.6 (the indium seals are not shown).

3.9 Optical layout

In this experiment the collection of light was maximized under the size constraints imposed by the existing refrigerator.

Minimizing the volume of helium inside the cell implies placing a lens as close as possible to the discharge region; if the focal length is greater than the distance between lens and object (the discharge), then a virtual image is generated further back in the discharge region (see Fig. 3.7), which means that light rays diverge off the lens and some light is lost on its way to the next lens.

The bores on the faces of the cell are 15 mm-diameter. The distance between the tip and the first optics is 8 mm. No lens with a smaller focal-length f was available. An $f = 50$ mm achromatic lens (Edmund Optics Dwg. No. 47702INK) was placed, thereby generating a virtual image of the discharge.

Then, an $f = 15$ mm lens (Thorlabs Part No. LB1092) collects the divergent light from the first lens and focuses it right onto a pinhole (radius of the pinhole is

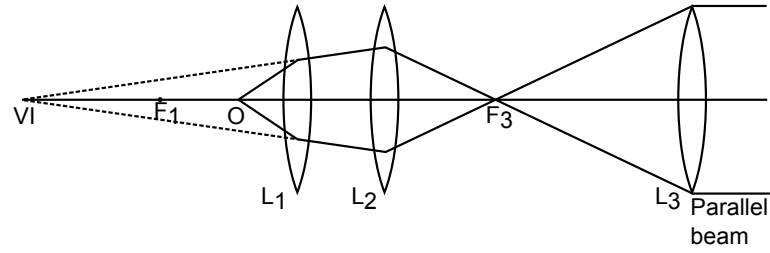


Figure 3.7: Schematic diagram of the optical system designed to couple the discharge light out of the vacuum chamber in the experiment. An object (O), the electrical discharge, placed between the focal point F_1 and the lens L_1 will produce a virtual image (VI) that will be picked up by L_2 . Light is then focused on the optical axis at a point that will correspond to F_3 , the focal point of a final lens L_3 . The focal lengths of the lenses are, from left to right, 50, 15, and 50 mm.

1 mm and so this is the size of the aperture connecting the cold pot to the ambient temperature world) at the flange on the first heatshield (thus minimizing the impact of the 300 K radiation). Light is then collected by a third $f = 50$ mm achromatic lens (again an Edmund Optics Dwg. No. 47702INK) placed such that its focal point matches the pinhole position. The setup is displayed in Fig. 3.8.

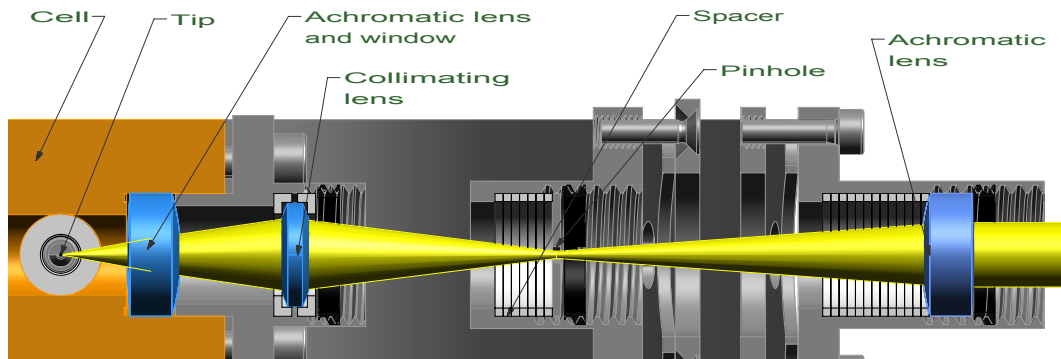


Figure 3.8: Cross-sectional view of the cryogenic setup and physical realization of the system sketched in Fig. 3.7. An electrical discharge is generated in the immediate vicinity of the tungsten tip and the light is first picked up by an achromatic lens ($f = 50$ mm) that also serves as the sealing interface. A second collimating lens (this lens is 12.7 mm diameter and thus it was necessary to build a holder for it to fit into the 15 mm bores) picks up the light and focuses it into a pinhole (designed to prevent room temperature radiation from entering the setup) from where it is then picked by a final lens that produces parallel light.

In conclusion, the optical layout is constrained by the dimensions of the cell, the cryostat, and the separation of the heatshields; another more practical constraint is the availability of focal lengths and diameters of lenses from the manufacturers. The focal lengths and relative distances between lenses are chosen so as to produce a beam of parallel light.

Once the light is coupled out the vacuum chamber it is steered by a couple of mir-

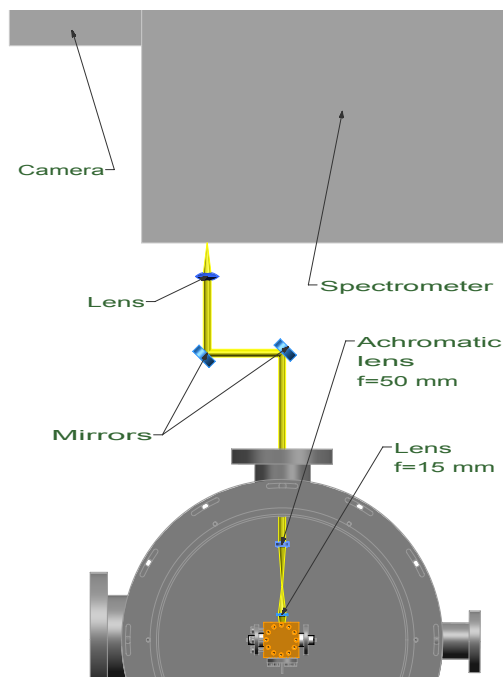


Figure 3.9: Top view of the light path. Items from the inside of the fridge have been hidden for visualization purposes.

rors and then collected into a Czerny-Turner spectrograph [27] (Andor Technology Shamrock SR303i), which resolves incoming light via a diffraction grating.

Spectra are recorded on a CCD chip (Andor CCD-12855 in the Andor iDus Camera DV420) and stored in a computer for analysis. The CCD camera is cooled down to -65°C to reduce shot noise.

A top view of the optical setup is shown in Fig. 3.9.

3.10 Gas installation

The Heliox refrigerator utilized in this experiment did not include a built-in gas supply line so a gas feed was specifically built for it. Several problems were overcome, namely: to design a setup which could handle large pressures (100 bar at most), purity and an acceptable leak rate. The first problem was solved by using stainless steel tubing; the second was solved by using N6 helium, and the third one by using standard Swagelok seals. A measurement of the leak rate in the pressurized gas line via a sniffer attached to a leak detector yielded a leak rate less than 1×10^{-8} mbar l/s. Alternatively, it was observed that the pressure in the gas line remained constant (excluding fluctuations of approximately ± 0.050 bar) over a span of time of weeks.

A diagram of the gas line used for this experiment is shown in Fig. 3.10.

A Swagelok 6 mm O.D. (outer diameter) stainless-steel pipe was chosen to ac-

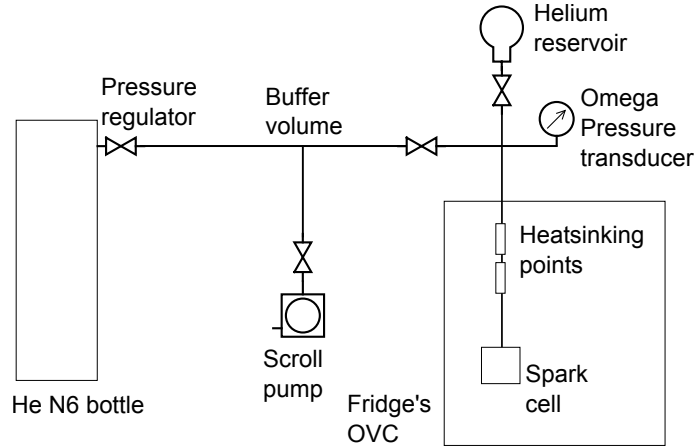


Figure 3.10: Schematic diagram of the gas installation.

commodate the gases used in the experiment.

The gas line can be divided schematically into two parts, namely: the pumping/helium supply part and the fridge part. They can be conveniently detached from each other as the fridge has to be opened and lifted on occasion. They are communicated by a buffer volume.

The pumping/supply section of the helium gas supply line features a mechanical pump, an N6 helium bottle, a Harris pressure regulator (delivering up to 40 bar) attached to it; the flow of gas is controlled by a series of ball valves.

The refrigerator part of the gas installation features a cross; the first port is connected to the buffer volume; the outlet opposite leads to the Omega pressure transducer. Opposite the fridge stands a 0.3 litre bottle controlled by a ball valve (the bottle relieves the pressure in the cell without losing helium to atmosphere and thus contaminating the line). The fourth outlet accommodates a gas inlet system built for the Heliox cryostat.

Said gas inlet system starts off with a sector of 6 mm pipe welded to a 25 KF flange that will make the vacuum seal. In the interior of the fridge, the 6 mm pipe is adapted into a 3 meter- $1/16$ " O.D. pipe (0.020" wall thickness)⁸. This thin pipe is heatsunk at the 80 K and 4 K stages using copper bobbins. Cf. Fig. 3.12. The pipe is then connected to the cell.

There is a safety concern that has to be addressed by the plumbing installation. Due to the large density of liquid helium (Cf. Appendix D), if liquid helium gets warmed up quickly without the pressure in the gas line being properly relieved (this is a hazard that may arise if the refrigerator operates unattended), then pressure can surge up to very high values (800 bar in our case) thus bursting the gas line. One way out of this problem is to let the helium expand into the bottle in Fig. 3.10; another way to solve this issue is to install a safety pressure-relief valve.

⁸Swagelok part number SS-T1-S-020-6ME.

3.11 Thermometer and pressure transducer

For thermometry purposes a Cernox CX-1030-CU-HT0.3L resistor has been chosen. This resistor can measure temperatures in a range of 300 mK- 325 K. The sensor has been factory-calibrated: above 0.65 K the calibration is based on the International Temperature Scale of 1990 (ITS-90); for temperatures below 0.65 K, the calibration is based upon the Provisional Low Temperature Scale of 2000 (PLTS 2000). The accuracy of the sensor depends on the temperature being measured. At 0.3 K its accuracy is ± 3 mK; at 300 K, ± 5 mK [4]. The sensor was mounted on the side of the cell as will be explained in Section 3.14.

For measuring the pressure in the gas line we employed a PXM409-USBH Omega transducer (0-100 bar absolute pressure USBH 0.14). It features 1000 readings per second, a USB interface for pressure-readout. This pressure transducer is again factory-calibrated and its accuracy is 0.08% BSL⁹ (linearity, hysteresis and repeatability combined) [2].

3.12 Electrical layout

The electrical installation of this experiment consists of a tip-plane electrode array connected to a high-voltage ammeter and voltmeter. The measurement of voltage and current is important insofar as it enables us to estimate the Joule heating, and furthermore, a current measurement is indicative of changes in the phase of helium: in the gas-phase, typical currents in the setup can be as high as 300 μA ; in the subcritical phase, the current in a stable discharge is 1 μA , at most. Finally, by measuring both magnitudes it is possible to calculate the mobility as per Eq. 2.1.

An electrical diagram of the experiment is shown in Fig. 3.11.

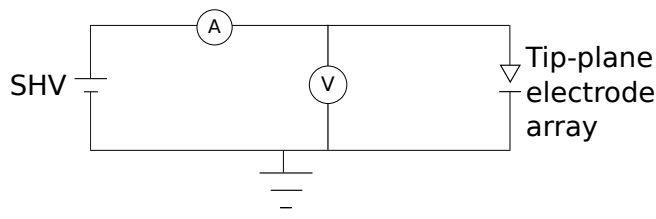


Figure 3.11: Electric diagram of the experiment. The construction and design of an ammeter and voltmeter suitable for high-voltage uses such as the present one is detailed in Appendix G.

⁹Best fit straight line.

3.13 Preparation of the tip

The procedure for preparing the tip is based on [83]. The tips utilized in the present experiment were prepared by Dr Mark Watkins and the then project student Naomi Vellody Williams.

The preparation of a typical tip can be summarized as follows: a tungsten rod (100-280 μm diameter) was submerged into a solution of sodium hydroxide (NaOH). An electric current (with voltages between 5 and 10 V) was passed through it using tungsten as the cathode and a graphite electrode as the anode. Only a couple of millimeters of tungsten wire need to be submerged into the solution. Typical etching times are approximately 30 seconds.

The free parameters in the tip preparation process are the gauge of the tungsten wire, the concentration of NaOH and the applied voltage. It was found that different combinations of concentrations and voltages produce different radii of curvature of the tip. Typical voltages were 6-10 V (dc) for a couple of seconds only; concentrations were on the order of 4 mol/dm³ and radii were about 100 nm.

By varying the above parameters a set of tips with radii in the range 100-280 nm were prepared.

Tips experience erosion during the course of the experiments as can be seen in Fig. H.1 in Appendix H.

3.14 Assembly of the setup

3.14.1 Assembly of the spark cell

This Section describes the logical steps to put together the setup that makes up this experiment.

The first component to be put together is the cell. The order in which the ports are assembled is not important although in practice it may be more convenient to start with the optical port; it is also noteworthy that our particular copper cell has a 180° symmetry about the origin, which means that opposite faces of the cell are identical whereas adjacent faces are not.

First off, an indium gasket with dimensions 15 mm O.D., 13 mm I.D. and (typically) 1 mm-thick has to be cut; this dimensions correspond to the size of the hole on the faces of the copper cell. The achromatic lens then sits against the indium gasket. The first lens to be reached by the emitted light has the double purpose of steering the beam and also performing the seal (in previous experiments by the Grenoble group it was found feasible to use an achromatic doublet to perform the seal). The lens holder is then inserted into the bore with a thin (1 mm-thick) PTFE

spacer between them. The array is then evenly pressed and fixed into position by tightening the M4 screws on the face of the cell.

The next port to be done can be either the one for the flat electrode or the tip electrode. The tungsten tip was spot welded on the tip electrode bearer shown in Fig. 3.6. The pins (either the tip or the flat electrodes) were placed into position by pressing against an inner face of the macor pieces (for which an indium seal is also required). Then an indium gasket per electrode and the macor piece (including the electrode) were inserted into the bore and pressed against the cell via the stainless steel flange as per Fig. 3.6.

The gas feed was inserted into the corresponding bore and pressed against the cell in order to make flow the indium seal by employing fasteners on the corresponding side of the cell.

Given the dimensions of the cell employed, M4 fasteners are used on its walls. Belvoir washers were utilized on the sides of the cell; they feature a spring mechanism that is useful in the cryogenic regime.

Once the cell has been put together it is convenient to link it to a leak detector to investigate leaks in the setup.

3.14.2 Assembly of the rest of the setup

The copper cell was mounted onto the fridge via the “concentric-eccentric” adapter piece made also from the copper. Cf. Appendix I. The faces of each component were wiped off with acetone. The interfaces were generously rubbed off with cryogenic grease Apiezon-N. Metric brass fasteners were used to screw the copper parts into position; the choice of brass is recommended due to its softness.

Once the cell has been put in place the thermometer (previously wiped off with acetone and rubbed off with Apiezon-N too) is bolted on one of its faces. The thermometer cable has to be heatsunk as described above (usually at the first and second stages as well as at the pot of the fridge).

Preliminary experiments showed that the cooling power of the ^3He pot was insufficient to cope with the Joule heating from the discharge if experiments in the liquid phase were to be conducted; the reason for liquid helium being challenging to break (in the sense of a dielectric) lies in its high dielectric strength [22]. Therefore, in order to break liquid helium [36] without boiling it, copper braids were used to thermally link the cell and the second stage, thereby exploiting the cooling power of the latter, and furnishing a constant base temperature of 3.2 K.

Lakeshore phosphor-bronze cables have been chosen to accommodate the high voltages utilized. Customarily they have to be heatsunk in the usual fashion; however, it has been found that the thickness of polyimide in the utilized cables was

not able to prevent short-circuits to ground that arise at potential differences of about 4 kV (in the present setup it was found that in order to break liquid helium at least 10 kV negative polarity were necessary). In this instance we have utilized PTFE-sleeving, which cannot be heatsunk.

Heatshields are mounted on the first and second stages of the fridge. They accommodate cylindrical inserts that in turn accommodate lenses and 1 mm-thick plastic spacers. Given the dimensions of this specific setup, as many spacers as per Fig. 3.8 are necessary.

The innermost, gold-coated heatshield normally sits around the pot of the fridge; however, due to space limitations this heatshield has been removed for the duration of the experiments. The only heatshields that remain in place are those on the first and second stages.

The outer vacuum chamber or vacuum-housing can then be mounted on to a table; the chamber is fitted with a window for coupling out the light, an electrical feedthrough socket and a Penning gauge to assess the vacuum in the fridge. Once the insert of the fridge is ready it can then be lifted via a crane and dropped into the vacuum chamber.

We can summarize the features of the designed system as follows:

- The ability to cool down the system to at least 3 K and ignite an electrical discharge at those low temperatures.
- Minimization of the impact from the thermal radiation at 300 K.
- Minimization of the dimensions of the physical setup to enhance cooling.

Fig. 3.12 shows a cross-sectional view of the internal components of the cryostat.

3.15 Experimental procedure

The gas line was cleaned with the vacuum pump and then purged several times with 3-10 bar of N6 He. This helium features a very high purity yet it still contains impurities such as hydrogen. When the setup is cold (typically below 20 K), all the remaining impurities have been frozen and are not apparent in the emission spectrum, as will be seen later.

The pumping-down routine was then started. Cf. Appendix A for an explanation of the operation of the pumping mechanism.

The optical system can be aligned while the pumping is being carried out. Outside the vacuum chamber, on the experimental table, lies an optical breadboard that accommodates two mirrors to steer the (parallel) light beam onto a lens of an appropriate focal length (in our case 150 mm). Cf. Fig. 3.4. This lens focuses

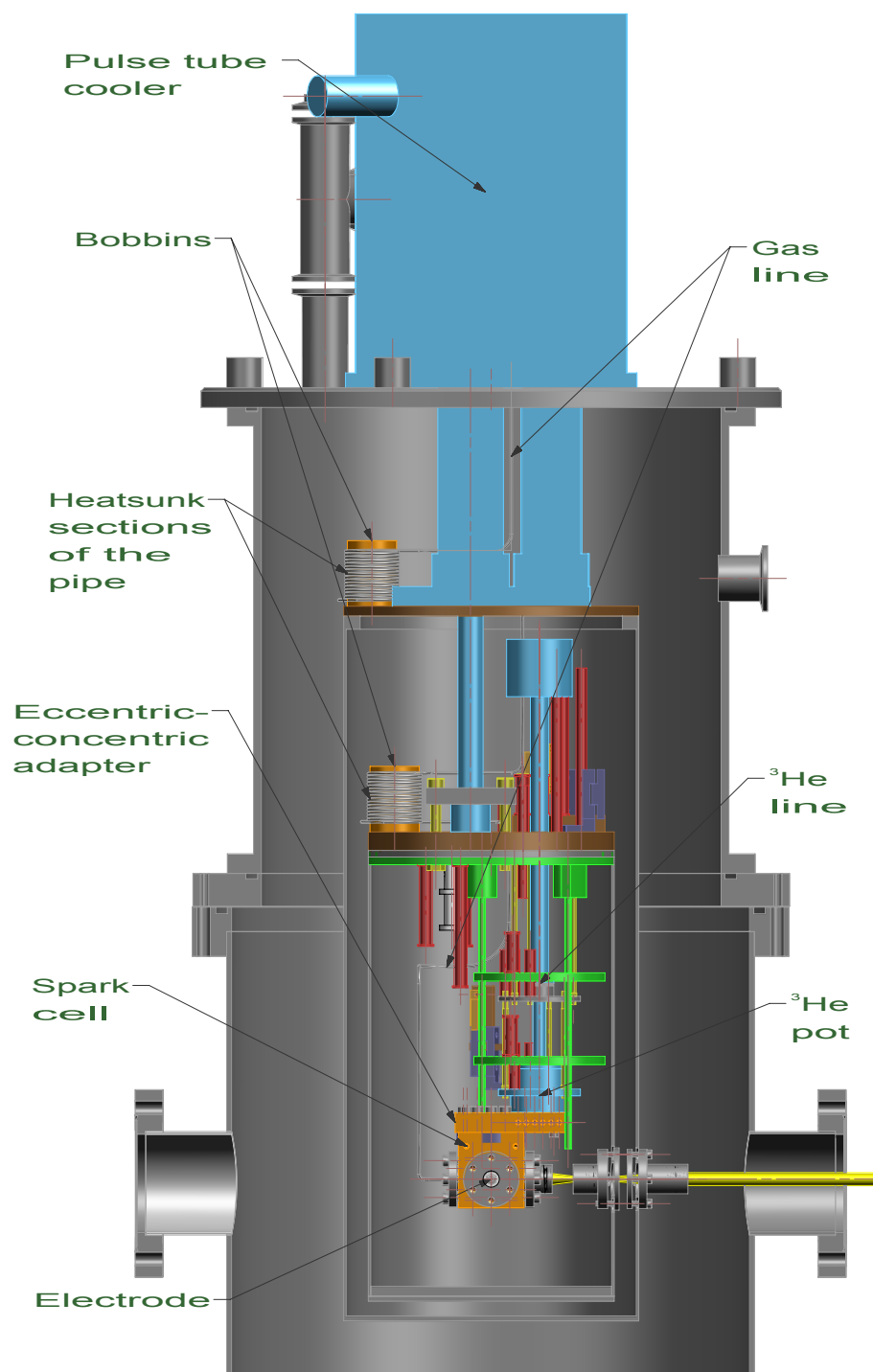


Figure 3.12: Assembled cryostat. Electrical cables are omitted. The inner section of the tubing is shown to illustrate the concept of heatsinking applied to the plumbing of the experiment.

the beam onto the slit of the spectrograph; the lens is conveniently placed on two crossed-linear translation stages. The tip-plane corona discharge represents an almost ideal point-like light source. The idea of alignment was therefore to image the tip on the entrance slit of the spectrometer.

The method we have chosen to optimize the alignment is as follows: start a corona discharge, get the spectrograph into the imaging mode (by selecting the zero-th order of the diffraction grating, making it effectively a mirror). Then place the image of the discharge onto the center of the slit; afterwards, manipulate the mirrors, lens and spectrograph to get a spot as round as possible¹⁰. For the final step of the alignment the distance between the lens and the slit of the spectrometer can be finely tuned with the translation stage, thereby maximizing the light-collection efficiency. It is important to mention that a few iterations of this process have to be carried out once the cryostat has achieved low temperatures as the components suffer contractions that shift the discharge by approximately 1 mm and thus modify the alignment. See Fig. 3.13.

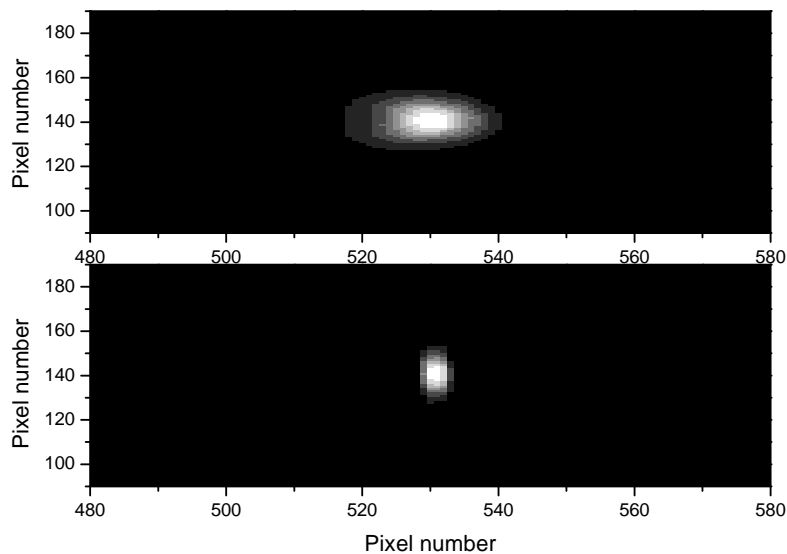


Figure 3.13: Final stage of the alignment procedure in the cryogenic regime (3.5 K). Slit (fully) open at 2,500 μm (top panel) and adjusted to 100 μm (bottom panel). The images were recorded on 10 September 2014.

Once the system is aligned the next step is to record a reference spectrum, while the refrigerator is still at room temperature. Low-pressure discharge spectra of helium were recorded by pumping on the cell while applying a high potential difference across the electrodes. Since the pumping of the cell itself is inefficient

¹⁰A rigid body possesses 6 degrees of freedom and so this alignment problem has 24 degrees of freedom.

due to the length of the gas pipe (about 3 meters), helium at a pressure of about 80 mbar remains. Emission was then recorded and stored. The spectra obtained in this fashion are glow discharge spectra of helium.

At this point the compressor was started and, a couple of minutes later, the valves controlling the cooling water were opened, as per the operation instructions of the fridge [3].

When the fridge runs in standard mode (that is, when the second stage and the ^3He pot are not thermally linked), the cooling-down process takes up to three days; when the second stage and the pot are linked the cooling-down can take just 9-10 hours.

It was found that in the unlinked setup, by operating the heater of the pot and by adjusting the voltage and current, it was easier to systematically record spectra in the supercritical phase of helium ($T = 5.2 - 20$ K). On the other hand, changing the temperature of the pot via the heater beyond the critical temperature in the “short-circuited” setup proved more challenging but less so below the critical temperature; hence, the linked setup was deemed more convenient for spectra acquisition in the subcritical phase ($T < 5.2$ K).

While operating the fridge in the “short-circuited” mode, liquid helium was condensed in the following fashion: once the setup has reached base temperature (~ 3.2 K and about 0.150 bar), additional gas was added to the line. This action increases temperature temporarily but the action of the refrigerator took it back to base temperature. The process was repeated until the point that small increments in the amount of gas in the gas line did not produce further increases in the pressure of the line. This is the signature of the helium lying on the saturated vapor pressure (SVP) curve of the phase diagram (see Fig. 1.2). More helium needs then to be added to the line until an increase change in pressure is observed (after stabilization at base temperature). When the pressure transducer indicates a pressure above the SVP and T is below T_c then, by definition, the liquid phase of helium has been reached.

The ignition of an electrical discharge proceeds in the same way as before. The only difference is that the ignition and stable operation voltages are both about 10 kV (in negative polarity). The current for stable operation was found to be $1 \mu\text{A}$.

3.16 Methodology of the data collection

The emission spectra were recorded using the Andor Solis software¹¹ accompanying the hardware. A high-resolution diffraction grating of 1200 grooves/mm was

¹¹version 4.19.30001.0

employed in the spectrograph; this grating is able to acquire a spectrum in a spectral range of approximately 60 nm. Successive spectra were recorded in the same experiment and then ‘stitched’ (or ‘glued’) together using the Andor Solis software.

A typical routine of exploration of the phase-space was as follows: a certain amount of helium of a certain pressure is admitted into the line. An electrical discharge is then started; typically the ignition voltages will be much higher than the minimum necessary needed to obtain a stable discharge thereby increasing the temperature, so the voltage and hence the current have to be brought down until the temperature stabilizes. Several spectra are then recorded (to ensure reproducibility). The light acquisition times usually differed from spectrum to spectrum but this parameter always ranged between a few seconds up to one and a half minutes; the choice of a particular acquisition time reflects the interplay between the need of acquiring a well resolved spectrum, the intrinsic instability of the discharge and the fluctuations in the temperature (and pressure) of the helium.

Once this is finished the temperature is varied in regular intervals via the heater at the pot of the fridge; the Joule heating did not change. This process ensures we probe the phase space by looking at points that correspond to the same number of helium atoms in the gas line; this accounts for the slant, semi-straight lines in Fig 3.14. Pressure can be added or taken out of the gas line by adding more gas or releasing helium from the gas line. Usually this was accompanied by a change of temperature. Then the recording and heater manipulation takes place again.

Using the setup and procedure described above we were able to explore the PT diagram shown in Fig 3.14. Each point in it represents a fluorescence spectrum which spans the range 300-1000 nm¹²; also each of the data points shown was acquired at least thrice in order to ensure reproducibility of our results. This methodology furnished different transitions of molecular and atomic helium¹³.

¹²This operation implies a continuous change in the orientation of the grating which naturally prompts the issue of the repositioning error of the grating. Said error was assessed by comparing the position (in pixel numbers) of notable atomic lines after a few acquisitions of spectra without modifying any other element of the optical array. It was found that the positions (in pixels) of the lines did not change, which led us to conclude that the repositioning error is negligible.

¹³This methodology in principle can also deliver the spectra of impurities such as hydrogen (this element is always present in minimum concentrations in helium N6); however, impurities are not apparent in the emission spectra at the temperatures of liquid helium

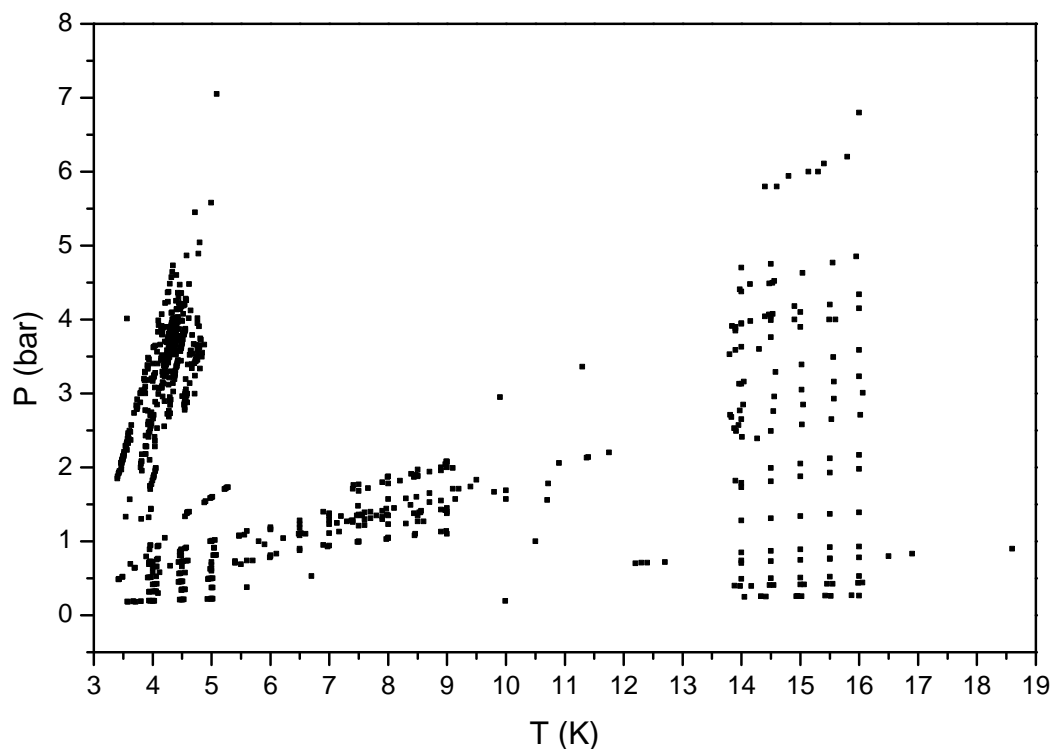


Figure 3.14: Section of the PT diagram for the liquid and supercritical phases probed in this experiment.

Chapter 4

Results and discussion

The structure of this chapter is as follows. The history of our experiments is outlined in Section 4.1, the treatment of the spectra is described in Section 4.2, spectra in different thermodynamic phases of helium as well as an analysis of said spectra are presented in Sections 4.3-4.8; we present an error analysis in Section 4.9 and a structural model that arises from our findings in Section 4.10.

In this chapter the abbreviation a.u. stands for ‘arbitrary units’.

4.1 Experimental history

The history of our experiments is outlined in this section.

In the cryogenic regime there were 3 different sets of experiments carried out in 2014 – and hence 3 calibration standards recorded under different alignment conditions. An additional experiment at 80 K was completed in 2012.

4.1.1 Experiment from 22-May-2014

This experiment was envisaged as being of an exploratory nature, to test the equipment and the data-acquisition methodology although it also allowed us to acquire the first spectra under cryogenic conditions.

The reference was recorded on 20-May-2014 (spectrum 5) while the setup was at room temperature. The results of the calibration¹ (slope and intercept, respectively) are $m = 0.05797 \text{ nm/row}^2$, $b = 298.44 \text{ nm}$. The recalibration is achieved by using the formula $\lambda_{\text{recal}} = mn + b$, where m and b correspond to the slopes and intercepts given in this Section and n is the row number of each datafile.

The first spectra in the sub/supercritical regime were recorded on 22-May-2014.

¹The utilized lines and the calibration procedure will be explained in Section 4.3.

²The unit for the slope is formally just nm, but the row number is added for clarity of the exposition.

This experiment ended prematurely due to an electrical short-circuit which occurred due to the formvar insulation of the cryogenic cable not being rated for potential differences larger than 2 kV (necessary for passing an electric current across liquid helium). To overcome this limitation, the cryogenic cable was sleeved with PTFE, as has been explained above.

4.1.2 Supercritical gas phase data

Once the experimental setup was shown to work we set out to record data in the supercritical phase of helium. The rationale for this decision is that for breaking (as a dielectric) gaseous helium, lower voltages are required and so the risk of an electrical short-circuit is lower.

The reference discharge glow spectra were recorded on 3-June-2014, while the setup was at room temperature. The result of the calibration is $m = 0.05799$ nm/row, $b = 298.28$ nm.

The setup was then brought down to ~ 4 K. No realignment was carried out. The recording of spectra under cryogenic conditions started on 6-June-2014.

The experiment ended on 22-July-2014.

4.1.3 Liquid phase data

In order to probe the normal liquid phase of helium using the corona discharge method the insulation of the cables was improved by sleeving the cables with PTFE tubing. It provided insulation for potential differences of up to 10 kV with respect to ground. For exploring the subcritical phase of helium it was also found necessary to thermally bridge the second stage of the refrigerator and the pot.

The reference discharge glow spectra were recorded on the 8-Sept 2014, while the setup was at room temperature (spectra 7-11).

The cooling started on 9-Sept-2014. Then, on 10-Sept-2014 the position of the light spot on the entrance slit was readjusted. This is done to make up for a mechanical displacement of the source of light due to the cooling.

Because of said displacement it was necessary to recalibrate the spectrometer and to record a spectrum under the exact same thermodynamic conditions than a spectrum from the previous experiment (supercritical phase); the recalibration standard obtained in this fashion for the liquid phase data can then be used on the rest of the liquid phase data.

We have chosen for that effect spectrum 19 from 6-June-2014 (at 5 K, 0.6 bar) and spectra 63-68 from 11-Sept-2014 (at 5 K, 0.627 bar). The recalibration parameters turn out to be $m = 0.05798$ nm/row, $b = 298.57$ nm.

On 16-Sept-2014 the first spectrum in the normal liquid phase and with negative polarity was recorded. It was found that the tip voltage for stable emission was -10 kV; the flat electrode was earthed.

The experiment ended on 24-Sept-2014.

4.1.4 80 K data

This data set was recorded in 2012 under a methodology different than that used in 2014. Overview, high-resolution spectra were recorded at 2, 4, 6, 8, 10, 14, 20 and 25 bar. Each data file has 7,761 rows. There is no glow discharge reference; instead, the reference was obtained by interpolation of the spectra to 0 bar. The recalibration parameters are $m = 0.0592$ nm/row, $b = 367.26$ nm.

4.2 Treatment of the spectra

The raw spectra obtained directly from the spectrometer are approximately calibrated since the spacing of the grooves and the central wavelength (via the orientation of the grating) are known. However, in a high-resolution spectroscopy experiment more precision is needed. For such an endeavor we recorded glow-discharge spectra to be used as (re)calibration standards. Under glow discharge conditions the pressure is so low that the linewidth is governed by the spectrometer features (mainly slit opening). These glow discharge spectra were used as a reference standard for the position of the spectral lines and the resolving power of the spectrometer; they were calibrated using the positions of helium atomic lines reported in the literature [72].

It was observed during experimentation that the exact position of the spectral lines depends, among other factors, on the alignment of the optics; hence, before recalibrating the spectra, they are dependent on the alignment which will naturally change from experiment to experiment (an “experiment” means, in the present context, turning the fridge on and hence start the cooling). After recalibration (the calibration standard having been recorded under the same alignment conditions than the spectra it will act upon), the spectra become “alignment-independent” and they constitute the basis of the work presented in this chapter. The ‘stitching’ procedure explained in Section 3.16 does not affect the (re)calibration.

Intensities have been normalized to the most intense peak in the spectrum, that normally being the 706 nm line of atomic helium.

The spectrograph can be used in either imaging mode or spectra-acquisition mode, and so the files obtained via the spectrograph can be either images or spectra. They were labeled using a simple scheme – “imag” followed by a number for

images and “spec” followed by a number for spectra. The data files are organized in chronological order. Files pertaining to fluorescence spectra span the range 300-1000 nm and consist of 12,081 rows. A linear relationship between the row number in the data file and the wavelength was observed and so a typical recalibration consists of a (linear) fit of a graph featuring the peak positions in wavelengths vs. row number for the calibration. See Fig. 4.1.

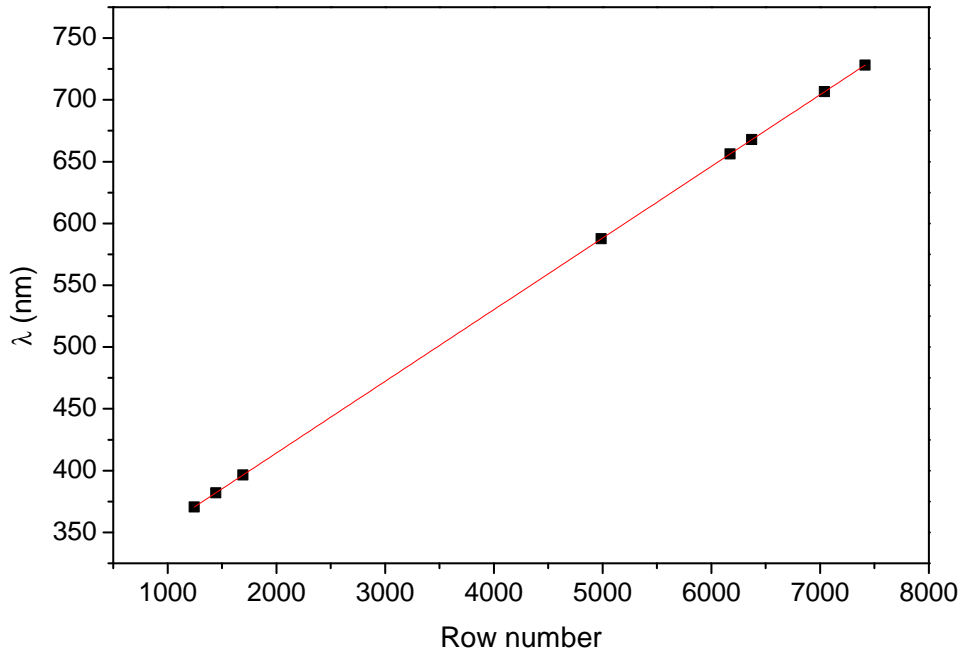


Figure 4.1: Recalibrated wavelength versus row number in the glow discharge spectrum from 6-Jun-2014. Linear fit added for clarity.

The methodology to analyze the data is the following: the region of interest was defined to include the $d^3\Sigma_u^+ \rightarrow b^3\Pi_g$ (0-0) transition and a lorentzian line profile was fitted to its Q- and P-branches, subtracting a constant baseline when necessary. Then the lineshift $\Delta\lambda$ of the lines of the transition (with respect to the calibration standard) measured using the P- and Q-branches as well as the linewidth of each rotational line, quantified via the full-width half maximum (FWHM) of the lorentzian lines, are both investigated as a function of pressure for each isotherm. The open-source curve fitting software Fityk v. 0.9.8 and 1.2.1 was chosen to carry out the fitting procedure.

An example of the fitting is shown in Fig. 4.2.

The raw spectra from the spectrograph can be interpreted as the convolution of the physical spectrum and the profile of the spectrograph’s slit [14]. If the real spectrum and the profile of the slit are assumed to bear a lorentzian line profile³,

³An ideal slit would bear a rectangular line profile; however, a lorentzian or a gaussian bear more resemblance to an actual slit.

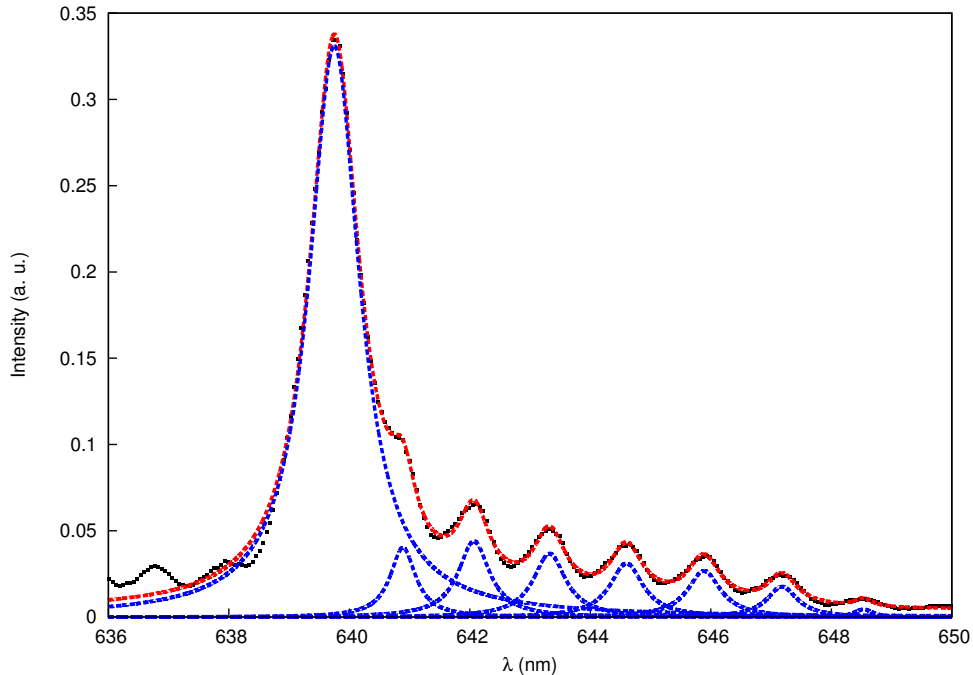


Figure 4.2: Fit of spectrum 4 from 22-Sept-2014 ($T = 3.8$ K, $P = 2.30$ bar) by Fityk. The calibrated datafile is represented in black dots; the overall fit is represented by a red-dashed line and the lorentzian components by blue-dashed lines.

then the convolution is another lorentzian whose linewidth equals the sum of the linewidths of the component linewidths⁴. The analogous result for the convolution of two gaussians would produce a pythagorean relationship between the three linewidths involved; a lorentzian line profile is thus chosen in view of the simpler relationship between convoluting linewidths discussed above.

The analysis presented in this chapter is centered around the $d^3\Sigma_u^+ \rightarrow b^3\Pi_g$ (0-0) transition. This is a transition of interest because it is known to show up in the spectrum of liquid helium and also because it has been extensively reviewed in the literature [28, 81, 97, 41, 40, 68, 25, 106, 19].

4.3 Glow discharge calibration spectra and normalization

An example of a recalibrated glow discharge spectrum is shown in Fig. 4.3.

The lines in this glow discharge spectrum have been matched to the positions of the atomic lines from NIST [72]. The lines employed to recalibrate our spectra are shown in Table 4.1.

⁴This fact can be proved via a simple algebraic calculation.

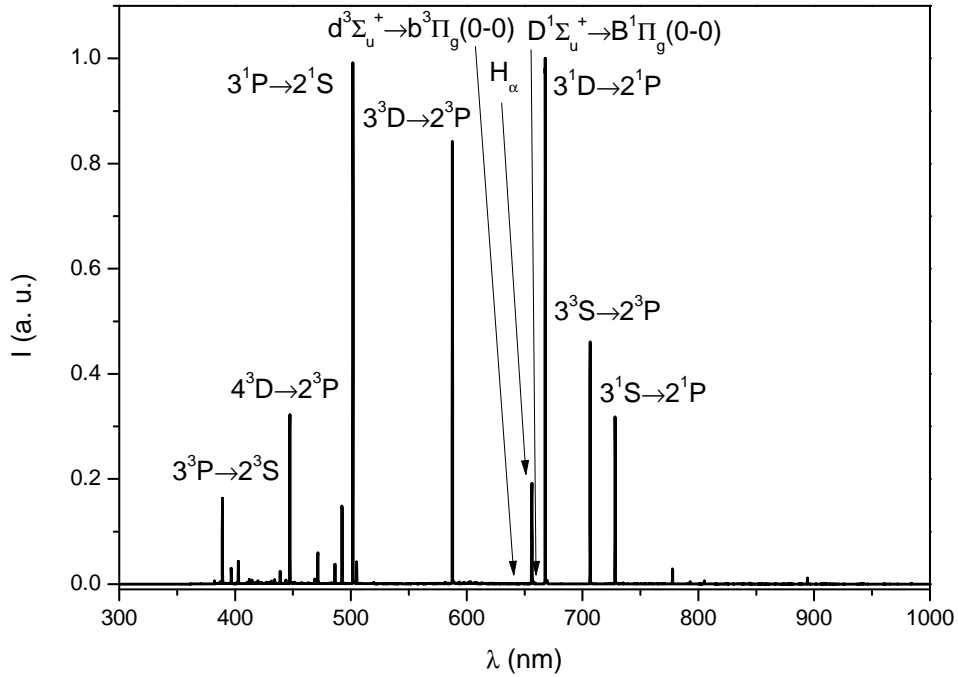


Figure 4.3: Overview of a normalized and calibrated glow discharge spectrum. This spectrum was recorded on 8 September 2014 at room temperature and at about 80 mbar. Important transitions indicated. Cf. Appendix C. Glow discharge spectra like this were utilized to recalibrate corona discharge spectra.

NIST wavelength (nm)	Species
587.56	atomic helium
656.27	H_{α} ($n = 3 \rightarrow n = 2$, atomic hydrogen)
667.81	atomic helium
706.51	atomic helium
728.13	atomic helium

Table 4.1: Transitions utilized for recalibrating the spectra. Hydrogen makes it to this list because H impurities are inevitably contained in N6 He, but disappear at low temperatures (below 20 K) upon solidification.

4.3.1 Line positions of the molecular transition of interest

In this subsection we shall make a digression to report the positions of the rotational lines that make up the $d^3\Sigma_u^+ \rightarrow b^3\Pi_g$ (0-0) transition obtained with the glow discharge technique described above.

Rotational line	Observed value (cm^{-1})	Ginter (cm^{-1}) [40]
P(2)	15604.22	15994.63
P(4)	15574.40	15564.60
P(6)	15543.66	15534.14
P(8)	15513.01	15503.33
P(10)	15481.99	15472.23

Table 4.2: Positions of the rotational P-lines of the transition of interest. The observed line positions exhibit a 10 cm^{-1} shift with respect to previously reported values of the line position.

From Table 4.2 it follows that there is a discrepancy in the positions of the rotational lines between the values observed in this work and those reported previously [40]. However, it should be noted that the present data is blue-shifted with respect to the reported value by a constant amount (10 cm^{-1}). On the other hand, after recalibration, the atomic lines are shifted by approximately 3 cm^{-1} with respect to the NIST values; this is the case by construction, since the atomic lines were chosen as the recalibration reference.

The exact cause of the shift is not known and it appears to be a systematic error of the measurement. Regardless, the shift does not have any implications in our results and conclusions as it only amounts to a constant offset of the spectral lines.

4.4 Gas-phase experiments

Apart from glow discharge spectra, fluorescence spectra of helium were collected in the gaseous phase at 80 K for pressures in the range 2-25 bar (approximately the pressure at which rotational resolution was lost).

During these experiments operation voltages ranged between 0.5 and 2 kV (in negative polarity) and currents ranged approximately between 18 and 460 μA .

Spectroscopic results are displayed in Figs. 4.4 and 4.5. From them we observe both line broadening and line-shift of the spectral lines and also a broad baseline and strong molecular lines.

The contributions to the linewidth observed in this phase correspond to pressure broadening. The line-shift can be explained as follows: pressure has a direct effect on the density. Higher densities mean that emitters are more strongly influenced by their surroundings. This interaction has, in turn, an effect on the potential energy

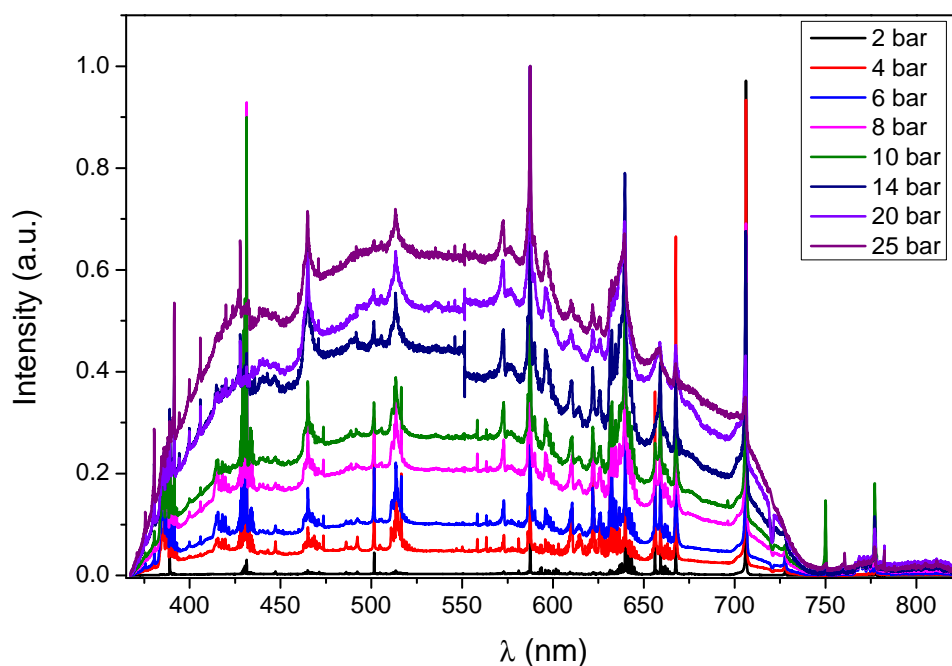


Figure 4.4: Overview of the spectra for the 80 K isotherm. The different baselines of the spectra are due to variations in the current while the spectra were being recorded.

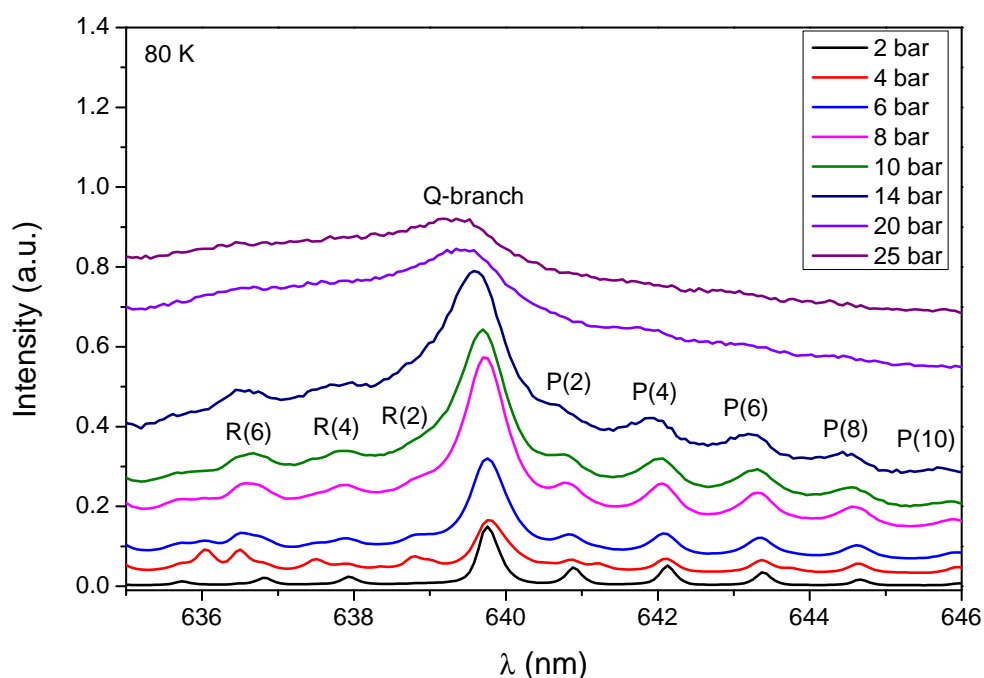


Figure 4.5: Development of the $d^3\Sigma_u^+ \rightarrow b^3\Pi_g$ (0-0) transition as a function of pressure for the 80 K isotherm. Only the 20 bar and 25 bar spectra have been shifted upwards for clarity (by 0.15 and 0.25 in a.u., respectively).

curves (of excimers) or the energy levels (of excited atoms) of both initial and final states, shifting them upwards or downwards.

Fig. 4.5 shows that rotational resolution of this transition vanishes between 14 and 20 bar. According to the ideal gas law, this corresponds to densities between 0.0013 and 0.0018 \AA^{-3} at 80 K. This finding is to be compared to the density of bulk liquid helium, namely 0.0219 \AA^{-3} . See Table E.1 in Appendix E and Fig. D.1 in Appendix D.

4.5 Supercritical phase

Fig. 4.6 defines the region of the PT diagram that in the present work is referred to as the supercritical regime.

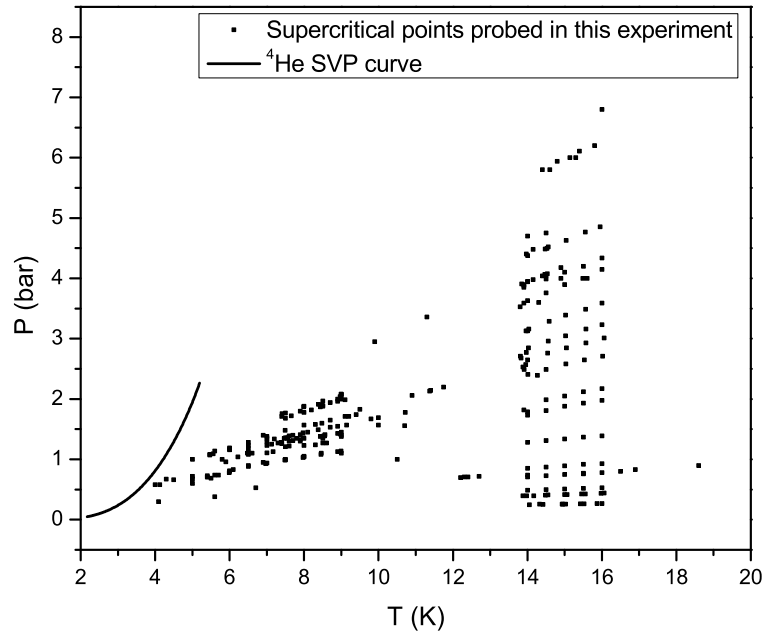


Figure 4.6: Supercritical data points from Fig. 3.14. The SVP curve of ${}^4\text{He}$ shows the location of the critical point of ${}^4\text{He}$ relative to the data points.

Experiments in the supercritical phase of helium took place at voltages between 0.50 and 1.50 kV (in negative polarity) and currents in the 6-20 μA range.

Fig. 4.7 shows rotational spectra of the $d^3\Sigma_u^+ \rightarrow b^3\Pi_g$ (0-0) transition at several pressures for the 16 K isotherm. As in the gas-phase experiments, broadening and shift of the spectral lines are observed. However, it should be noted that the rotational resolution vanishes at much earlier pressures than in the gas-phase; in the case of the 16 K isotherm shown, the rotational resolution is lost between 4.15 and

6.20 bar, which corresponds to densities between 0.0019 and 0.0028 \AA^{-3} according to the ideal gas law, which holds far away from the critical temperature of ^4He (5.13 K). At 16 K, the Q-branch broadens at a different rate than the P- and R-branches. It is also interesting to note that the rotational line P(2) merges with the Q-branch at rather low pressures compared to 80 K; no such effect is observed in the R-branch.

Following the observation of condensation of helium atoms into a cluster around positive helium ions in the supercritical phase [103], it is hypothesized that in this temperature region condensation of neutral helium atoms on single excimer molecules to clusters will begin when the pressure is large enough. At present there is no theory to ascertain what pressure that would be.

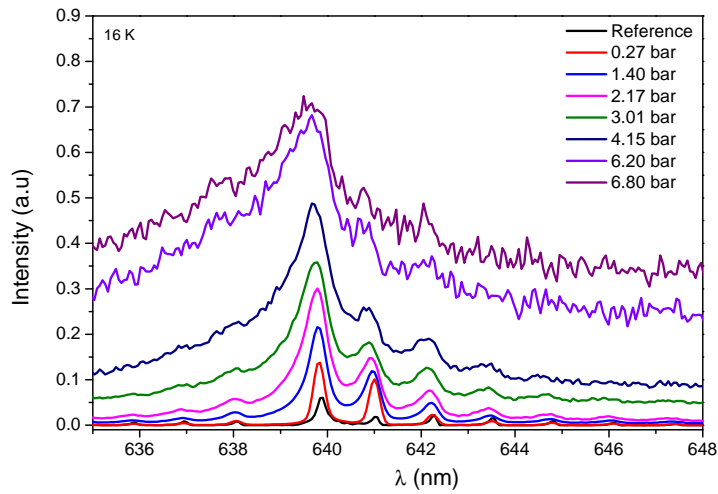


Figure 4.7: Development of the $d^3\Sigma_u^+ \rightarrow b^3\Pi_g$ (0-0) transition as a function of pressure for the 16 K isotherm. Only representative isotherms are shown. The reference spectrum has been shifted 0.019 a.u. downwards and then scaled by a factor of 3; the spectrum at 0.27 bar is unchanged; the spectrum at 1.40 bar has been scaled by a factor of 3; spectra at 2.17, 3.01 and 4.15 bar have been scaled by a factor of 4; spectra at 6.20 and 6.80 bar have been scaled by a factor of 3. Said changes have been done for visualization purposes. The reference spectrum is a glow discharge spectrum like the one in Fig. 4.3 (but recorded on 3-June-2014) and is meant to showcase an unshifted (line position-wise) benchmark spectrum of negligible broadening.

4.6 Subcritical phase (gas and normal liquid helium)

In Fig. 4.8 the points in the PT diagram that correspond to normal liquid and subcritical gaseous helium are shown; they are collectively referred to as the “subcritical phase” of helium.

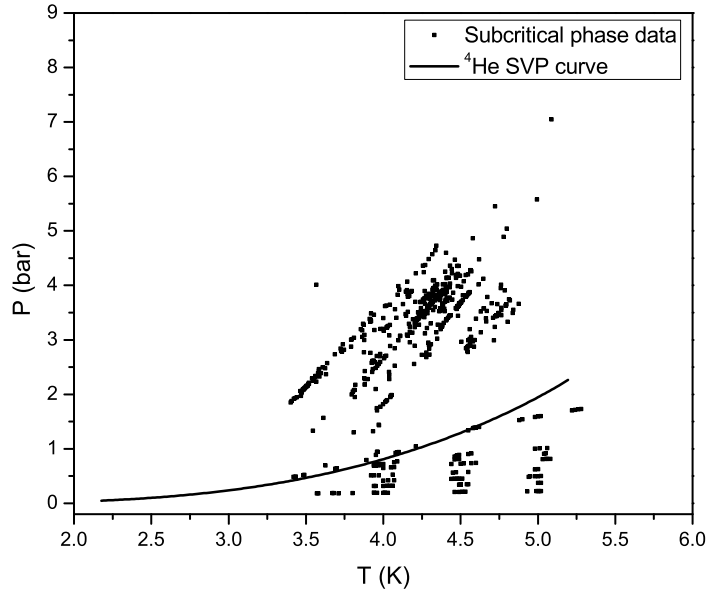


Figure 4.8: Points from Fig. 3.14 that correspond to the subcritical phase of helium (which includes either normal liquid or vapor). The SVP curve of ^4He is shown to illustrate the differences in the phases of helium as well as the position of the critical point.

Ignition voltages in the subcritical phase of helium are about 9.5 kV (in negative tip polarity). Experiments in the subcritical phase of helium took place at voltages between 9.5 and 10 kV (in negative tip polarity) and currents were measured to be less or equal than $1 \mu\text{A}$.

A typical overview spectrum at low temperatures is shown in Fig. 4.9. There is a stark contrast between it and the glow discharge spectrum (that serves as calibration standard as has been explained above) at room temperature (Fig. 4.3) and the overview spectra at 80 K (Fig. 4.4): only a few rotational and atomic transitions can be observed at the low temperatures of subcritical helium that can be characterized by the following bullet points:

1. atomic lines appear only for $n = 3$ states or lower;
2. atomic lines appear only for s (spherically symmetric) states;
3. molecular lines originating only from Σ levels appear;
4. $d^3\Sigma_u^+$ is the highest populated molecular level;

these pieces of evidence are an indication of a change of structure of the emitters.

Fig. 4.10 contains the most relevant features observed in spectra in the subcritical phase. The 3.8 K, 4 K and 5 K isotherms are featured; for each of the isotherms

P (bar)	T (K)	No. of spectrum	Date recorded	Scaling	Shift (a.u.)
0.08	300	4	03 June 2014	50.00	-0.95
0.19	3.8	1	10 September 2014	6.60	0.20
0.80	3.8	2	23 September 2014	3.84	0.53
2.77	3.8	11	18 September 2014	1.00	0.75
3.30	3.8	59	17 September 2014	2.70	1.01
0.19	4.0	21	10 September 2014	1.25	0.25
0.42	4.0	35	11 September 2014	1.44	0.45
0.95	4.0	4	23 September 2014	3.57	0.80
1.78	4.0	12	23 September 2014	4.54	0.90
2.74	4.0	26	18 September 2014	3.70	1.13
3.93	4.0	9	18 September 2014	2.85	1.35
0.22	5.0	42	10 September 2014	1.20	0.20
0.50	5.0	60	11 September 2014	1.80	0.40
1.00	5.0	24	12 September 2014	9.00	0.60
1.59	5.0	54	12 September 2014	2.50	0.90
3.55	5.0	164	19 September 2014	1.20	1.10
5.58	5.0	90	23 September 2014	5.00	1.10

Table 4.3: Scaling and shift factors for the spectra in Figs. 4.10 and 4.11. The spectrum recorded at 80 mbar corresponds to the reference glow discharge spectrum. A positive shift corresponds to a shift of the spectrum upwards (intensitywise). The spectra that were used for the analysis in the present work were obtained in different days so a systematic error in that respect can be disregarded.

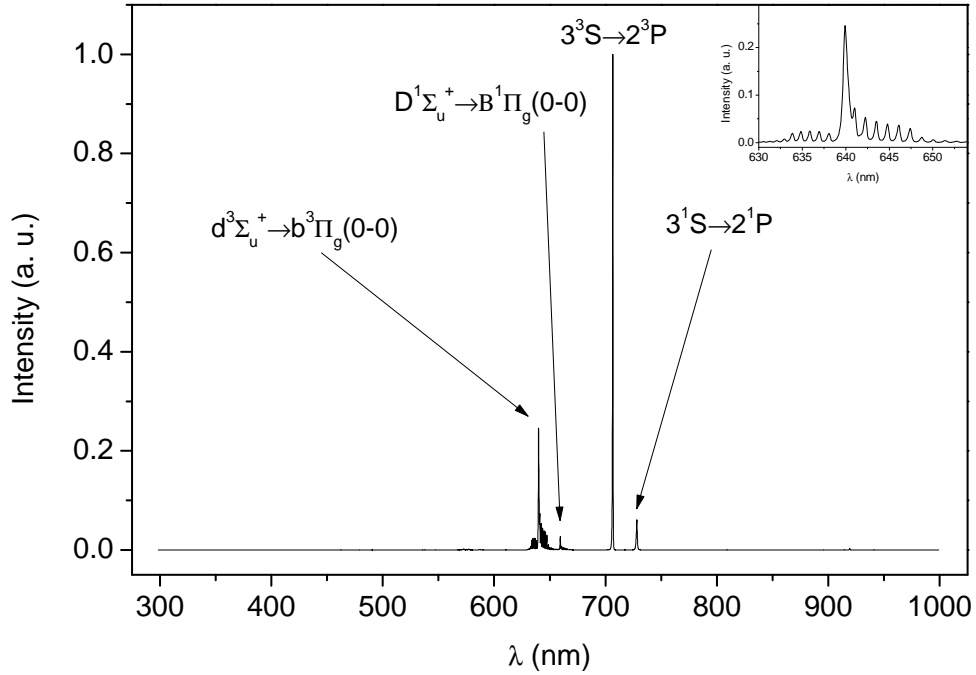


Figure 4.9: Typical emission spectrum in the cryogenic regime. The spectrum shown is “spec2” from 23-Sept-2014 ($T = 3.89$ K and $P = 0.80$ bar). Several atomic and rotational transitions have disappeared from the spectrum. In particular, the H_{α} line is gone because hydrogen impurities are frozen out at the walls of the cell. The inset shows a zoom-in of the $d^3\Sigma_u^+ \rightarrow b^3\Pi_g(0-0)$ transition.

several representative pressures have been chosen and displayed. In Fig. 4.11 a zoomed in version of Fig. 4.10 is shown.

The following trends are consistently present in the analyzed isotherms:

- The relative separations of the rotational lines of the P-branch remain unchanged, which means that rotational constants do not change, at least within the resolution of our experiment.
- The rotational line intensities do not follow a Maxwell-Boltzmann distribution [18].
- High rotational quantum states are populated (this can be seen from the existence of P(10), P(12) and so on). Hence, the rotational temperature is considerably higher than that of the surrounding environment.
- The shapes of the P- and Q-rotational lines evolve differently with pressure: at high pressures the Q-branch remains symmetric but the P-lines become asymmetric, skewed to the red. Also, at large enough pressures, P(2) and Q-branch merge completely even before the other lines lose rotational resolution.
- Rotational lines become increasingly broader as the local pressure increases.

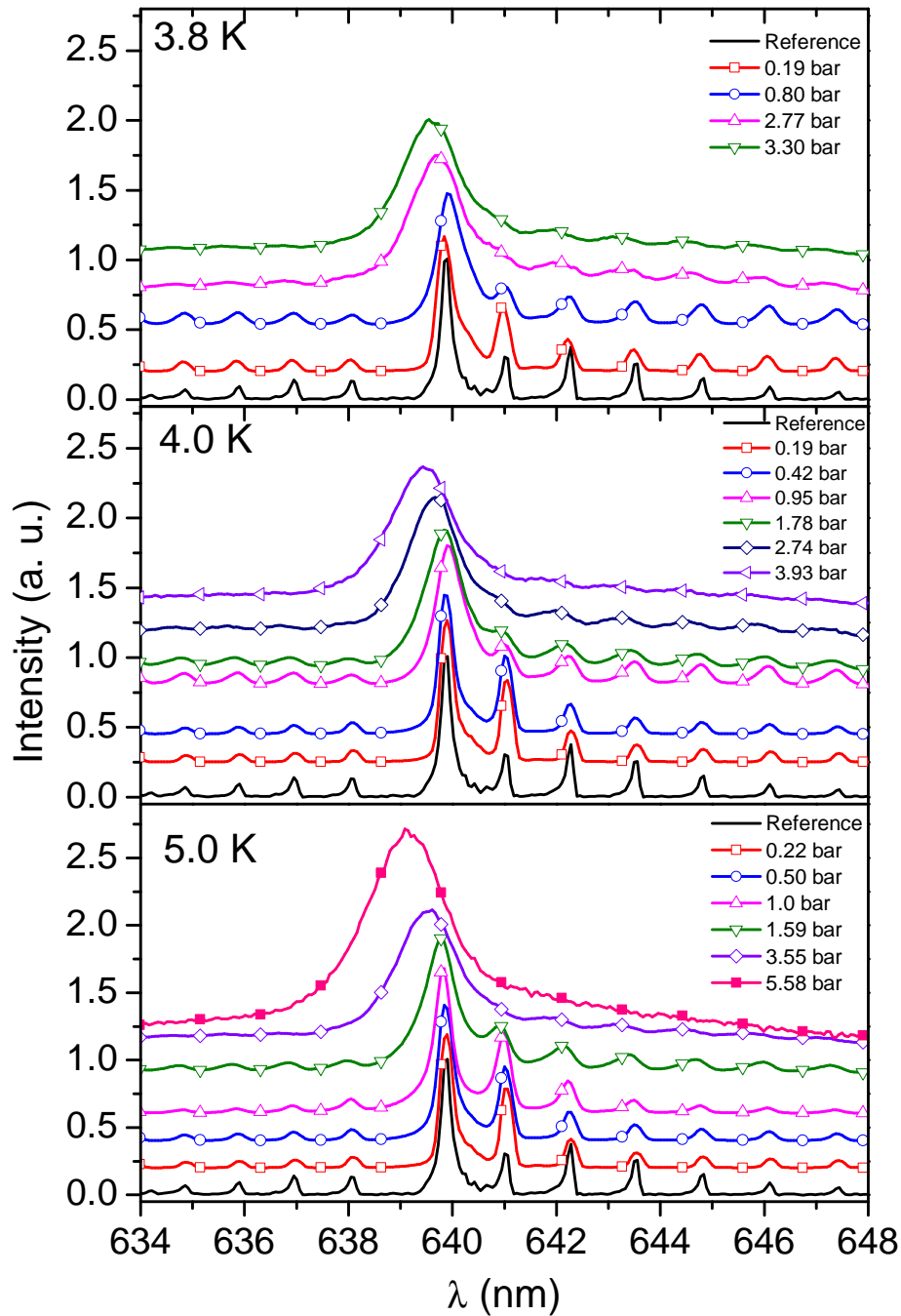


Figure 4.10: Development of the $d^3\Sigma_u^+ \rightarrow b^3\Pi_g$ (0-0) transition as a function of pressure for the 3.8, 4 K and 5 K isotherms. The spectra have been scaled and shifted for visualization purposes (scaling and shift factors detailed in Table 4.3). The P(2) line at 641 nm can be seen to merge with the Q-branch as pressure increases (see text and Fig. 4.11). Rotational lines broaden and resolution vanishes progressively with pressure. Every 20th data point was displayed with a symbol for clarity. The reference spectrum corresponds to a glow discharge spectrum similar to the one in Fig. 4.3, but this time recorded on the 3-June-2014.

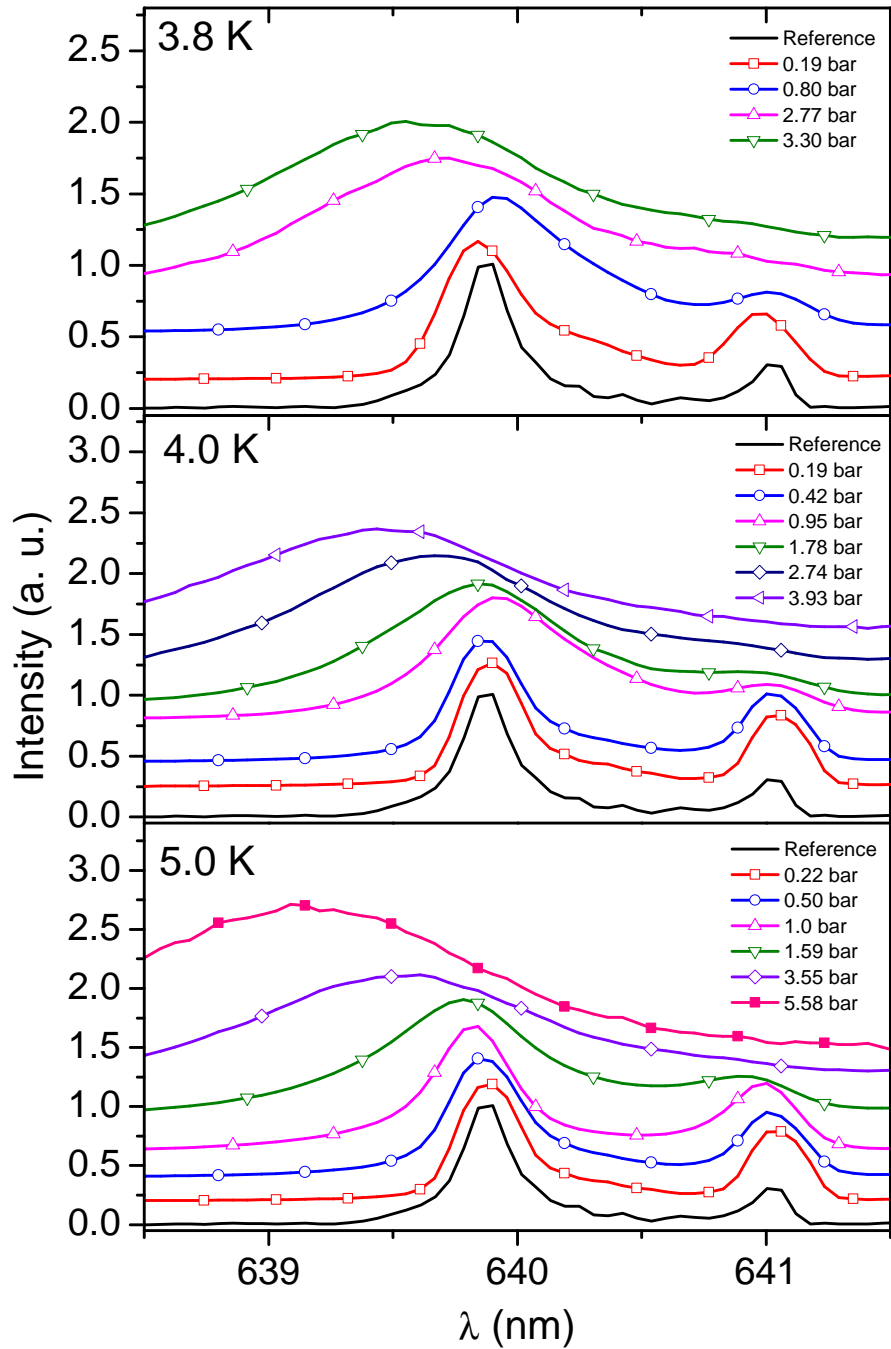


Figure 4.11: Zoom-in of the Q-branch and P(2) of Fig. 4.10. The spectra have been scaled and shifted for visualization purposes (scaling and shift factors detailed in Table 4.3). The P(2) line merges completely with the Q-branch as pressure increases. Also, the lineshapes evolve from a symmetric to an asymmetric profile as a function of pressure. See text. A different number of data points between 5 and 9 on each spectrum have been skipped for clarity (different numbers were chosen to prevent points from bunching together). The reference spectrum corresponds to a glow discharge spectrum similar to the one in Fig. 4.3, but this time recorded on the 3-June-2014.

The line broadening of the lines will be investigated more closely in Section 4.7.

- Spectral features experience a redshift and then a blueshift as a function of pressure with respect to the glow discharge spectrum. This will be looked at more into detail in Section 4.8.
- The R-branch loses rotational resolution at much earlier pressures than the P-branch.
- The features discussed in the preceding bullet points are shared between Figs. 4.7 and 4.10. The only significant difference is that in the supercritical phase it was possible to measure higher pressures than in the liquid phase (up to 6.80 bar at 16 K). At such high pressures, the disappearance of rotational resolution is evident. In spite of the similarities of the phenomena observed in both phases, it is hypothesized that the physics occurring at subcritical temperatures is substantially different than for other phases, as will be seen in Sections 4.7 and 4.8: rotational lines broaden and shift with pressure in a way that cannot be attributed to classical gas-phase pressure broadening alone but rather to a combination of classical pressure broadening and a cage effect due to clustering.
- Upon comparison of spectra in the subcritical and gaseous phases (Figs. 4.10 and 4.5), it was found that the rotational resolution in the liquid phase vanishes at much earlier pressures than in the gas-phase. Also, the resolution of the R-branch seems to be lost at the same time than the P-branch, contrary to what happens in the liquid phase (compare 14 bar at 80 K and 2.77 bar at 3.8 K). The first four features stated in this list for the liquid phase are present also at 80 K.
- Fig. 4.10 can be related to published results by other authors:
 - In luminescence spectroscopy studies of liquid and cold gaseous helium excited by an electron beam, Dennis and coworkers found that the transition under study bore no rotational resolution in the liquid phase. See Fig. 1.7. This is not in agreement with the observation in Fig. 4.10. However, in both cases, it is possible to observe red and blue shifts of the spectral features with respect to the reference values.
 - In helium droplets excited with synchrotron radiation it was found that the luminescence spectrum of helium droplets bears an isotopic as well as a size dependence. In particular, the spectrum of a large ^4He droplet

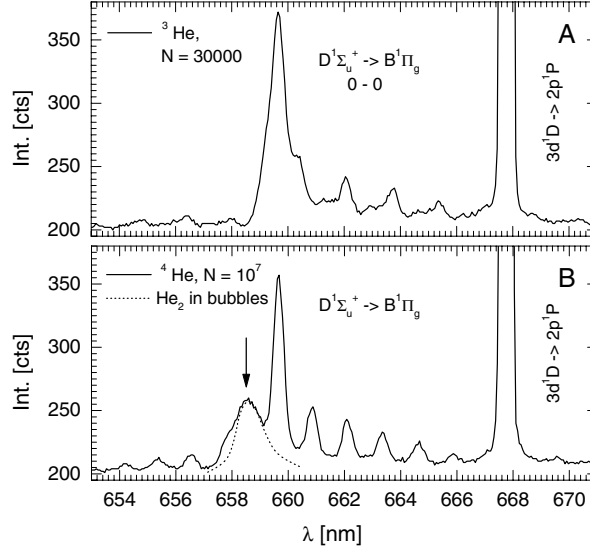


Figure 4.12: $D^1\Sigma_u^+ \rightarrow B^1\Pi_g$ (0-0) transition observed in the luminescence spectrum of ^3He (top panel) and ^4He (bottom panel) droplets. Sizes indicated. The spectrum in panel B can be interpreted as the superposition of excimer emission inside bubbles in the droplet (sharp lines) and emission from molecules desorbed from the bubble (broad feature marked by arrow). Reproduced from Fig. 2 of [110].

(10^7 atoms) exhibits a broad feature that resembles the spectrum of bulk liquid helium (see Fig. 4.12); it was interpreted as the emission from a bubble within a large ^4He droplet. Emission observed at large pressures in Fig. 4.10 bears resemblances to said emission from a bubble. However, the shift observed in this work is not as large as the shift in [110].

- Sharp rotational lines in the corona discharge emission of the $d^3\Sigma_u^+ \rightarrow b^3\Pi_g$ (0-0) transition have been observed at 4.2 K and 1.0 bar (see Fig. 1.9). A blueshift for increasingly large pressures was observed in that work for the $3^3S \rightarrow 2^3P$ (706.1 nm) line, but no such study was carried out for the molecular transition under study here.

4.7 Linewidth versus pressure

To investigate the physical origin of our observations, the linewidth of the P- and Q-lines of the transition of interest was analyzed as a function of pressure and temperature. This analysis was challenging because of the limited resolution of the spectrometer (0.1 nm), changes in the line shape (that is, the transition from a symmetric into an asymmetric line shape) and the uncertainty inherent to fits at large pressures, where rotational resolution is (almost) lost and the definition of each line becomes ambiguous.

By fitting lorentzians to selected atomic transitions in the calibration standard

(the glow discharge, which was recorded at vanishing pressures) an average linewidth of 0.20 nm was found. This linewidth is interpreted as the system's response function (in this context system means the whole optical setup, in this case dominated by the slit width). The deconvoluted linewidth is, then, the linewidth of any given line minus the linewidth of the system's response function.

For the $d^3\Sigma_u^+ \rightarrow b^3\Pi_g$ (0-0) transition the rotational lines P(4) and P(6) have been found to be the most suitable for analysis: P(2) merges relatively early with Q-branch and P(8) and P(10) are sometimes too distorted to provide a reasonable measure of the line broadening.

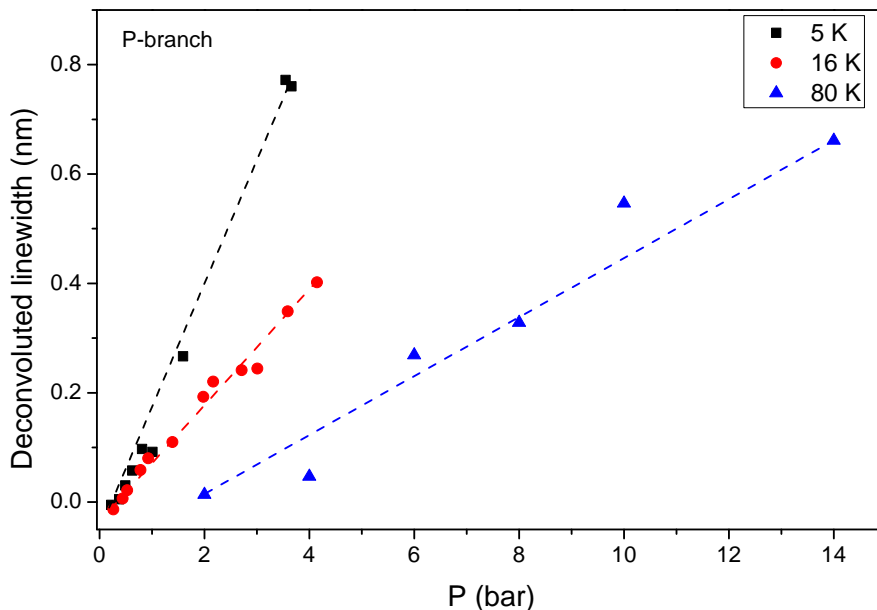


Figure 4.13: Linewidth of the P- rotational lines for isotherms in different phases of helium. This value corresponds to the mean of the linewidths of P(4) and P(6). Trend-lines added for convenience.

Fig. 4.13 shows a comparison of the line broadening of the P-lines in different thermodynamic states; it also shows that the sub/supercritical phases exhibit a much stronger dependence of the linewidth on pressure than the gaseous phase. This observation suggests that the measured line broadening cannot be explained on classical pressure-broadening of single excimer molecules in a dense gas alone (a density effect); this is easily proved in Fig. 4.14, by investigating the linewidth as a function of the mass density; it shows that different isotherms at any given density exhibit different line broadenings thus demonstrating that pressure-broadening is not the only mechanism contributing towards line broadening.

Fig. 4.15 shows the deconvoluted linewidth vs. P for selected isotherms in the subcritical phase of helium. In the pressure range where helium is liquid, the slopes of the trend-lines for the three different isotherms do not differ appreciably and so

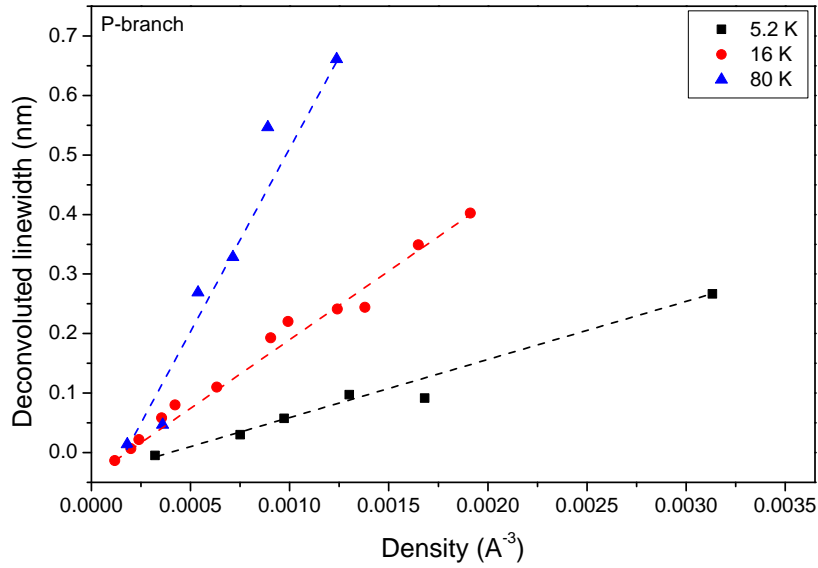


Figure 4.14: Linewidth of the P- rotational lines for 5.2, 16 and 80 K isotherms as a function of the number density. The 5.2 K isotherm is made up of data from the 5.0 K isotherm and the taking the temperature of the plasma as 5.2 K is a working hypothesis. Only points concerning the vapor phase of the 5 K isotherm are considered because after crossing the phase boundary, the density of the species is fairly inhomogeneous since in the immediate neighborhood of the excimer there is empty space (the bubble) and thereafter, the solvation shells of the bubble.

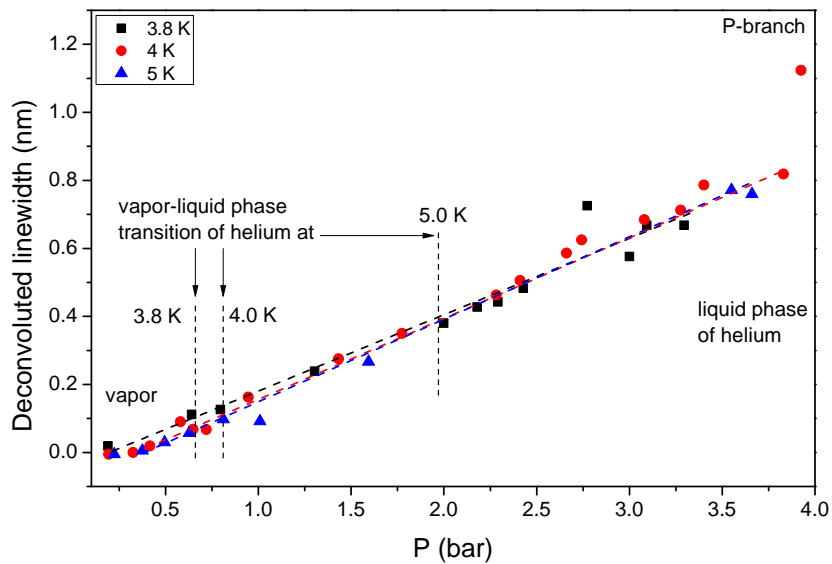


Figure 4.15: Linewidth of the P- rotational lines for selected isotherms below the critical point of helium. The linewidth shown is the mean of the linewidths of P(4) and P(6). Trend-lines fashioned as dotted lines were added as a guide to the eye. For pressures greater than 2.5 bar the linewidth is increasingly more difficult to measure because the rotational resolution progressively vanishes and the lines also change their shape. Saturated vapor pressures are indicated with vertical dotted lines for the temperatures indicated in the Figure.

one is led to conclude that the same broadening mechanism (apart from pressure broadening) is acting at this scale.

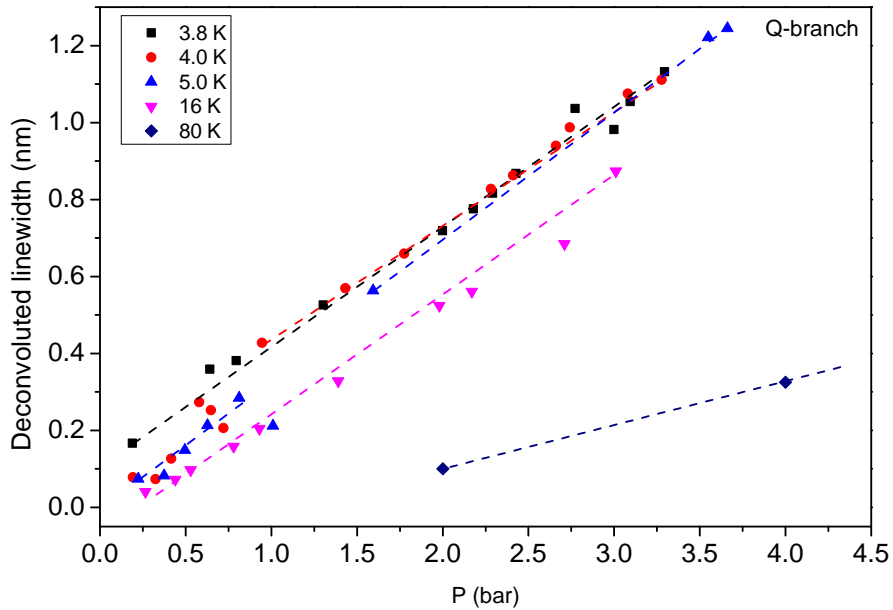


Figure 4.16: Linewidth of the Q-branch for isotherms in various thermodynamic states of helium as a function of pressure.

The linewidth of the Q-branch of the transition of interest has been investigated too. This is valid even though the Q-branch is the superposition of many different lines. The measured linewidth in this way is close to the expected width of a single Q-line because the separation between them is small. Fig. 4.16 shows the deconvoluted linewidth as a function of pressure for the same isotherms as in Figs. 4.13 and 4.15. The points follow linear trends but unfortunately gaps are left where a phase transition is expected to occur; more data points are required in order to investigate the hypothesized phase boundary. Isotherms in the sub/supercritical regimes exhibit a similar dependence on pressure, reflected on them having similar slopes.

Linewidths of P- and Q-lines are compared in Fig. 4.17 for a temperature bracket ranging between 3.8 K and 80 K. The slopes of the trend-lines of the P-lines are very similar so to avoid cluttering only one of them is chosen and compared against the Q- lines.

4.8 Line-shift versus pressure

This Section contains the line-shift analysis performed on isotherms pertaining to the phases of helium described above. The lineshift analysis is the measurement of the lineshift of the P- and Q-branches of the transition (with respect to the calibration

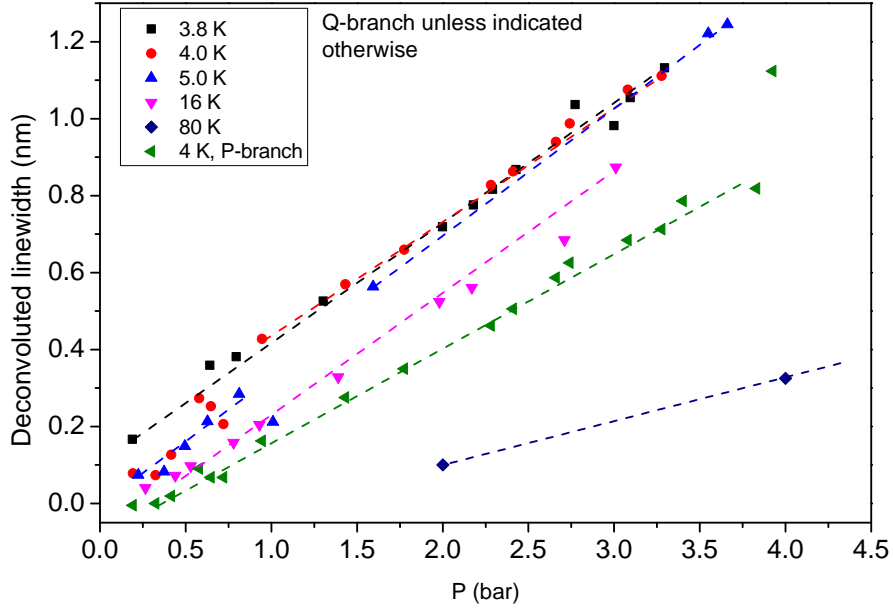


Figure 4.17: Comparison of the line broadening of P- and Q- rotational lines for 3.8, 4, 5, 16 and 80 K for Q- and P-branches. In order to avoid cluttering, only one isotherm representing P-branch is shown.

standard) as a function of pressure and temperature. In the case of the P-branch, the reported value corresponds to the average of the shift of the P-rotational lines. P(2) was excluded from this analysis because it strongly overlaps with the Q-branch.

In concrete, the lineshift is measured as the reference value (from the calibration standard) minus the measured peak position of a given rotational line. Hence, a positive line-shift denotes a change towards shorter wavelengths and is thus interpreted as blue-shift; negative shifts are interpreted as red-shifts. Caution is in order for larger pressures as the accuracy of the fits decreases with pressure due to broadening.

Fig. 4.18 compares the lineshift of the rotational lines (measured via the Q-branch criterion) of representative isotherms in the different phases of helium. It is apparent that there exist quasi-linear regions in the $\Delta\lambda$ vs. P dependence for the isotherms. There is a suggestion of a plateau at 80K when $P < 6$ K that may warrant further investigation but in the context of the present work is of minor importance. The Figure also shows that the slope of the linear region of the $\Delta\lambda$ vs. P is temperature-dependent. There is a stark contrast in the slopes of the sub/supercritical and the gas phases: the slope of both sub/supercritical phases is much larger than that of the gas; hence, the latter phase can be thought of as a classical, pressure broadening-dominated region, whereas the former can be interpreted as a structure-related regime, dominated by the formation of clusters.

Fig. 4.19 displays $\Delta\lambda$ vs. pressure for isotherms in the 3.8 K - 5 K temperature

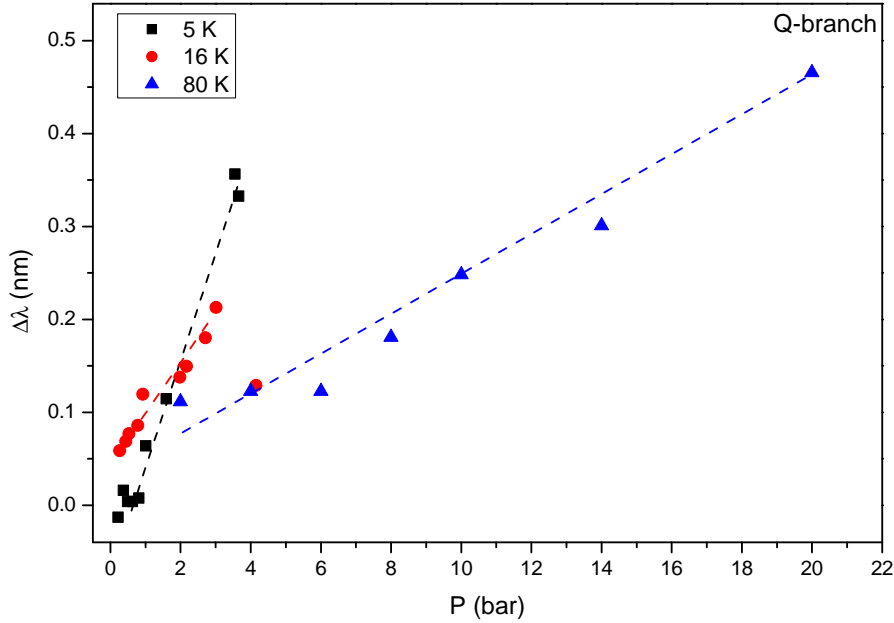


Figure 4.18: Line-shift of the Q-branch for isotherms in the 5 K- 80 K temperature bracket as a function of pressure. Dashed trend-lines are added for convenience.

bracket (subcritical phase) for Q- and P-branch transitions.

For the Q-branch, a red-shift is observed in the 3.8 K and 4 K isotherms; it is absent in the 5 K isotherm. After the minimum/plateau region an almost linear blue-shift with pressure for the coldest isotherms is observed, whereas for 5 K a plateau is followed by a steady linear blue-shift. The red-shift can be interpreted as the signature of a structural change (phase transition close to the phase transition from vapor to liquid helium), namely the growth of a cluster surrounding the excimer. The steeper linear regime is interpreted as excimers surrounded by a solvation shell of denser helium embedded in liquid helium (see Fig. 2.9).

The line-shift has also been measured using the P-lines of the transition (see the bottom panel of Fig. 4.19). In practice this corresponds to the average of the lineshifts of P(4)-P(10). For the 4 and 5 K isotherms a slight redshift is observed; however, such redshift is within the error and as such is attributed to a systematic error in the fitting (lineshift should be negligible for vanishing pressures). In the 4 K isotherm two regions with different slopes are apparent: one of them at low pressures is identified with a gaseous-like environment for the excimer and the other one at larger pressures is representative of the solvated state; such change in slopes cannot be identified for the isotherms at 3.8 and 5 K due to the lack of the necessary data points to make that claim: the former contains mainly points in the solvated phase and the latter consists mostly of points in the gaseous phase.

The evidence presented in this Section indicates a change of structure of the light emitters and it prompts us to postulate the existence of a phase transition

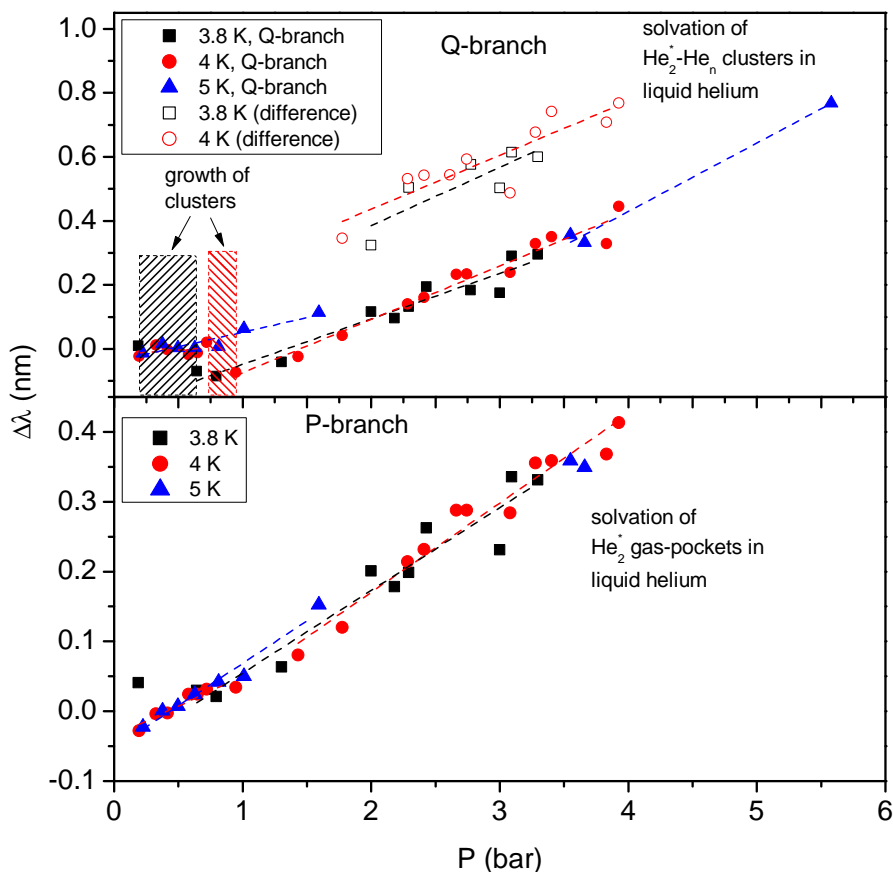


Figure 4.19: Line-shift of the Q-branch (top panel) and P-lines (bottom panel) for isotherms in the 3.8 K- 5 K interval as a function of pressure. The different regions in this diagram have been interpreted in terms of growth and solvation of clusters as indicated. In general, in each isotherm two qualitatively different thermodynamic regions have been identified: a region in which excimers exist in a gaseous-like phase (the gas pockets) and a region where the excimers are solvated (identified by a stronger interaction with the environment or, in other words, a larger slope). Linear fits have been added in dashed lines; results of the fits are shown in Table 4.8. The ‘difference’ spectrum in the top panel will be explained in Section 4.10.3. Extrapolation of the trends to vanishing pressures produces (negative) lineshifts for the P-branch that are within the resolution of the setup and are thus ignored.

for the excimer-helium mixed system. This phase change consists in the emitters (either excimers or excited atoms) being trapped (or ‘caged’) into an empty space in a cluster of helium atoms. An estimation of the loci where said phase transition occurs is given in Fig. 4.20. The phase transition is expected to occur at slightly lower pressures than the SVP curve of ^4He , but unlike it, it would not end at the critical point but would rather extend beyond.

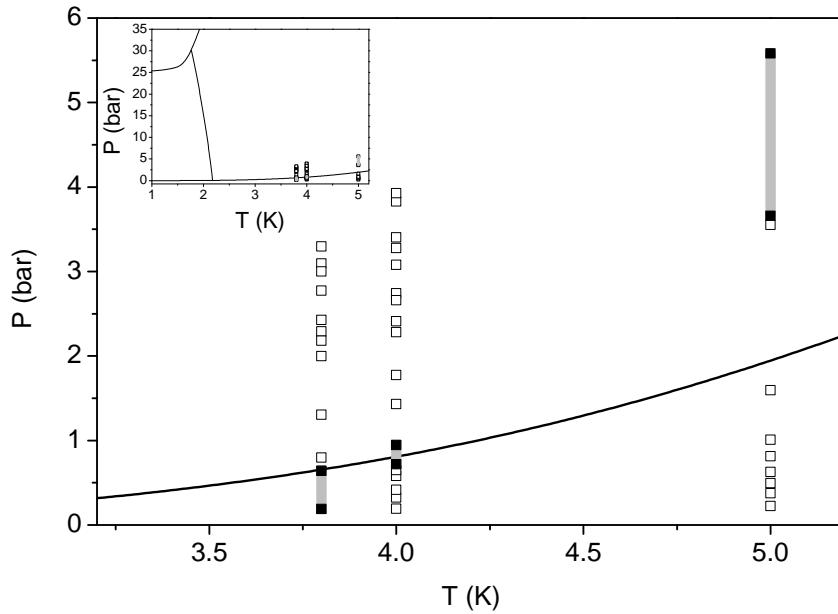


Figure 4.20: Hypothesized phase diagram for the excimer-helium mixed system. The shaded region between the filled points represents the region in the P-T diagram where the hypothesized thermodynamic transition for the excimer-helium mixed system is located; both hollow and filled points represent spectra measured for each of the indicated isotherms. The SVP curve of ^4He (solid line) was added for comparison. The inset shows the whole phase diagram of ^4He .

For small pressures below the phase transition, gas-phase behavior is expected because of the possibility of local heating. This is expected in the immediate vicinity of the tip, where a high Joule power dissipation is likely to occur thus increasing the temperature; on the other hand, at high pressures the presence of additional helium atoms would force the clusters to boil rather than increase their temperature.

4.9 Error determination in this experiment

The error associated with the determination of lineshifts and linewidths can be traced to different sources, namely: the error inherent to the mathematical fitting procedure, the asymmetry of the lines, fluctuations in the discharge current,

T (K)	Line	Phase	Parameter	Value	Standard error	Relative error (%)
3.8	Q	s	Intercept	-0.19	0.03	14.9
			Slope	0.14	0.01	8.5
4	Q	g	Intercept	-0.02	0.02	114.4
			Slope	0.03	0.04	136.1
4	Q	s	Intercept	-0.24	0.03	11.9
			Slope	0.17	0.01	6.2
5	Q	g	Intercept	-0.04	0.01	35.0
			Slope	0.09	0.02	17.4
5	Q	s	Intercept	-0.43	0.09	21.3
			Slope	0.21	0.02	9.7
3.8	Q	d	Intercept	0.02	0.16	715.9
			Slope	0.18	0.06	31.0
4	Q	d	Intercept	0.10	0.09	90.5
			Slope	0.17	0.03	17.8
3.8	P	s	Intercept	-0.06	0.03	41.5
			Slope	0.12	0.01	9.8
4	P	g	Intercept	-0.04	0.01	23.7
			Slope	0.09	0.01	16.4
4	P	s	Intercept	-0.09	0.03	31.6
			Slope	0.13	0.01	7.3
5	P	g	Intercept	-0.05	0.01	16.0
			Slope	0.12	0.01	8.1

Table 4.4: Intercepts and slopes of the linear fits in Fig. 4.19. The phases referred to in the Table are gaseous (g), solvated (s) and d represents the difference spectrum for 3.8 K (as per Section 4.10.3); in a ‘solvated’ spectrum, the lineshift featured is dominated by the solvated state of the excimer, whereas a ‘difference’ spectrum contains purely solvated features. The relative error is the absolute error divided by the value of the magnitude (slope or intercept). Slopes in nm/bar and intercepts in nm.

changes in temperature and pressure for the duration of the spectra acquisition⁵ and the broadening of the spectral lines as a function of pressure and their concomitant overlap. Error attributable to counting (Poisson error) is negligible in this experiment because the number of counts per accumulation is in the order of hundreds (or higher); each spectrum is formed of 5-20 accumulations.

Across the different isotherms studied and especially for low pressures, the errors provided by the fitting routines are exceedingly small (about 5% or less), visually almost as prominent as the symbols used to represent the data points in Figs. 4.13-4.19. We will see below that the error provided by a fitting routine does not account for the whole error associated with the measurement.

Errorwise, linewidths and shifts are very different since the fitting of line positions (and consequently the determination of lineshifts) is inherently more precise. The error is dominated by the scattering of the lineshifts and linewidths; this means that the scattering of the shifts and widths due to changing temperatures and pressures is greater than the estimated variations in said magnitudes due to the other sources of error cited at the start of this Section.

The results of this work have been summarized in Figs. 4.13-4.19 and it has been found that the linewidths and (mainly) the lineshifts follow linear patterns or progressions. This naturally leads to the problem of fitting straight lines, whose solution is well known in the literature [14]. An indirect measure of the error would be naturally given by the goodness of the linear fit, quantified by the R^2 factor. For the lineshift fits said factor ranges between 0.84 and 0.96 (the closer to 1, the better the linear fit). This is evidence that the linear fit is a fair model for the results we have obtained. It can also be interpreted as an estimation of the error in this experiment.

4.10 Structural model and discussion

It has been argued that pressure broadening is not the only mechanism at play to account for the physics of the rotational line emission. The picture based on the formation of a bubble and a cluster around the bubble (Cf. Fig. 2.9) to explain the observed features is elaborated upon in this Section.

4.10.1 Formation of clusters

In the previous Section it has been observed that the Q-branch features a slight red-shift and then a blue-shift as a function of pressure for certain isotherms at low

⁵ The temperature variation during a spectrum acquisition is of about 0.2 K for the lowest temperatures (3.5 and 4.0 K) and becomes less than 0.05 K at the largest temperatures (16 K). Changes in the temperature of the cell are followed by changes in the pressure of the helium.

temperatures; see Fig. 4.19. A discontinuity has been observed for the isotherms at 3.8 K and 4 K. The redshift in Fig. 4.19 indicates a structural change and is interpreted as a signature of condensation into clusters and the aforementioned discontinuity as the region of growth of clusters. The hypothesized physical picture is that for isotherms below the critical temperature of ^4He at low pressures, excimers flow freely in the vapor phase and, at pressures slightly below the SVP curve of helium, join ground state He atoms forming a void space around the excimer similar to liquid helium; this suggests the existence of an analogue of the SVP curve of ^4He for condensation of excimers into clusters (see Fig. 4.20). Upon further increase of the pressure the solvation shell around the bubble is completed. Upon even further increase the bubble undergoes compression and the excimer is increasingly more influenced by the neighboring helium atoms until the rotation of the excimer is completely hindered; it is then that rotational lines get completely smeared out.

For the same model to hold in supercritical helium, the “condensation-SVP” curve should extend beyond the critical point of ^4He . In this way, the higher the temperature (for example 16 K), the higher the pressure required to establish (or “condense”) a void around the excimer. Consequently, the transition to the “condensed” phase would be obtained at considerably much larger pressures. At such large pressures signatures of condensation (like a red-shift of the spectral lines) would probably be overshadowed by other effects (mainly pressure broadening).

4.10.2 Linewidth and lineshift revisited

Depending on the phase, linewidths are taken as signatures of pressure broadening or caging. In the case of caging, broadening can arise due to asymmetries in the interparticle potential, whereas lineshifts are interpreted as signs of changes in the electronic levels of excimers due to interaction with the environment.

The investigation of the linewidth as a function of pressure has shown that in the sub/supercritical phases of helium there are line-broadening phenomena that cannot be explained on the basis of density effects (pressure broadening) alone.

The study of the lineshift of the spectral lines produced further indication of cluster-formation, specifically features overlapping with the Q-branch; trends observed for sub/supercritical phases were completely different than for gaseous (80 K) helium. Isotherms at 3.8 and 4.0 K showed a redshift for features overlapping with the Q-branch in a PT region consistent with the notion that a phase transition occurs at pressures lower than the SVP curve of ^4He .

However, the P-line positions should show a similar trend to the Q-branch, but they do not. Our observations can be summarized as follows:

- P- and Q-features exhibit different lineshifts.

- Q-branch features an asymmetric line-shape.
- Q-branch is broader than P- and R-lines.

The above facts are interpreted as two-spectra being superimposed. In this framework, the P-, Q- and R-lines observed in free molecules are consistent with our observations; however, for caged excimers only features centered around the Q-branch would be observed (this is essentially a rotationally-collapsed spectrum in line with the observations in pure ^3He droplets [94]). The present model is based on the idea of two kinds of emitters: excimers surviving within gaseous helium pockets within the liquid helium and, on the other hand, excimers living in bubbles embedded in liquid helium; the archetype of the former is the sharp spectra we have observed in the gaseous phase of helium, and the archetype of the latter is the broad, unresolved spectrum observed by Dennis and coworkers. Both kinds of emitters emit a characteristic kind of spectrum and the total spectrum is the linear superposition of the two different contributions. If we were able to model the contribution from excimers in gas pockets then we would also be in position to indirectly model the contribution of the excimers in liquid helium and also we would be able to estimate the relative contribution of emitters in different thermodynamic states.

To explain our observations we consider regions in the cell of different temperatures. A temperature gradient is not unreasonable to expect because of the possibility of local heating in the vicinity of the tip and thus the formation of gas pockets within the liquid helium.

In the context of this experiment, the discrepancy in the outcome of the P- and Q-lines' shift vs. P could be interpreted as evidence supporting the existence of emitters embedded in different environments; since the observed spectrum is the linear superposition of all the contributions it becomes a formidable task to disentangle the contributions of different emitters; this is attempted in the next Subsection.

4.10.3 Simulation of the different contributions to the spectra

In this Subsection we have attempted to disentangle the different contributions made to the spectrum of the $d^3\Sigma_u^+ \rightarrow b^3\Pi_g$ (0-0) transition by the different emitters in the cryogenic cell. For that purpose we have utilized a program written on the Mathematica computing platform by Dr Nelly Bonifaci (CNRS, Grenoble). The source code has been reproduced with permission from its author in Appendix F.

The program used to simulate the transition in the gas phase works on the basis of the vibrating rotor model described above. Lineshifts, linewidth of the lines and

the rotational parameters can be changed by the user and after several trials we have used the values prescribed by [63] except for the rotational constants of the involved states. The values we have used are (with units being cm^{-1} except for T_{rot}):

$$T_{eu} = 164479 \quad (4.1)$$

$$\Omega_{eu} = 1728.01 \quad (4.2)$$

$$\Omega ex_{eu} = 36.13 \quad (4.3)$$

$$B_{eu} = 7.341 \quad (4.4)$$

$$\alpha_{eu} = \frac{224}{10^3} \quad (4.5)$$

$$T_{el} = 148835; \quad (4.6)$$

$$\Omega_{el} = 1769.07 \quad (4.7)$$

$$\Omega ex_{el} = 35.02 \quad (4.8)$$

$$B_{el} = 7.417 \quad (4.9)$$

$$\alpha_{el} = \frac{220}{10^3} \quad (4.10)$$

$$T_{\text{rot}} = 750 \text{ K}. \quad (4.11)$$

The notation utilized above is the same as in the source code. The subscripts “*u*” and “*l*” stand for “upper” and “lower”, respectively⁶. Therefore, and for the sake of the example, T_{eu} means T_e (with the meaning ascribed to this symbol in Chapter 2) for the upper state, and similarly for the other magnitudes.

The values of the Hönl-London factors from [70] have also been used in this simulation.

The idea behind the fitting procedure was to maximize the overlap of P- and R-lines pertaining to high J -quantum numbers between experimental and simulated spectra. The result of the fitting and subtraction process outlined above is shown in Fig. 4.21. It has also been found that the area subtended by the blue curve is about 20%. This could possibly be interpreted as the excimers in the liquid phase of helium contributing with said percentage to the total emission, at least in the channel represented by the transition of interest. It is important to emphasize that the rotational temperature of the simulation is 750 K, in stark contrast with the cryogenic environment of the experiment; this is a further confirmation that the excimer-generation process and light emission occur outside of thermodynamic equilibrium.

⁶The upper state is $d^3\Sigma_u^+$ and the lower state is $b^3\Pi_g$.

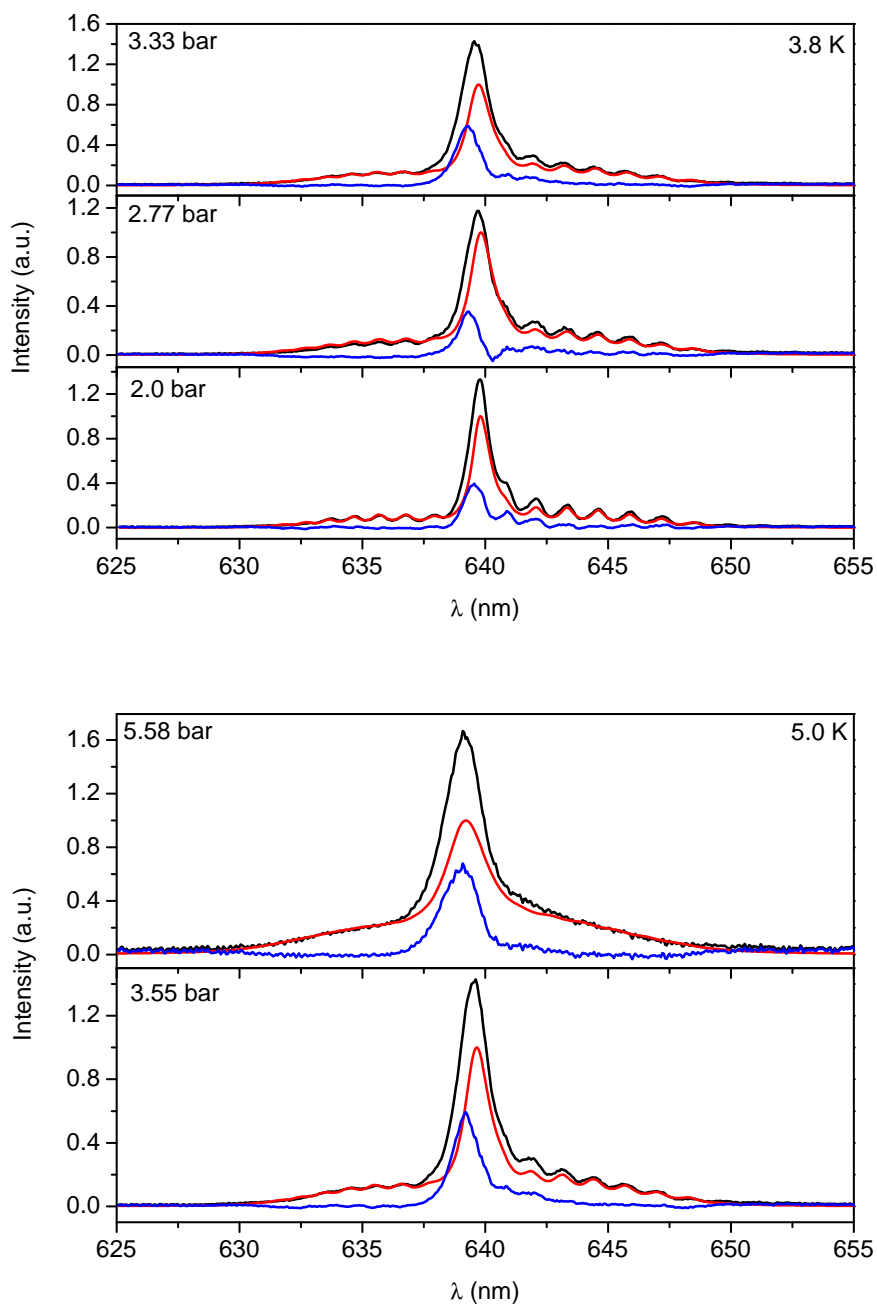


Figure 4.21: Results of the simulation of the transition of interest for representative temperatures and pressures. The black line in each panel represents the experimental data (normalized by a factor); the red curve represents the simulation (in this model, the contribution from excimers in gas pockets) and the blue curve represents the difference between each black and red curves (the contribution to the spectrum from excimers embedded in voids in liquid helium).

4.10.4 Distribution and localization of energy in a corona discharge in cryogenic helium

The total heating contribution of the electron-injecting tip (in negative polarity) is known, but the non-uniform distribution of energy and the dynamics of heat transport in the setup are not understood.

On an intuitive level it could be expected that the ionization zone of the discharge will be at a temperature higher than the rest of the helium. In this scenario, the existence of different environments that will affect differently the excimers in the liquid helium is viable, thus strengthening the idea of excimers subject to different thermodynamic conditions. A consequence of this is a potential local boiling of helium.

It has been observed that the rotational temperature of the excimers in gas pockets is distinctly different than that of the surrounding liquid helium environment which means that energy is strongly localized.

4.10.5 Rotational constants

By simulating the rotational spectrum it was found that rotational constants do not change under the thermodynamic conditions studied. This supports the assignment to free molecules because Grebenev's and Sartakov's work suggest that the excimer should respond to solvation with a change of the rotational constant.

The spectrum pertaining to the excimers in bubbles (in blue) does not show rotational features. Following Sartakov [94] it may be interpreted as a 'rotationally-collapsed' spectrum reflecting the caging/solvation of an excimer in condensed helium. The helium solvation shell is made of normal liquid and affects rotating molecules in a similar way to normal liquid ^3He in Sartakov's experiment. It has also been found that this spectrum corresponds to a rotational temperature no greater than 20 K.

Chapter 5

Conclusions and outlook

In this work we have utilized helium excimers to demonstrate single-molecule spectroscopy in liquid helium. We have also produced evidence of spectroscopic signatures for molecule emission within cavities in liquid helium.

Two effects were identified in the emission spectra: a cage effect, which is understood as the enclosure of an excimer molecule into a 7 Å-large void [29], and is characterized by a broad, rotationally-unresolved spectrum; on the other hand, a sharp spectrum, reminiscent of gas-phase emission. The former effect means that formation of excimer-He_n clusters and a concomitant hindered-rotation were observed; the latter indicates free rotation attributed to molecules in large gas bubbles of boiling helium.

There is a host of avenues that can be taken to further this research.

Collecting more data points in the region of the hypothesized phase transition for more isotherms is important for strengthening that finding. It would also allow us to study the phase transition of a mixed excimer-helium fluid in closer detail.

Equivalent experiments to the ones performed here with reversed (positive) polarity can be carried out to investigate the dynamics of clustering and free/hindered rotation of positive He snowballs in liquid helium.

With minor modifications to the equipment, mobility measurements of electrons in cavities and helium snowballs can be performed.

The efficiency of the light collection system is close to optimum so there is little point in modifying the optical layout. However, it is possible to exploit this fact to perform a cold emission experiment, which would consist of the same setup and experimental procedure; the only difference is to use voltages below the ignition of a full corona discharge. A minuscule current would circulate across the cell and the Joule heating impact of the discharge would diminish greatly, minimizing the requirement of higher cooling powers. The drawback is that longer exposure times (in the order of minutes or hours) would be required.

A more serious modification of the experiment involves increasing the cooling

power available; potentially this would mean using a different cryostat. The purpose of this change is twofold: on the one hand, an increase in the cooling power would allow us to study the superfluid transition, and on the other hand it would allow us to explore the empty regions at large pressures in the phase diagram (see Fig. 3.14) that were just barely accessible with our setup.

In the superfluid phase of ^4He free rotation is expected. However, following Grebenev's experiment, it would be possible to expect a non-superfluid layer developing around the excimer. This would mean a change in the rotational constant of the helium excimer. Also, by changing the superfluid to normal fluid ratio (in the 1.0 K- T_λ temperature bracket), a development of the spectrum similar to Grebenev's (see Fig. 1.5) is expected.

It is possible to probe the absorption transition $d^3\Sigma_u^+ \leftarrow a^3\Sigma_u^+$ using a two-photon excitation scheme (the two photon scheme ensures that the selection rules are maintained) [34]. This transition could be used to continue the study of hindered and free rotations in helium.

The results of this work challenge the current knowledge of the potential energy curve of the helium trimer $\text{He}_2^*\text{-He}$: it has been reported [29] that said potential energy curve does not exhibit a minimum; however, the findings of this work suggest that a minimum does actually exist. This calls for new calculations using more extended basis sets or a finer grid size.

Finally, the results of this experiments lead us to consider a reinterpretation of Dennis' experiment as follows: in his original work, it was stated that the temperature of the liquid helium irradiated with electrons was 1.7 K. It is possible that at this temperature the normal liquid concentration around the excimers was much larger than for OCS in ^4He clusters and ^3He - ^4He mixtures. The work by Sartakov, Grebenev, Toennies and Vilesov shows that the temperature has an effect on the linewidth and it is possible that at 1.7 K the linewidths are too large to be resolved. Apart from these fundamental reasons, it may be that the impinging electron beam heated locally the sample. It is then hypothesized that the temperature of Dennis' helium was too high to observe free-rotation, resulting in a loss of rotational resolution.

Appendices

Appendix A

Operation of the pumping station

The methodology for pumping described in this Section has been originally devised by Robert Limpenny and Dr Gauthier Torricelli.

Assuming that the pumping cart is initially disengaged from the fridge, the pumping station is operated as follows. Cf. Fig. 3.1.

To start up the pumping system:

- Before starting the operation of the pumping cart, ensure valves PV0, PV1, PV2, PV4 and PV6 are closed.
- Ensure oil level of the rotary pump is above minimum and clear, that is, no high levels of condensates (water) in oil which may affect performance/vacuum.
- Start the rotary pump. Wait at least 5 minutes before opening PV0.
- Open PV0 and PV1.
- Wait until reading on CH2 drops to 5×10^{-2} mbar or lower and then start the turbopump.
- Check CH2 and CH3 to ensure turbo functioning correctly and running normally, i.e. allow system to clean up.

To operate the roughing system:

- Check roughing line, close PV0 and open PV2.
- Check pressure of roughing line at CH1 ensuring pressure achieved is 5×10^{-2} mbar or less.
- During this roughing system check, ensure the turbo backing line pressure does not go above the critical backing pressure for the turbopump. If there is a concern, close PV2, wait several seconds, then open PV0 and drop the

pressure in the backing line of the turbopump. Once the pressures at CH2 and CH3 are at suitable levels, namely CH2 5×10^{-4} mbar and CH3 less than 5×10^{-4} mbar, it is then safe to resume the roughing line check process again.

To rough out OVC:

- Connect the pumping line to the refrigerator.
- Ensure turbopump pressures are 5×10^{-4} mbar on CH2 and less than 5×10^{-4} mbar on CH3.
- Close PV0, open PV2.
- Pressure at CH1 5×10^{-2} mbar or less, slowly open PV5 and rough out OVC to 5×10^{-2} mbar or less (ideally). While roughing out the OVC ensure turbopump pressures are maintained and adjust cart operation to maintain correct pressures as required.
- When the OVC is at 5×10^{-2} mbar or less, close PV2, open PV0, then open PV3 to continue to evacuate the OVC to below 10^{-2} mbar.

Appendix B

Operation of the Heliox AC-V refrigerator

The following methodology was used to cool down (symbols make reference to Fig. 3.1):

- Close V1 when $T < 240$ K. This is to use the ^3He as an exchange gas and accelerate the cooling.
- Set the SORB to 35-40 K. For safety, turn off all the heaters if the fridge is to run overnight.
- Look out for cryogenic pumping. If found, close PV5.
- Wait for the pot to cool down to 4 K.

The steps above describe the operation of the refrigerator down to 4 K. In order to cool down to 300 mK the operation is as follows:

- Open V1.
- Set HS to 18 K and let it on until SORB cools down below 10 K (usually 6-7 K).
- Close V1.
- Heat SORB to 35-40 K.
- Wait until it stabilizes (35 minutes or more).
- Open briefly V1. Opening V1 has a cooling effect.
- Set SORB to 0 and HS to 18 K.

Appendix C

Atomic and molecular transitions of helium

This is an inventory of notorious atomic and molecular transitions of He. Identification of the transitions taken from [40, 39, 38] and Table 4.7 of [108].

Transition	Wavelength or band-head (nm)	Reference
$e^3\Pi_g \rightarrow a^3\Sigma_u^+$ (0-0)	465.0	[108]
$d^3\Sigma_u^+ \rightarrow b^3\Pi_g$ (0-0)	640.1	[108, 40]
$D^1\Sigma_u^+ \rightarrow B^1\Pi_g$ (0-0)	659.6	[108, 39]
$f^3\Sigma_u^+ \rightarrow b^3\Pi_g$ (0-0)	596.0	[108, 40]
$C^1\Sigma_g^+ \rightarrow A^1\Sigma_u$ (0-0)	911	[38]
$C^1\Sigma_g^+ \rightarrow A^1\Sigma_u$ (1-1)	930	[38]
$C^1\Sigma_g^+ \rightarrow A^1\Sigma_u$ (2-2)	950	[38]
$c^3\Sigma_g^+ \rightarrow a^3\Sigma_u$ (0-0)	919	[38]
$3^1P \rightarrow 2^1S$	501.6	[108]
$3^1D \rightarrow 2^1P$	667.8	[108]
$3^1S \rightarrow 2^1P$	728.1	[108]
$3^3P \rightarrow 2^3S$	388.9	[108]
$3^3D \rightarrow 2^3P$	587.6	[108]
$3^3S \rightarrow 2^3P$	706.1	[108]
$4^1P \rightarrow 2^1S$	396.5	[108]
$4^1D \rightarrow 2^1P$	492.2	[108]
$4^1S \rightarrow 2^1P$	504.8	[108]
$4^3P \rightarrow 2^3S$	318.8	[108]
$4^3D \rightarrow 2^3P$	447.2	[108]
$4^3S \rightarrow 2^3P$	471.3	[108]

Table C.1: Transitions of He* and He₂*

Appendix D

Densities of liquid helium

Densities in \AA^{-3} for representative loci in the phase diagram of helium are provided in Fig. D.1. Notice the discontinuity in the values of density at the SVP curve. A representative value of the densities has been recorded in Table E.1 in Appendix E.

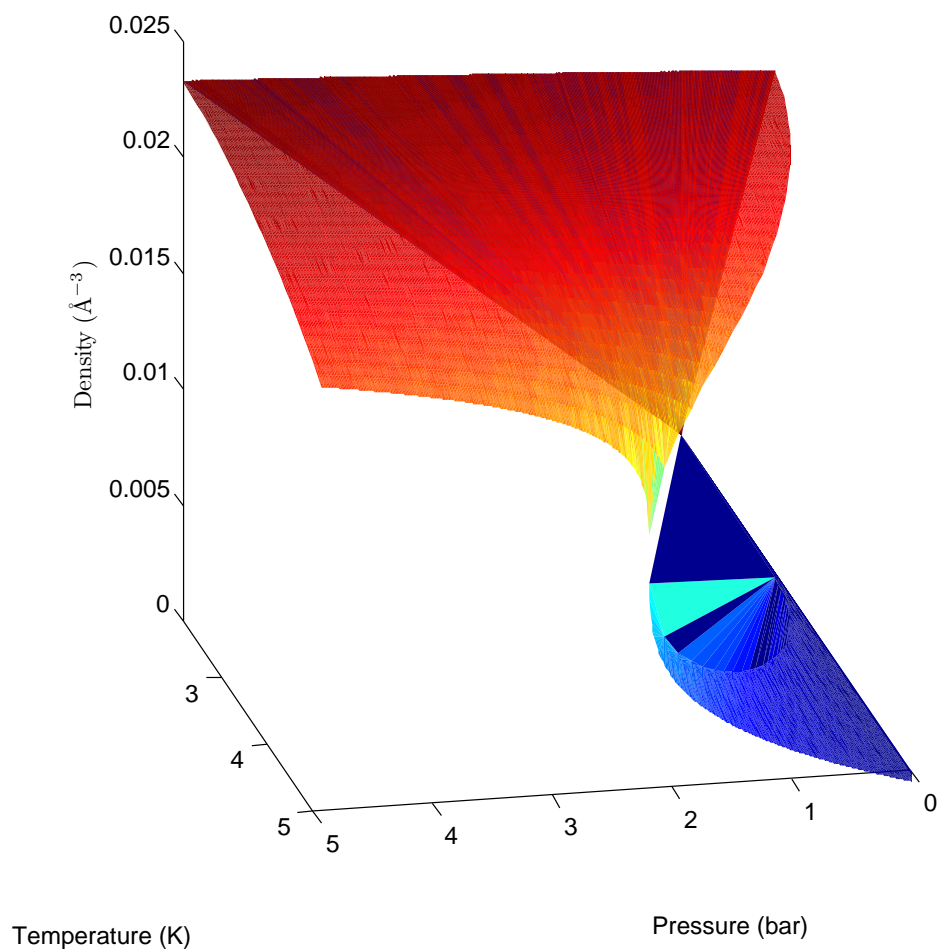


Figure D.1: Reported densities of helium in the normal liquid and vapor regimes. The data points used to generate this plot have been taken from [79].

Appendix E

Relevant physical constants and helium parameters

Property	Symbol	Value	Reference
Planck's constant	h	6.6256×10^{-34} Js	[5]
Boltzman's constant	k	1.38054×10^{-23} J/K	[5]
Universal gas constant	R	8.3143 J K ⁻¹ mol ⁻¹	[5]
Speed of light in vacuum	c	2.997925×10^8 m/s	[5]
Elementary electric charge	e	1.60210×10^{-19} C	[5]
Stefan-Boltzman's constant	σ	5.6697×10^{-8} W/m ² K ⁴	[5]
Rydberg constant	Ry or R_∞	1.0973731×10^7 m ⁻¹	[5]
Avogadro constant	N_A	6.022169×10^{23} mol ⁻¹	[5]
Bulk liquid ⁴ He density	ρ_{bulk}	0.0219 Å ⁻³	[51]
⁴ He critical temperature	T_c	5.2014 K	[85]
⁴ He critical pressure	P_c	2.2449 atm	[85]
³ He λ -temperature	T_λ	3×10^{-3} K	[13]
⁴ He λ -temperature	T_λ	2.1720 K	[85]
⁴ He atomic mass	$m_{^4\text{He}}$	4.00260 amu	[93]
³ He atomic mass	$m_{^3\text{He}}$	3.01603 amu	[93]

Table E.1: Physical constants utilized in this work and relevant parameters of He.

Appendix F

Shell-scripts and software

This Appendix provides the pieces of software used in this thesis for handling and analyzing data. Utilized computational platforms were diverse and include shell-scripting in UNIX/Linux and Mathematica running on Windows.

F.1 Script for normalization

The following script was used to normalize the spectra to the highest peak in the spectrum.

```
# Date: September 2014.
# Project: Cryogenic corona discharge.
# Programs and/or language(s) used: Linux shell-scripting and pyxplot.
# Handling of the headers: Ignored if preceded by a hash symbol (#).

# Description: This program normalizes the heighest peak in
# the spectrum (usually the 706 nm atomic line) to unity.

# How to use it: For using this script it load the data and the script
# itself onto some directory on the Snapper fileserver , which has
# pyxplot on it. Then, on the command line ,
# type 'chmod 755 script_filename' and
# run by typing './script_filename'.
# Follow the directions on the screen.
# The output files will then appear in the current directory.

clear

echo "Hi, this program will normalize your spectra contained in the
current directory"
echo "Please notice that this program will delete the files that
begin with the string calibrated_ since that is the format of
the output files produced by this script"
```

```

echo "First input the file extension of your datafiles (asc,
dat, txt, etc): "
read extension
echo "You have chosen extension $extension"
echo "Checking that files with the $extension extension
exist..."

rm uncalibrated_normalized_*. $extension

for file in ./*. $extension
do
    if [ -f "$file" ];
then
    echo "Files with the stated extension do exist. Carrying on..."
    break
else
    echo "No files with the aforementioned extension exist.
Please run the script again..."
    exit
fi
done

for i in *. $extension '
do
    pyxplot << EOF

filename='${i%.*}. $extension' # Data filename; it has to
# be in the current directory.

interpolate spline exp_spectrum() filename u 1:2
# Acquisition and interpolation of the experimental curve.

#Find the maximum and minimum values of x and y

N_data=0 # Initialization

foreach datum x,y in filename using 1:2
{

if N_data==0
{
    min_x_data=x
    max_x_data=x
    min_y_data=y
    max_y_data=y
}
}

```

```

if x<min_x_data
{
    min_x_data=x
}

if x>max_x_data
{
    max_x_data=x
}

if y<min_y_data
{
    min_y_data=y
}

if y>max_y_data
{
    max_y_data=y
}

N_data++

}

set output 'uncalibrated_normalized_${i%.*}.${extension}'
# Prepares the output datafile. It will be written into
# the current directory.
set samples 12081 # Number of data points in the results file.
tabulate [min_x_data:max_x_data]
(exp_spectrum(x)-min_y_data)/(max_y_data-min_y_data) u 1:2
# The script writes the normalized data onto the output file.

EOF

done

```

F.2 Script for recalibration

The following code for recalibration was produced by Dr Mark Watkins.

```

#!/bin/bash
unset FILEEXT
unset OFFSET
unset GRADIENT

#

```

```

# set the initial input variables for the calibration
#
until [ "${FILEEXT}" != "" ]; do
    echo "# Enter the file extension string you
    want to do the calibration for (i.e., without the dot):"
    read FILEEXT
done

until [ "${OFFSET}" != "" ]; do
    echo ""
    echo "# Enter the calibration y-intercept or constant offset:"
    read OFFSET
done

until [ "${GRADIENT}" != "" ]; do
    echo ""
    echo "# Enter the calibration gradient:"
    read GRADIENT
done

# do the recalibration

for i in $(ls *.$FILEEXT); do
    awk -v GRAD=${GRADIENT} -v OFF=${OFFSET}
    '{ printf "%-15s %s\n", OFF+(GRAD*NR), $2 > "tempfile"}' $i
    j='basename $i .$FILEEXT'
    mv tempfile ${j}-cal.$FILEEXT
done

unset FILEEXT
unset OFFSET
unset GRADIENT

exit 0

```

F.3 Simulation of the spectrum

The code below pertains to a Mathematica program developed by Dr Nelly Bonifaci to simulate theoretically the spectrum of the $d^3\Sigma_u^+ \rightarrow b^3\Pi_g$ (0-0) transition.

The program below was run using Mathematica 9.0.0.0 for Windows. Its input is an ascii-formatted file, two-columns containing the transition of interest. The rotational constants and other parameters as well as the linewidth of the different lines are input manually. The output of this program is a graph containing the original dataset (scaled by a carefully chosen factor), the fitted spectrum and the

subtraction of both. The program can be readily modified to export the three spectra into an ascii datafile to be treated with any other software.

```

SetDirectory["C:\\Users\\Luis\\data\\d-to-b_triplet_simulation"];
ClearAll[lambdaexp, Iexperimental, dim, donnée, I0, M, C1, C2, Ed, Eb,
BLF, BLF1, h, k, low, up, Flow, Fup, dis]
med = Import["experimental_data.dat"];
dim = Dimensions[med][[1]];
lambdaexp = Table[med[[i, 1]], {i, 1, dim}];
Iexperimental = Table[med[[i, 2]], {i, 1, dim}];
M0 = Max[Iexperimental];
donnée = Table[{lambdaexp[[i]], Iexperimental[[i]]}, {i, 1, dim}];
IE = Table[{lambdaexp[[i]], Iexperimental[[i]]/M0}, {i, 1, dim}];
Export["experiment.dat", IE, "Table"];
I0 = Interpolation[donnée];
C1 = ListPlot[donnée];
Teu = 164479; ωeu = 1728.01; ωexeu = 36.13; Beu = 7.341; αeu =  $\frac{224}{10^3}$ ;
Tel = 148835; ωel = 1769.07; ωexel = 35.02; Bel = 7.417; αel =  $\frac{220}{10^3}$ ;
GOu =  $\frac{\omega_{eu}}{2} - \frac{\omega ex_{eu}}{4}$ ;
GOl = 0.5ωel - (0 + 0.5)2ωexel;
labdaup = Teu + GOu;
labdalow = Tel + GOl;
Bou = Beu - 0.5αeu;
Bol = Bel - 0.5αel;
Deu =  $\frac{4B_{eu}^3}{\omega_{eu}^2}$ ;
Del =  $\frac{4B_{el}^3}{\omega_{el}^2}$ ;
βeu = Deu  $\left( -\frac{\alpha_{eu}^2 \omega_{eu}}{24B_{eu}^3} - \frac{5\alpha_{eu}}{B_{eu}} + \frac{8\omega ex_{eu}}{\omega_{eu}} \right)$ ;
βel = Del  $\left( -\frac{\alpha_{el}^2 \omega_{el}}{24B_{el}^3} - \frac{5\alpha_{el}}{B_{el}} + \frac{8\omega ex_{el}}{\omega_{el}} \right)$ ;
Dvu = Deu + (0 + 0.5)βeu;
Dvl = Del + (0 + 0.5)βel;
Ed = Table[(k + 1)k Bou + (k + 1)2k2 (-Dvu) + labdaup, {k, 1, 55}];

```

```

Eb = Table [(k + 1)k Bol + (k + 1)2k2 (-Dvl) + labdalow, {k, 1, 55}];
Array[Fup, {100, 100}, {0, 0}];
Array[Flow, {100, 100}, {0, 0}];
up = Table[Fup[i, j] = Ed[[i]], {i, 1, 51}, {j, 0, 50}];
low = Table[Flow[i, j] = Eb[[i]], {i, 1, 51}, {j, 0, 50}];
"P1: kup=1,3,5..., jup=2,4,6.....,klow=2,4,6..... jlow=3,5...";
FP1 = Table[Fup[2i - 1, 2i] - Flow[2i, 2i + 1], {i, 1, 20}];
λFP1 =  $\frac{10^7}{FP1}$ ;
Export["p1.dat", FP1];
Export ["lambdaP1.dat", λFP1];
"P2: kup=1,3,5..., jup=1,3,5.....,klow=2,4,6..... jlow=2,4,6...";
FP2 = Table[Fup[2i - 1, 2i - 1] - Flow[2i, 2i], {i, 1, 20}];
λFP2 =  $\frac{10^7}{FP2}$ ;
Export["p2.dat", FP2];
Export ["lambdaP2.dat", λFP2];
"P3: kup=1,3,5..., jup=0,2,4.....,klow=2,4,6..... jlow=1,3,5...";
FP3 = Table[Fup[2i - 1, 2i - 2] - Flow[2i, 2i - 1], {i, 1, 20}];
λFP3 =  $\frac{10^7}{FP3}$ ;
Export["p3.dat", FP3];
Export ["lambdaP3.dat", λFP3];
"Q1: kup=1,3,5..., jup=2,4,6.....,klow=1,3,5.... jlow=2,4,6...";
FQ1 = Table[Fup[2i - 1, 2i] - Flow[2i - 1, 2i], {i, 1, 20}];
λFQ1 =  $\frac{10^7}{FQ1}$ ;
Export["Q1.dat", FQ1];
Export ["lambdaQ1.dat", λFQ1];
"Q2: kup=1,3,5..., jup=1,3,5.....,klow=1,3,5... jlow=1,3,5...";
FQ2 = Table[Fup[2i - 1, 2i - 1] - Flow[2i - 1, 2i - 1], {i, 1, 20}];
λFQ2 =  $\frac{10^7}{FQ2}$ ;
Export["Q2.dat", FQ2];

```

Export ["lambdaQ2.dat", λ_{FQ2}];
 "Q3: kup=3,5..., jup=2,4,6.....,klow=3,5... jlow=2,4,6....";
 FQ3 = Table[Fup[2i + 1, 2i] - Flow[2i + 1, 2i], {i, 1, 20}];
 $\lambda_{FQ3} = \frac{10^7}{FQ3}$;
 Export["Q3.dat", FP2];
 Export ["lambdaQ3.dat", λ_{FQ3}];
 "R1: kup=3,5..., jup=4,6,8,10.....,klow=2,4,6... jlow=3,5....";
 FR1 = Table[Fup[2i + 1, 2i + 2] - Flow[2i, 2i + 1], {i, 1, 20}];
 $\lambda_{FR1} = \frac{10^7}{FR1}$;
 Export["R1.dat", FR1];
 Export ["lambdaR1.dat", λ_{FR1}];
 "R2: kup=3,5..., jup=3,5.....,klow=2,4,6... jlow=2,4,6....";
 FR2 = Table[Fup[2i + 1, 2i + 1] - Flow[2i, 2i], {i, 1, 20}];
 $\lambda_{FR2} = \frac{10^7}{FR2}$;
 Export["R2.dat", FR2];
 Export ["lambdaR2.dat", λ_{FR2}];
 "R3: kup=3,5..., jup=2,4.....,klow=2,4,6... jlow=1,3,5....";
 FR3 = Table[Fup[2i + 1, 2i] - Flow[2i, 2i - 1], {i, 1, 20}];
 $\lambda_{FR3} = \frac{10^7}{FR3}$;
 Export["R3.dat", FR3];
 Export ["lambdaR3.dat", λ_{FR3}];
 "QR12: kup=1,3,5..., jup=2,4,6.....,klow=1,3,5... jlow=1,3,5....";
 FQR12 = Table[Fup[2i - 1, 2i] - Flow[2i - 1, 2i - 1], {i, 1, 20}];
 $\lambda_{FQR12} = \frac{10^7}{FQR12}$;
 Export["QR12.dat", FQR12];
 Export ["lambdaQR12.dat", λ_{FQR12}];
 "QR23: kup=1,3,5..., jup=1,3,5....., klow=1,3,5... jlow=0,2,4....";
 FQR23 = Table[Fup[2i - 1, 2i - 1] - Flow[2i - 1, 2i - 2], {i, 1, 20}];
 $\lambda_{FQR23} = \frac{10^7}{FQR23}$;

Export["QR23.dat", FQR23];
 Export ["lambdaQR23.dat", λ_{FQR23}];
 "QP21: kup=1,3,5..., jup=1,3,5...,klow=1,3,5... jlow=2,4,6....";
 FQP21 = Table[Fup[2i - 1, 2i - 1] - Flow[2i - 1, 2i], {i, 1, 20}];
 $\lambda_{FQP21} = \frac{10^7}{FQP21}$;
 Export["QP21.dat", FQP21];
 Export ["lambdaQP21.dat", λ_{FQP21}];
 "QP32: kup=1,3,5..., jup=0,2,4...,klow=1,3,5... jlow=1,3,5....";
 FQP32 = Table[Fup[2i - 1, 2i - 2] - Flow[2i - 1, 2i - 1], {i, 1, 20}];
 $\lambda_{FQP32} = \frac{10^7}{FQP32}$;
 Export["QP32.dat", FQP32];
 Export ["lambdaQP32.dat", λ_{FQP32}];
 "PQ12: kup=1,3,5..., jup=2,4...,klow=2,4,6... jlow=2,4,6....";
 FPQ12 = Table[Fup[2i - 1, 2i] - Flow[2i, 2i], {i, 1, 20}];
 $\lambda_{FPQ12} = \frac{10^7}{FPQ12}$;
 Export["PQ12.dat", FPQ12];
 Export ["lambdaPQ12.dat", λ_{FPQ12}];
 "PR13: kup=1,3,5..., jup=2,4...,klow=2,4,6... jlow=2,4,6....";
 FPR13 = Table[Fup[2i - 1, 2i] - Flow[2i, 2i + 2], {i, 1, 20}];
 $\lambda_{FPR13} = \frac{10^7}{FPR13}$;
 Export["PR13.dat", FPR13];
 Export ["lambdaPR13.dat", λ_{FPR13}];
 "PQ23: kup=1,3,5..., jup=1,3,5,....,klow=2,4,6... jlow=1,3,5....";
 FPQ23 = Table[Fup[2i - 1, 2i - 1] - Flow[2i, 2i - 1], {i, 1, 20}];
 $\lambda_{FPQ23} = \frac{10^7}{FPQ23}$;
 Export["PQ23.dat", FPQ23];
 Export ["lambdaPQ23.dat", λ_{FPQ23}];
 "RQ21: kup=3,5..., jup=3,5,7...,klow=2,4,6... jlow=3,5,7....";
 FRQ21 = Table[Fup[2i + 1, 2i] - Flow[2i, 2i + 1], {i, 1, 20}];

$\lambda_{FRQ21} = \frac{10^7}{FRQ21}$;
 Export["RQ21.dat", FRQ21];
 Export ["lambdaRQ21.dat", λ_{FRQ21}];
 "RP31: kup=3,5..., jup=2,4,6...,klow=2,4,6... jlow=3,5,7....";
 FRP31 = Table[Fup[2i + 1, 2i] - Flow[2i, 2i + 1], {i, 1, 20}];
 $\lambda_{FRP31} = \frac{10^7}{FRP31}$;
 Export["RP31.dat", FRP31];
 Export ["lambdaRP31.dat", λ_{FRP31}];
 "RQ32: kup=3,5..., jup=2,4,6...,klow=2,4,6... jlow=2,4,6....";
 FRQ32 = Table[Fup[2i + 1, 2i] - Flow[2i, 2i], {i, 1, 20}];
 $\lambda_{FRQ32} = \frac{10^7}{FRQ32}$;
 Export["RQ32.dat", FRQ32]; Export ["lambdaRQ32.dat", λ_{FRQ32}];

"calculation of intensity for the general branch

with the Honl-London factor, i corresponds to

the lower level j";

SP1 = Table $\left[\frac{i(2i+1)}{6(2i-1)}, \{i, 3, 60, 2\} \right]$;
 SP2 = Table $\left[\frac{(i-1)(i+1)^2}{6.i^2}, \{i, 2, 60, 2\} \right]$;
 SP3 = Table $\left[\frac{(i+2)(2i-1)}{6.(2i+1)}, \{i, 1, 60, 2\} \right]$;
 SQ1 = Table $\left[\frac{(2i+1)(i-1)(i+1)}{6.i^2}, \{i, 2, 60, 2\} \right]$;
 SQ2 = Table $\left[\frac{(2i+1)(i^2+i-1)^2}{6.(i+1)^2.i^2}, \{i, 1, 60, 2\} \right]$;
 SQ3 = Table $\left[\frac{i(2i+1)(i+2)}{6.(i+1)^2}, \{i, 2, 60, 2\} \right]$;
 SR1 = Table $\left[\frac{(2i+3)(i-1)}{6.(2i+1)}, \{i, 3, 60, 2\} \right]$;
 SR2 = Table $\left[\frac{i^2(i+2)}{6.(i+1)^2}, \{i, 2, 60, 2\} \right]$;
 SR3 = Table $\left[\frac{(2i+1)(i+1)}{6.(2i+3)}, \{i, 1, 60, 2\} \right]$;
 SQR12 = Table $\left[\frac{2i+3}{6(i+1)^2}, \{i, 1, 60, 2\} \right]$;
 SQR23 = Table $\left[\frac{2i+1}{6.(i+1)^2}, \{i, 0, 60, 2\} \right]$;
 SQP21 = Table $\left[\frac{2i+1}{6.i^2}, \{i, 2, 60, 2\} \right]$;
 SQP32 = Table $\left[\frac{2i-1}{6.i^2}, \{i, 1, 60, 2\} \right]$;
 SPQ12 = Table $\left[\frac{i+1}{6.i^2}, \{i, 2, 60, 2\} \right]$;

SPQ23 = Table $\left[\frac{i+2}{6.(i+1)^2}, \{i, 1, 60, 2\} \right]$;
 SPR13 = Table $\left[\frac{i+2}{6.(i+1)^2(2i+3)(2i+1)}, \{i, 1, 60, 2\} \right]$;
 SRQ21 = Table $\left[\frac{i-1}{6.i^2}, \{i, 3, 60, 2\} \right]$;
 SRP31 = Table $\left[\frac{i-1}{6.i^2(2i+1)(2i-1)}, \{i, 3, 60, 2\} \right]$;
 SRQ32 = Table $\left[\frac{i}{6.(i+1)^2}, \{i, 2, 60, 2\} \right]$;
 “Boltzman distribution” ;
 $h = \frac{6.626}{10^{34}} ; c = 3 \cdot 10^{10} ; k = \frac{1.38}{10^{23}} ;$
 $\Delta\lambda = 1.95 ;$
 $De = 1.1 ; T = 750 ;$
 Array[BLF, {100, 100}, {0, 0}];
 “F(k=1)=F(i=1)” ;
 BLF1 = Table $\left[e^{-\frac{chEd[[i]]}{kT}}, \{i, 1, 52\} \right]$;
 dis = Table[BLF[i, j] = BLF1[[i]], {i, 1, 51}, {j, 0, 50}];
 “Lorenz profiles” ;
 “PQ1: Q1: kup=1,3,5..., jup=2,4,6.....,klow=1,3,5.... jlow=2,4,6....., ” ;
 PQ1 = Table[BLF[2i - 1, 2i]SQ1[[i]], {i, 1, 20}];
 eQ1 = Table $\left[\frac{PQ1[[i]]}{\lambda_{FQ1}[[i]]^3}, \{i, 1, 10\} \right]$;
 ProQ12 = Table $\left[\frac{2\Delta\lambda eQ1[[1]]}{\pi\Delta\lambda(4(De+\lambda_{exp}[[i]]-\lambda_{FQ1}[[1]])^2+\Delta\lambda^2)}, \{i, 1, dim\} \right]$;
 ProQ14 = Table $\left[\frac{2\Delta\lambda eQ1[[2]]}{\pi\Delta\lambda(4(De+\lambda_{exp}[[i]]-\lambda_{FQ1}[[2]])^2+\Delta\lambda^2)}, \{i, 1, dim\} \right]$;
 ProQ16 = Table $\left[\frac{2\Delta\lambda eQ1[[3]]}{\pi\Delta\lambda(4(De+\lambda_{exp}[[i]]-\lambda_{FQ1}[[3]])^2+\Delta\lambda^2)}, \{i, 1, dim\} \right]$;
 ProQ18 = Table $\left[\frac{2\Delta\lambda eQ1[[4]]}{\pi\Delta\lambda(4(De+\lambda_{exp}[[i]]-\lambda_{FQ1}[[4]])^2+\Delta\lambda^2)}, \{i, 1, dim\} \right]$;
 ProQ110 = Table $\left[\frac{2\Delta\lambda eQ1[[5]]}{\pi\Delta\lambda(4(De+\lambda_{exp}[[i]]-\lambda_{FQ1}[[5]])^2+\Delta\lambda^2)}, \{i, 1, dim\} \right]$;
 ProQ112 = Table $\left[\frac{2\Delta\lambda eQ1[[6]]}{\pi\Delta\lambda(4(De+\lambda_{exp}[[i]]-\lambda_{FQ1}[[6]])^2+\Delta\lambda^2)}, \{i, 1, dim\} \right]$;
 ProQ114 = Table $\left[\frac{2\Delta\lambda eQ1[[7]]}{\pi\Delta\lambda(4(De+\lambda_{exp}[[i]]-\lambda_{FQ1}[[7]])^2+\Delta\lambda^2)}, \{i, 1, dim\} \right]$;
 ProQ116 = Table $\left[\frac{2\Delta\lambda eQ1[[8]]}{\pi\Delta\lambda(4(De+\lambda_{exp}[[i]]-\lambda_{FQ1}[[8]])^2+\Delta\lambda^2)}, \{i, 1, dim\} \right]$;
 ProQ118 = Table $\left[\frac{2\Delta\lambda eQ1[[9]]}{\pi\Delta\lambda(4(De+\lambda_{exp}[[i]]-\lambda_{FQ1}[[9]])^2+\Delta\lambda^2)}, \{i, 1, dim\} \right]$;
 IQ1 = ProQ110 + ProQ112 + ProQ114 + ProQ116 + ProQ118+

ProQ12 + ProQ14 + ProQ16 + ProQ18;

“PQ2: kup=1,3,5..., jup=1,3,5.....,klow=1,3,5.... jlow=1,3,5....”;

PQ2 = Table[BLF[2i - 1, 2i - 1]SQ2[[i]], {i, 1, 20}];

eQ2 = Table $\left[\frac{\text{PQ2}[[i]]}{\lambda_{\text{FQ2}}[[i]]^3}, \{i, 1, 10\} \right]$;

ProQ21 = Table $\left[\frac{2\Delta\lambda eQ2[[1]]}{\pi\Delta\lambda(4(\text{De}+\lambda_{\text{exp}}[[i]]-\lambda_{\text{FQ2}}[[1]])^2+\Delta\lambda^2)}, \{i, 1, \text{dim}\} \right]$;

ProQ23 = Table $\left[\frac{2\Delta\lambda eQ2[[2]]}{\pi\Delta\lambda(4(\text{De}+\lambda_{\text{exp}}[[i]]-\lambda_{\text{FQ2}}[[2]])^2+\Delta\lambda^2)}, \{i, 1, \text{dim}\} \right]$;

ProQ25 = Table $\left[\frac{2\Delta\lambda eQ2[[3]]}{\pi\Delta\lambda(4(\text{De}+\lambda_{\text{exp}}[[i]]-\lambda_{\text{FQ2}}[[3]])^2+\Delta\lambda^2)}, \{i, 1, \text{dim}\} \right]$;

ProQ27 = Table $\left[\frac{2\Delta\lambda eQ2[[4]]}{\pi\Delta\lambda(4(\text{De}+\lambda_{\text{exp}}[[i]]-\lambda_{\text{FQ2}}[[4]])^2+\Delta\lambda^2)}, \{i, 1, \text{dim}\} \right]$;

ProQ29 = Table $\left[\frac{2\Delta\lambda eQ2[[5]]}{\pi\Delta\lambda(4(\text{De}+\lambda_{\text{exp}}[[i]]-\lambda_{\text{FQ2}}[[5]])^2+\Delta\lambda^2)}, \{i, 1, \text{dim}\} \right]$;

ProQ211 = Table $\left[\frac{2\Delta\lambda eQ2[[6]]}{\pi\Delta\lambda(4(\text{De}+\lambda_{\text{exp}}[[i]]-\lambda_{\text{FQ2}}[[6]])^2+\Delta\lambda^2)}, \{i, 1, \text{dim}\} \right]$;

ProQ213 = Table $\left[\frac{2\Delta\lambda eQ2[[7]]}{\pi\Delta\lambda(4(\text{De}+\lambda_{\text{exp}}[[i]]-\lambda_{\text{FQ2}}[[7]])^2+\Delta\lambda^2)}, \{i, 1, \text{dim}\} \right]$;

ProQ215 = Table $\left[\frac{2\Delta\lambda eQ2[[8]]}{\pi\Delta\lambda(4(\text{De}+\lambda_{\text{exp}}[[i]]-\lambda_{\text{FQ2}}[[8]])^2+\Delta\lambda^2)}, \{i, 1, \text{dim}\} \right]$;

ProQ217 = Table $\left[\frac{2\Delta\lambda eQ2[[9]]}{\pi\Delta\lambda(4(\text{De}+\lambda_{\text{exp}}[[i]]-\lambda_{\text{FQ2}}[[9]])^2+\Delta\lambda^2)}, \{i, 1, \text{dim}\} \right]$;

IQ2 = ProQ21 + ProQ211 + ProQ211 + ProQ213 + ProQ215 +

ProQ217 + ProQ23 + ProQ25 + ProQ27 + ProQ29;

“PQ3: Q3: kup=3,5..., jup=2,4,6.....,klow=3,5... jlow=2,4,6....”;

PQ3 = Table[BLF[2i + 1, 2i]SQ3[[i]], {i, 1, 20}];

eQ3 = Table $\left[\frac{\text{PQ3}[[i]]}{\lambda_{\text{FQ3}}[[i]]^3}, \{i, 1, 10\} \right]$;

ProQ32 = Table $\left[\frac{2\Delta\lambda eQ3[[1]]}{\pi\Delta\lambda(4(\text{De}+\lambda_{\text{exp}}[[i]]-\lambda_{\text{FQ3}}[[1]])^2+\Delta\lambda^2)}, \{i, 1, \text{dim}\} \right]$;

ProQ34 = Table $\left[\frac{2\Delta\lambda eQ3[[2]]}{\pi\Delta\lambda(4(\text{De}+\lambda_{\text{exp}}[[i]]-\lambda_{\text{FQ3}}[[2]])^2+\Delta\lambda^2)}, \{i, 1, \text{dim}\} \right]$;

ProQ36 = Table $\left[\frac{2\Delta\lambda eQ3[[3]]}{\pi\Delta\lambda(4(\text{De}+\lambda_{\text{exp}}[[i]]-\lambda_{\text{FQ3}}[[3]])^2+\Delta\lambda^2)}, \{i, 1, \text{dim}\} \right]$;

ProQ38 = Table $\left[\frac{2\Delta\lambda eQ3[[4]]}{\pi\Delta\lambda(4(\text{De}+\lambda_{\text{exp}}[[i]]-\lambda_{\text{FQ3}}[[4]])^2+\Delta\lambda^2)}, \{i, 1, \text{dim}\} \right]$;

ProQ310 = Table $\left[\frac{2\Delta\lambda eQ3[[5]]}{\pi\Delta\lambda(4(\text{De}+\lambda_{\text{exp}}[[i]]-\lambda_{\text{FQ3}}[[5]])^2+\Delta\lambda^2)}, \{i, 1, \text{dim}\} \right]$;

ProQ312 = Table $\left[\frac{2\Delta\lambda eQ3[[6]]}{\pi\Delta\lambda(4(\text{De}+\lambda_{\text{exp}}[[i]]-\lambda_{\text{FQ3}}[[6]])^2+\Delta\lambda^2)}, \{i, 1, \text{dim}\} \right]$;

ProQ314 = Table $\left[\frac{2\Delta\lambda eQ3[[7]]}{\pi\Delta\lambda(4(\text{De}+\lambda_{\text{exp}}[[i]]-\lambda_{\text{FQ3}}[[7]])^2+\Delta\lambda^2)}, \{i, 1, \text{dim}\} \right]$;

$$\text{ProQ316} = \text{Table} \left[\frac{2\Delta\lambda e_{\text{Q3}}[[8]]}{\pi\Delta\lambda(4(\text{De}+\lambda_{\text{exp}}[[i]]-\lambda_{\text{FP3}}[[8]])^2+\Delta\lambda^2)}, \{i, 1, \text{dim}\} \right];$$

$$\text{IQ3} = \text{ProQ310} + \text{ProQ312} + \text{ProQ314} + \text{ProQ316} +$$

$$\text{ProQ32} + \text{ProQ34} + \text{ProQ36} + \text{ProQ38};$$

“PP1: P1: kup=1,3,5..., jup=2,4,6.....,klow=2,4,6..... jlow=3,5...”;

$$\text{PP1} = \text{Table}[\text{BLF}[2i - 1, 2i]\text{SP1}[[i]], \{i, 1, 20\}];$$

$$\text{eP1} = \text{Table} \left[\frac{\text{PP1}[[i]]}{\lambda_{\text{FP1}}[[i]]^3}, \{i, 1, 15\} \right];$$

$$\text{ProP12} = \text{Table} \left[\frac{2\Delta\lambda e_{\text{P1}}[[1]]}{\pi\Delta\lambda(4(\text{De}+\lambda_{\text{exp}}[[i]]-\lambda_{\text{FP1}}[[1]])^2+\Delta\lambda^2)}, \{i, 1, \text{dim}\} \right];$$

$$\text{ProP14} = \text{Table} \left[\frac{2\Delta\lambda e_{\text{P1}}[[2]]}{\pi\Delta\lambda(4(\text{De}+\lambda_{\text{exp}}[[i]]-\lambda_{\text{FP1}}[[2]])^2+\Delta\lambda^2)}, \{i, 1, \text{dim}\} \right];$$

$$\text{ProP16} = \text{Table} \left[\frac{2\Delta\lambda e_{\text{P1}}[[3]]}{\pi\Delta\lambda(4(\text{De}+\lambda_{\text{exp}}[[i]]-\lambda_{\text{FP1}}[[3]])^2+\Delta\lambda^2)}, \{i, 1, \text{dim}\} \right];$$

$$\text{ProP18} = \text{Table} \left[\frac{2\Delta\lambda e_{\text{P1}}[[4]]}{\pi\Delta\lambda(4(\text{De}+\lambda_{\text{exp}}[[i]]-\lambda_{\text{FP1}}[[4]])^2+\Delta\lambda^2)}, \{i, 1, \text{dim}\} \right];$$

$$\text{ProP110} = \text{Table} \left[\frac{2\Delta\lambda e_{\text{P1}}[[5]]}{\pi\Delta\lambda(4(\text{De}+\lambda_{\text{exp}}[[i]]-\lambda_{\text{FP1}}[[5]])^2+\Delta\lambda^2)}, \{i, 1, \text{dim}\} \right];$$

$$\text{ProP112} = \text{Table} \left[\frac{2\Delta\lambda e_{\text{P1}}[[6]]}{\pi\Delta\lambda(4(\text{De}+\lambda_{\text{exp}}[[i]]-\lambda_{\text{FP1}}[[6]])^2+\Delta\lambda^2)}, \{i, 1, \text{dim}\} \right];$$

$$\text{ProP114} = \text{Table} \left[\frac{2\Delta\lambda e_{\text{P1}}[[7]]}{\pi\Delta\lambda(4(\text{De}+\lambda_{\text{exp}}[[i]]-\lambda_{\text{FP1}}[[7]])^2+\Delta\lambda^2)}, \{i, 1, \text{dim}\} \right];$$

$$\text{ProP116} = \text{Table} \left[\frac{2\Delta\lambda e_{\text{P1}}[[8]]}{\pi\Delta\lambda(4(\text{De}+\lambda_{\text{exp}}[[i]]-\lambda_{\text{FP1}}[[8]])^2+\Delta\lambda^2)}, \{i, 1, \text{dim}\} \right];$$

$$\text{ProP118} = \text{Table} \left[\frac{2\Delta\lambda e_{\text{P1}}[[9]]}{\pi\Delta\lambda(4(\text{De}+\lambda_{\text{exp}}[[i]]-\lambda_{\text{FP1}}[[9]])^2+\Delta\lambda^2)}, \{i, 1, \text{dim}\} \right];$$

$$\text{ProP120} = \text{Table} \left[\frac{2\Delta\lambda e_{\text{P1}}[[10]]}{\pi\Delta\lambda(4(\text{De}+\lambda_{\text{exp}}[[i]]-\lambda_{\text{FP1}}[[10]])^2+\Delta\lambda^2)}, \{i, 1, \text{dim}\} \right];$$

$$\text{ProP122} = \text{Table} \left[\frac{2\Delta\lambda e_{\text{P1}}[[11]]}{\pi\Delta\lambda(4(\text{De}+\lambda_{\text{exp}}[[i]]-\lambda_{\text{FP1}}[[11]])^2+\Delta\lambda^2)}, \{i, 1, \text{dim}\} \right];$$

$$\text{IP1} = \text{ProP110} + \text{ProP112} + \text{ProP114} + \text{ProP116} + \text{ProP118} +$$

$$\text{ProP12} + \text{ProP120} + \text{ProP122} + \text{ProP14} + \text{ProP16} + \text{ProP18};$$

“PP2: P2: kup=1,3,5..., jup=1,3,5.....,klow=2,4,6..... jlow=2,4,6....”;

$$\text{PP2} = \text{Table}[\text{BLF}[2i - 1, 2i - 1]\text{SP2}[[i]], \{i, 1, 20\}];$$

$$\text{eP2} = \text{Table} \left[\frac{\text{PP2}[[i]]}{\lambda_{\text{FP2}}[[i]]^3}, \{i, 1, 12\} \right];$$

$$\text{ProP21} = \text{Table} \left[\frac{2\Delta\lambda e_{\text{P2}}[[1]]}{\pi\Delta\lambda(4(\text{De}+\lambda_{\text{exp}}[[i]]-\lambda_{\text{FP2}}[[1]])^2+\Delta\lambda^2)}, \{i, 1, \text{dim}\} \right];$$

$$\text{ProP23} = \text{Table} \left[\frac{2\Delta\lambda e_{\text{P2}}[[2]]}{\pi\Delta\lambda(4(\text{De}+\lambda_{\text{exp}}[[i]]-\lambda_{\text{FP2}}[[2]])^2+\Delta\lambda^2)}, \{i, 1, \text{dim}\} \right];$$

$$\text{ProP25} = \text{Table} \left[\frac{2\Delta\lambda e_{\text{P2}}[[3]]}{\pi\Delta\lambda(4(\text{De}+\lambda_{\text{exp}}[[i]]-\lambda_{\text{FP2}}[[3]])^2+\Delta\lambda^2)}, \{i, 1, \text{dim}\} \right];$$

$$\text{ProP27} = \text{Table} \left[\frac{2\Delta\lambda e_{\text{P2}}[[4]]}{\pi\Delta\lambda(4(\text{De}+\lambda_{\text{exp}}[[i]]-\lambda_{\text{FP2}}[[4]])^2+\Delta\lambda^2)}, \{i, 1, \text{dim}\} \right];$$

$$\text{ProP29} = \text{Table} \left[\frac{2\Delta\lambda e_{\text{P2}}[[5]]}{\pi\Delta\lambda(4(\text{De}+\lambda_{\text{exp}}[[i]]-\lambda_{\text{FP2}}[[5]])^2+\Delta\lambda^2)}, \{i, 1, \text{dim}\} \right];$$

$$\text{ProP211} = \text{Table} \left[\frac{2\Delta\lambda e_{\text{P2}}[[6]]}{\pi\Delta\lambda(4(\text{De}+\lambda_{\text{exp}}[[i]]-\lambda_{\text{FP2}}[[6]])^2+\Delta\lambda^2)}, \{i, 1, \text{dim}\} \right];$$

$$\text{ProP213} = \text{Table} \left[\frac{2\Delta\lambda e_{\text{P2}}[[7]]}{\pi\Delta\lambda(4(\text{De}+\lambda_{\text{exp}}[[i]]-\lambda_{\text{FP2}}[[7]])^2+\Delta\lambda^2)}, \{i, 1, \text{dim}\} \right];$$

$$IP2 = \text{ProP21} + \text{ProP211} + \text{ProP213} + \text{ProP23} + \text{ProP25} + \text{ProP27} + \text{ProP29};$$

$$\text{"PP3: P3: kup}=1,3,5\dots, \text{jup}=0,2,4\dots, \text{klow}=2,4,6\dots \text{jlow}=1,3,5\dots \text{"};$$

$$PP3 = \text{Table}[\text{BLF}[2i - 1, 2i - 2] \text{SP3}[[i]], \{i, 1, 20\}];$$

$$eP3 = \text{Table} \left[\frac{PP3[[i]]}{\lambda_{FP3}[[i]]^3}, \{i, 1, 15\} \right];$$

$$\text{ProP30} = \text{Table} \left[\frac{2\Delta\lambda eP3[[1]]}{\pi\Delta\lambda(4(\text{De} + \lambda_{\text{exp}}[[i]] - \lambda_{FP3}[[1]])^2 + \Delta\lambda^2)}, \{i, 1, \text{dim}\} \right];$$

$$\text{ProP32} = \text{Table} \left[\frac{2\Delta\lambda eP3[[2]]}{\pi\Delta\lambda(4(\text{De} + \lambda_{\text{exp}}[[i]] - \lambda_{FP3}[[2]])^2 + \Delta\lambda^2)}, \{i, 1, \text{dim}\} \right];$$

$$\text{ProP34} = \text{Table} \left[\frac{2\Delta\lambda eP3[[3]]}{\pi\Delta\lambda(4(\text{De} + \lambda_{\text{exp}}[[i]] - \lambda_{FP3}[[3]])^2 + \Delta\lambda^2)}, \{i, 1, \text{dim}\} \right];$$

$$\text{ProP36} = \text{Table} \left[\frac{2\Delta\lambda eP3[[4]]}{\pi\Delta\lambda(4(\text{De} + \lambda_{\text{exp}}[[i]] - \lambda_{FP3}[[4]])^2 + \Delta\lambda^2)}, \{i, 1, \text{dim}\} \right];$$

$$\text{ProP38} = \text{Table} \left[\frac{2\Delta\lambda eP3[[5]]}{\pi\Delta\lambda(4(\text{De} + \lambda_{\text{exp}}[[i]] - \lambda_{FP3}[[5]])^2 + \Delta\lambda^2)}, \{i, 1, \text{dim}\} \right];$$

$$\text{ProP310} = \text{Table} \left[\frac{2\Delta\lambda eP3[[6]]}{\pi\Delta\lambda(4(\text{De} + \lambda_{\text{exp}}[[i]] - \lambda_{FP3}[[6]])^2 + \Delta\lambda^2)}, \{i, 1, \text{dim}\} \right];$$

$$\text{ProP312} = \text{Table} \left[\frac{2\Delta\lambda eP3[[7]]}{\pi\Delta\lambda(4(\text{De} + \lambda_{\text{exp}}[[i]] - \lambda_{FP3}[[7]])^2 + \Delta\lambda^2)}, \{i, 1, \text{dim}\} \right];$$

$$IP3 = \text{ProP30} + \text{ProP310} + \text{ProP312} + \text{ProP32} + \text{ProP34} + \text{ProP36} + \text{ProP38};$$

$$\text{"PR1: R1: kup}=3,5\dots, \text{jup}=4,6,8,10\dots, \text{klow}=2,4,6\dots \text{jlow}=3,5\dots \text{"};$$

$$PR1 = \text{Table}[\text{BLF}[2i + 1, 2i + 2] \text{SR1}[[i]], \{i, 1, 14\}];$$

$$eR1 = \text{Table} \left[\frac{PR1[[i]]}{\lambda_{FR1}[[i]]^3}, \{i, 1, 14\} \right];$$

$$\text{ProR14} = \text{Table} \left[\frac{2\Delta\lambda eR1[[1]]}{\pi\Delta\lambda(4(\text{De} + \lambda_{\text{exp}}[[i]] - \lambda_{FR1}[[1]])^2 + \Delta\lambda^2)}, \{i, 1, \text{dim}\} \right];$$

$$\text{ProR16} = \text{Table} \left[\frac{2\Delta\lambda eR1[[2]]}{\pi\Delta\lambda(4(\text{De} + \lambda_{\text{exp}}[[i]] - \lambda_{FR1}[[2]])^2 + \Delta\lambda^2)}, \{i, 1, \text{dim}\} \right];$$

$$\text{ProR18} = \text{Table} \left[\frac{2\Delta\lambda eR1[[3]]}{\pi\Delta\lambda(4(\text{De} + \lambda_{\text{exp}}[[i]] - \lambda_{FR1}[[3]])^2 + \Delta\lambda^2)}, \{i, 1, \text{dim}\} \right];$$

$$\text{ProR110} = \text{Table} \left[\frac{2\Delta\lambda eR1[[4]]}{\pi\Delta\lambda(4(\text{De} + \lambda_{\text{exp}}[[i]] - \lambda_{FR1}[[4]])^2 + \Delta\lambda^2)}, \{i, 1, \text{dim}\} \right];$$

$$\text{ProR112} = \text{Table} \left[\frac{2\Delta\lambda eR1[[5]]}{\pi\Delta\lambda(4(\text{De} + \lambda_{\text{exp}}[[i]] - \lambda_{FR1}[[5]])^2 + \Delta\lambda^2)}, \{i, 1, \text{dim}\} \right];$$

$$\text{ProR114} = \text{Table} \left[\frac{2\Delta\lambda eR1[[6]]}{\pi\Delta\lambda(4(\text{De} + \lambda_{\text{exp}}[[i]] - \lambda_{FR1}[[6]])^2 + \Delta\lambda^2)}, \{i, 1, \text{dim}\} \right];$$

$$\text{ProR116} = \text{Table} \left[\frac{2\Delta\lambda eR1[[7]]}{\pi\Delta\lambda(4(\text{De} + \lambda_{\text{exp}}[[i]] - \lambda_{FR1}[[7]])^2 + \Delta\lambda^2)}, \{i, 1, \text{dim}\} \right];$$

$$\text{ProR118} = \text{Table} \left[\frac{2\Delta\lambda eR1[[8]]}{\pi\Delta\lambda(4(\text{De} + \lambda_{\text{exp}}[[i]] - \lambda_{FR1}[[8]])^2 + \Delta\lambda^2)}, \{i, 1, \text{dim}\} \right];$$

$$IR1 = \text{ProR110} + \text{ProR112} + \text{ProR114} + \text{ProR116} + \text{ProR118} +$$

$$\text{ProR14} + \text{ProR16} + \text{ProR18};$$

$$\text{"PR2: R2: kup}=3,5\dots, \text{jup}=3,5\dots, \text{klow}=2,4,6\dots \text{jlow}=2,4,6\dots \text{"};$$

$$PR2 = \text{Table}[\text{BLF}[2i + 1, 2i + 1] \text{SR2}[[i]], \{i, 1, 22\}];$$

$$eR2 = \text{Table} \left[\frac{PR2[[i]]}{\lambda_{FR2}[[i]]^3}, \{i, 1, 15\} \right];$$

$$\text{ProR23} = \text{Table} \left[\frac{2\Delta\lambda eR2[[1]]}{\pi\Delta\lambda(4(\text{De} + \lambda_{\text{exp}}[[i]] - \lambda_{FR2}[[1]])^2 + \Delta\lambda^2)}, \{i, 1, \text{dim}\} \right];$$

$$\begin{aligned}
\text{ProR25} &= \text{Table} \left[\frac{2\Delta\lambda eR2[[2]]}{\pi\Delta\lambda(4(\text{De}+\lambda_{\text{exp}}[[i]]-\lambda_{\text{FR2}}[[2]])^2+\Delta\lambda^2)}, \{i, 1, \text{dim}\} \right]; \\
\text{ProR27} &= \text{Table} \left[\frac{2\Delta\lambda eR2[[3]]}{\pi\Delta\lambda(4(\text{De}+\lambda_{\text{exp}}[[i]]-\lambda_{\text{FR2}}[[3]])^2+\Delta\lambda^2)}, \{i, 1, \text{dim}\} \right]; \\
\text{ProR29} &= \text{Table} \left[\frac{2\Delta\lambda eR2[[4]]}{\pi\Delta\lambda(4(\text{De}+\lambda_{\text{exp}}[[i]]-\lambda_{\text{FR2}}[[4]])^2+\Delta\lambda^2)}, \{i, 1, \text{dim}\} \right]; \\
\text{ProR211} &= \text{Table} \left[\frac{2\Delta\lambda eR2[[5]]}{\pi\Delta\lambda(4(\text{De}+\lambda_{\text{exp}}[[i]]-\lambda_{\text{FR2}}[[5]])^2+\Delta\lambda^2)}, \{i, 1, \text{dim}\} \right]; \\
\text{ProR213} &= \text{Table} \left[\frac{2\Delta\lambda eR2[[6]]}{\pi\Delta\lambda(4(\text{De}+\lambda_{\text{exp}}[[i]]-\lambda_{\text{FR2}}[[6]])^2+\Delta\lambda^2)}, \{i, 1, \text{dim}\} \right]; \\
\text{ProR215} &= \text{Table} \left[\frac{2\Delta\lambda eR2[[7]]}{\pi\Delta\lambda(4(\text{De}+\lambda_{\text{exp}}[[i]]-\lambda_{\text{FR2}}[[7]])^2+\Delta\lambda^2)}, \{i, 1, \text{dim}\} \right]; \\
\text{ProR217} &= \text{Table} \left[\frac{2\Delta\lambda eR2[[8]]}{\pi\Delta\lambda(4(\text{De}+\lambda_{\text{exp}}[[i]]-\lambda_{\text{FR2}}[[8]])^2+\Delta\lambda^2)}, \{i, 1, \text{dim}\} \right]; \\
\text{IR2} &= \text{ProR211} + \text{ProR213} + \text{ProR215} + \text{ProR217} + \text{ProR23} + \\
&\text{ProR25} + \text{ProR27} + \text{ProR29};
\end{aligned}$$

“PR3:R3: kup=3,5..., jup=2,4,6..., klow=2,4,6... jlow=1,3,5... ”;

$$\text{PR3} = \text{Table}[\text{BLF}[2i + 1, 2i]\text{SR3}[[i]], \{i, 1, 20\}];$$

$$\text{eR3} = \text{Table} \left[\frac{\text{PR3}[[i]]}{\lambda_{\text{FR3}}[[i]]^3}, \{i, 1, 15\} \right];$$

$$\begin{aligned}
\text{ProR32} &= \text{Table} \left[\frac{2\Delta\lambda eR3[[1]]}{\pi\Delta\lambda(4(\text{De}+\lambda_{\text{exp}}[[i]]-\lambda_{\text{FR3}}[[1]])^2+\Delta\lambda^2)}, \{i, 1, \text{dim}\} \right]; \\
\text{ProR34} &= \text{Table} \left[\frac{2\Delta\lambda eR3[[2]]}{\pi\Delta\lambda(4(\text{De}+\lambda_{\text{exp}}[[i]]-\lambda_{\text{FR3}}[[2]])^2+\Delta\lambda^2)}, \{i, 1, \text{dim}\} \right]; \\
\text{ProR36} &= \text{Table} \left[\frac{2\Delta\lambda eR3[[3]]}{\pi\Delta\lambda(4(\text{De}+\lambda_{\text{exp}}[[i]]-\lambda_{\text{FR3}}[[3]])^2+\Delta\lambda^2)}, \{i, 1, \text{dim}\} \right]; \\
\text{ProR38} &= \text{Table} \left[\frac{2\Delta\lambda eR3[[4]]}{\pi\Delta\lambda(4(\text{De}+\lambda_{\text{exp}}[[i]]-\lambda_{\text{FR3}}[[4]])^2+\Delta\lambda^2)}, \{i, 1, \text{dim}\} \right]; \\
\text{ProR310} &= \text{Table} \left[\frac{2\Delta\lambda eR3[[5]]}{\pi\Delta\lambda(4(\text{De}+\lambda_{\text{exp}}[[i]]-\lambda_{\text{FR3}}[[5]])^2+\Delta\lambda^2)}, \{i, 1, \text{dim}\} \right]; \\
\text{ProR312} &= \text{Table} \left[\frac{2\Delta\lambda eR3[[6]]}{\pi\Delta\lambda(4(\text{De}+\lambda_{\text{exp}}[[i]]-\lambda_{\text{FR3}}[[6]])^2+\Delta\lambda^2)}, \{i, 1, \text{dim}\} \right]; \\
\text{ProR314} &= \text{Table} \left[\frac{2\Delta\lambda eR3[[7]]}{\pi\Delta\lambda(4(\text{De}+\lambda_{\text{exp}}[[i]]-\lambda_{\text{FR3}}[[7]])^2+\Delta\lambda^2)}, \{i, 1, \text{dim}\} \right]; \\
\text{IR3} &= \text{ProR310} + \text{ProR312} + \text{ProR314} + \text{ProR32} + \text{ProR34} + \\
&\text{ProR36} + \text{ProR38};
\end{aligned}$$

“PQR12: QR12: kup=1,3,5..., jup=2,4,6..., klow=1,3,5,7,9,11... jlow=1,3,5,7,9,11... ”;

$$\text{PQR12} = \text{Table}[\text{BLF}[2i - 1, 2i]\text{SQR12}[[i]], \{i, 1, 20\}];$$

$$\text{eQR12} = \text{Table} \left[\frac{\text{PQR12}[[i]]}{\lambda_{\text{FQR12}}[[i]]^3}, \{i, 1, 12\} \right];$$

$$\begin{aligned}
\text{ProQR122} &= \text{Table} \left[\frac{2\Delta\lambda eQR12[[1]]}{\pi\Delta\lambda(4(\text{De}+\lambda_{\text{exp}}[[i]]-\lambda_{\text{FQR12}}[[1]])^2+\Delta\lambda^2)}, \{i, 1, \text{dim}\} \right]; \\
\text{ProQR124} &= \text{Table} \left[\frac{2\Delta\lambda eQR12[[2]]}{\pi\Delta\lambda(4(\text{De}+\lambda_{\text{exp}}[[i]]-\lambda_{\text{FQR12}}[[2]])^2+\Delta\lambda^2)}, \{i, 1, \text{dim}\} \right]; \\
\text{ProQR126} &= \text{Table} \left[\frac{2\Delta\lambda eQR12[[3]]}{\pi\Delta\lambda(4(\text{De}+\lambda_{\text{exp}}[[i]]-\lambda_{\text{FQR12}}[[3]])^2+\Delta\lambda^2)}, \{i, 1, \text{dim}\} \right]; \\
\text{ProQR128} &= \text{Table} \left[\frac{2\Delta\lambda eQR12[[4]]}{\pi\Delta\lambda(4(\text{De}+\lambda_{\text{exp}}[[i]]-\lambda_{\text{FQR12}}[[4]])^2+\Delta\lambda^2)}, \{i, 1, \text{dim}\} \right];
\end{aligned}$$

$$\begin{aligned}
\text{ProQR1210} &= \text{Table} \left[\frac{2\Delta\lambda\text{eQR12}[[5]]}{\pi\Delta\lambda(4(\text{De}+\lambda_{\text{exp}}[[i]]-\lambda_{\text{FQR12}}[[5]])^2+\Delta\lambda^2)}, \{i, 1, \text{dim}\} \right]; \\
\text{ProQR1212} &= \text{Table} \left[\frac{2\Delta\lambda\text{eQR12}[[4]]}{\pi\Delta\lambda(4(\text{De}+\lambda_{\text{exp}}[[i]]-\lambda_{\text{FQR12}}[[6]])^2+\Delta\lambda^2)}, \{i, 1, \text{dim}\} \right]; \\
\text{IQR12} &= \text{ProQR1210} + \text{ProQR1212} + \text{ProQR122} + \\
&\text{ProQR124} + \text{ProQR126} + \text{ProQR128}; \\
\text{"PQR23: QR23: kup=1,3,5..., jup=1,3,5.....,klow=1,3,5..... jlow=0,2,4,..."}; \\
\text{PQR23} &= \text{Table}[\text{BLF}[2i - 1, 2i - 1]\text{SQR23}[[i]], \{i, 1, 20\}]; \\
\text{eQR23} &= \text{Table} \left[\frac{\text{PQR23}[[i]]}{\lambda_{\text{FQR23}}[[i]]^3}, \{i, 1, 12\} \right]; \\
\text{ProQR231} &= \text{Table} \left[\frac{2\Delta\lambda\text{eQR23}[[1]]}{\pi\Delta\lambda(4(\text{De}+\lambda_{\text{exp}}[[i]]-\lambda_{\text{FQR23}}[[1]])^2+\Delta\lambda^2)}, \{i, 1, \text{dim}\} \right]; \\
\text{ProQR233} &= \text{Table} \left[\frac{2\Delta\lambda\text{eQR23}[[2]]}{\pi\Delta\lambda(4(\text{De}+\lambda_{\text{exp}}[[i]]-\lambda_{\text{FQR23}}[[2]])^2+\Delta\lambda^2)}, \{i, 1, \text{dim}\} \right]; \\
\text{ProQR235} &= \text{Table} \left[\frac{2\Delta\lambda\text{eQR23}[[3]]}{\pi\Delta\lambda(4(\text{De}+\lambda_{\text{exp}}[[i]]-\lambda_{\text{FQR23}}[[3]])^2+\Delta\lambda^2)}, \{i, 1, \text{dim}\} \right]; \\
\text{ProQR237} &= \text{Table} \left[\frac{2\Delta\lambda\text{eQR23}[[4]]}{\pi\Delta\lambda(4(\text{De}+\lambda_{\text{exp}}[[i]]-\lambda_{\text{FQR23}}[[4]])^2+\Delta\lambda^2)}, \{i, 1, \text{dim}\} \right]; \\
\text{ProQR239} &= \text{Table} \left[\frac{2\Delta\lambda\text{eQR23}[[5]]}{\pi\Delta\lambda(4(\text{De}+\lambda_{\text{exp}}[[i]]-\lambda_{\text{FQR23}}[[5]])^2+\Delta\lambda^2)}, \{i, 1, \text{dim}\} \right]; \\
\text{IQR23} &= \text{ProQR231} + \text{ProQR233} + \text{ProQR235} + \text{ProQR237} + \text{ProQR239}; \\
\text{"PQP21: QP21: kup=1,3,5..., jup=1,3,5.....,klow=1,3,5..... jlow=2,4,..."}; \\
\text{PQP21} &= \text{Table}[\text{BLF}[2i - 1, 2i - 1]\text{SQP21}[[i]], \{i, 1, 20\}]; \\
\text{eQP21} &= \text{Table} \left[\frac{\text{PQP21}[[i]]}{\lambda_{\text{FQP21}}[[i]]^3}, \{i, 1, 12\} \right]; \\
\text{ProQP211} &= \text{Table} \left[\frac{2\Delta\lambda\text{eQP21}[[1]]}{\pi\Delta\lambda(4(\text{De}+\lambda_{\text{exp}}[[i]]-\lambda_{\text{FQP21}}[[1]])^2+\Delta\lambda^2)}, \{i, 1, \text{dim}\} \right]; \\
\text{ProQP213} &= \text{Table} \left[\frac{2\Delta\lambda\text{eQP21}[[2]]}{\pi\Delta\lambda(4(\text{De}+\lambda_{\text{exp}}[[i]]-\lambda_{\text{FQP21}}[[2]])^2+\Delta\lambda^2)}, \{i, 1, \text{dim}\} \right]; \\
\text{ProQP215} &= \text{Table} \left[\frac{2\Delta\lambda\text{eQP21}[[3]]}{\pi\Delta\lambda(4(\text{De}+\lambda_{\text{exp}}[[i]]-\lambda_{\text{FQP21}}[[3]])^2+\Delta\lambda^2)}, \{i, 1, \text{dim}\} \right]; \\
\text{ProQP217} &= \text{Table} \left[\frac{2\Delta\lambda\text{eQP21}[[4]]}{\pi\Delta\lambda(4(\text{De}+\lambda_{\text{exp}}[[i]]-\lambda_{\text{FQP21}}[[4]])^2+\Delta\lambda^2)}, \{i, 1, \text{dim}\} \right]; \\
\text{ProQP219} &= \text{Table} \left[\frac{2\Delta\lambda\text{eQP21}[[5]]}{\pi\Delta\lambda(4(\text{De}+\lambda_{\text{exp}}[[i]]-\lambda_{\text{FQP21}}[[5]])^2+\Delta\lambda^2)}, \{i, 1, \text{dim}\} \right]; \\
\text{IQP21} &= \text{ProQP211} + \text{ProQP213} + \text{ProQP215} + \text{ProQP217} + \text{ProQP219}; \\
\text{"PQP32: QP21: kup=1,3,5..., jup=0,2,4,6.....,klow=1,3,5..... jlow=1,3,5,..."}; \\
\text{PQP32} &= \text{Table}[\text{BLF}[2i - 1, 2i - 2]\text{SQP32}[[i]], \{i, 1, 20\}]; \\
\text{eQP32} &= \text{Table} \left[\frac{\text{PQP32}[[i]]}{\lambda_{\text{FQP32}}[[i]]^3}, \{i, 1, 12\} \right]; \\
\text{ProQP321} &= \text{Table} \left[\frac{2\Delta\lambda\text{eQP32}[[1]]}{\pi\Delta\lambda(4(\text{De}+\lambda_{\text{exp}}[[i]]-\lambda_{\text{FQP32}}[[1]])^2+\Delta\lambda^2)}, \{i, 1, \text{dim}\} \right];
\end{aligned}$$

$$\begin{aligned}
\text{ProQP323} &= \text{Table} \left[\frac{2\Delta\lambda\text{eQP32}[[2]]}{\pi\Delta\lambda(4(\text{De}+\lambda_{\text{exp}}[[i]]-\lambda_{\text{FQP32}}[[2]])^2+\Delta\lambda^2)}, \{i, 1, \text{dim}\} \right]; \\
\text{ProQP325} &= \text{Table} \left[\frac{2\Delta\lambda\text{eQP32}[[3]]}{\pi\Delta\lambda(4(\text{De}+\lambda_{\text{exp}}[[i]]-\lambda_{\text{FQP32}}[[3]])^2+\Delta\lambda^2)}, \{i, 1, \text{dim}\} \right]; \\
\text{ProQP327} &= \text{Table} \left[\frac{2\Delta\lambda\text{eQP32}[[4]]}{\pi\Delta\lambda(4(\text{De}+\lambda_{\text{exp}}[[i]]-\lambda_{\text{FQP32}}[[4]])^2+\Delta\lambda^2)}, \{i, 1, \text{dim}\} \right]; \\
\text{ProQP329} &= \text{Table} \left[\frac{2\Delta\lambda\text{eQP32}[[5]]}{\pi\Delta\lambda(4(\text{De}+\lambda_{\text{exp}}[[i]]-\lambda_{\text{FQP32}}[[5]])^2+\Delta\lambda^2)}, \{i, 1, \text{dim}\} \right]; \\
\text{IQP32} &= \text{ProQP321} + \text{ProQP323} + \text{ProQP325} + \text{ProQP327} + \text{ProQP329}; \\
\text{“PPQ12: PQ12: kup=1,3,5..., jup=2,4,6...,klow=2,4,6..... jlow=2,4,6....”}; \\
\text{PPQ12} &= \text{Table}[\text{BLF}[2i - 1, 2i]\text{SPQ12}[[i]], \{i, 1, 20\}]; \\
\text{ePQ12} &= \text{Table} \left[\frac{\text{PPQ12}[[i]]}{\lambda_{\text{FPQ12}}[[i]]^3}, \{i, 1, 12\} \right]; \\
\text{ProPQ121} &= \text{Table} \left[\frac{2\Delta\lambda\text{ePQ12}[[1]]}{\pi\Delta\lambda(4(\text{De}+\lambda_{\text{exp}}[[i]]-\lambda_{\text{FPQ12}}[[1]])^2+\Delta\lambda^2)}, \{i, 1, \text{dim}\} \right]; \\
\text{ProPQ123} &= \text{Table} \left[\frac{2\Delta\lambda\text{ePQ12}[[2]]}{\pi\Delta\lambda(4(\text{De}+\lambda_{\text{exp}}[[i]]-\lambda_{\text{FPQ12}}[[2]])^2+\Delta\lambda^2)}, \{i, 1, \text{dim}\} \right]; \\
\text{ProPQ125} &= \text{Table} \left[\frac{2\Delta\lambda\text{ePQ12}[[3]]}{\pi\Delta\lambda(4(\text{De}+\lambda_{\text{exp}}[[i]]-\lambda_{\text{FPQ12}}[[3]])^2+\Delta\lambda^2)}, \{i, 1, \text{dim}\} \right]; \\
\text{ProPQ127} &= \text{Table} \left[\frac{2\Delta\lambda\text{ePQ12}[[4]]}{\pi\Delta\lambda(4(\text{De}+\lambda_{\text{exp}}[[i]]-\lambda_{\text{FPQ12}}[[4]])^2+\Delta\lambda^2)}, \{i, 1, \text{dim}\} \right]; \\
\text{ProPQ129} &= \text{Table} \left[\frac{2\Delta\lambda\text{ePQ12}[[5]]}{\pi\Delta\lambda(4(\text{De}+\lambda_{\text{exp}}[[i]]-\lambda_{\text{FPQ12}}[[5]])^2+\Delta\lambda^2)}, \{i, 1, \text{dim}\} \right]; \\
\text{IPQ12} &= \text{ProPQ121} + \text{ProPQ123} + \text{ProPQ125} + \text{ProPQ127} + \text{ProPQ129}; \\
\text{“PPR13: PQ23: kup=1,3,5..., jup=1,3,5...,klow=2,4,6..... jlow=1,3,5....”}; \\
\text{PPQ23} &= \text{Table}[\text{BLF}[2i - 1, 2i - 1]\text{SPQ23}[[i]], \{i, 1, 20\}]; \\
\text{ePQ23} &= \text{Table} \left[\frac{\text{PPQ23}[[i]]}{\lambda_{\text{FPQ23}}[[i]]^3}, \{i, 1, 12\} \right]; \\
\text{ProPQ231} &= \text{Table} \left[\frac{2\Delta\lambda\text{ePQ23}[[1]]}{\pi\Delta\lambda(4(\text{De}+\lambda_{\text{exp}}[[i]]-\lambda_{\text{FPQ23}}[[1]])^2+\Delta\lambda^2)}, \{i, 1, \text{dim}\} \right]; \\
\text{ProPQ233} &= \text{Table} \left[\frac{2\Delta\lambda\text{ePQ23}[[2]]}{\pi\Delta\lambda(4(\text{De}+\lambda_{\text{exp}}[[i]]-\lambda_{\text{FPQ23}}[[2]])^2+\Delta\lambda^2)}, \{i, 1, \text{dim}\} \right]; \\
\text{ProPQ235} &= \text{Table} \left[\frac{2\Delta\lambda\text{ePQ23}[[3]]}{\pi\Delta\lambda(4(\text{De}+\lambda_{\text{exp}}[[i]]-\lambda_{\text{FPQ23}}[[3]])^2+\Delta\lambda^2)}, \{i, 1, \text{dim}\} \right]; \\
\text{ProPQ237} &= \text{Table} \left[\frac{2\Delta\lambda\text{ePQ23}[[4]]}{\pi\Delta\lambda(4(\text{De}+\lambda_{\text{exp}}[[i]]-\lambda_{\text{FPQ23}}[[4]])^2+\Delta\lambda^2)}, \{i, 1, \text{dim}\} \right]; \\
\text{IPQ23} &= \text{ProPQ231} + \text{ProPQ233} + \text{ProPQ235} + \text{ProPQ237}; \\
\text{“PPR13: PR13: kup=1,3,5..., jup=2,4,6...,klow=2,4,6..... jlow=1,3,5....”}; \\
\text{PPR13} &= \text{Table}[\text{BLF}[2i - 1, 2i]\text{SPR13}[[i]], \{i, 1, 20\}]; \\
\text{ePR13} &= \text{Table} \left[\frac{\text{PPR13}[[i]]}{\lambda_{\text{FPR13}}[[i]]^3}, \{i, 1, 12\} \right]; \\
\text{ProPR131} &= \text{Table} \left[\frac{2\Delta\lambda\text{ePR13}[[1]]}{\pi\Delta\lambda(4(\text{De}+\lambda_{\text{exp}}[[i]]-\lambda_{\text{FPR13}}[[1]])^2+\Delta\lambda^2)}, \{i, 1, \text{dim}\} \right];
\end{aligned}$$

$$\text{ProPR133} = \text{Table} \left[\frac{2\Delta\lambda e\text{PR13}[[2]]}{\pi\Delta\lambda(4(\text{De}+\lambda_{\text{exp}}[[i]])-\lambda_{\text{FRP13}}[[2]])^2+\Delta\lambda^2}, \{i, 1, \text{dim}\} \right];$$

$$\text{ProPR135} = \text{Table} \left[\frac{2\Delta\lambda e\text{PR13}[[3]]}{\pi\Delta\lambda(4(\text{De}+\lambda_{\text{exp}}[[i]])-\lambda_{\text{FRP13}}[[3]])^2+\Delta\lambda^2}, \{i, 1, \text{dim}\} \right];$$

$$\text{ProPR137} = \text{Table} \left[\frac{2\Delta\lambda e\text{PR13}[[5]]}{\pi\Delta\lambda(4(\text{De}+\lambda_{\text{exp}}[[i]])-\lambda_{\text{FRP13}}[[5]])^2+\Delta\lambda^2}, \{i, 1, \text{dim}\} \right];$$

$$\text{IPR13} = \text{ProPR131} + \text{ProPR133} + \text{ProPR135} + \text{ProPR137};$$

“PRQ21: RQ21: kup=3,5..., jup=3,5,....,klow=2,4,6..... jlow=3,5....”;

$$\text{PRQ21} = \text{Table}[\text{BLF}[2i + 1, 2i + 1]\text{SRQ21}[[i]], \{i, 1, 20\}];$$

$$\text{eRQ21} = \text{Table} \left[\frac{\text{PRQ21}[[i]]}{\lambda_{\text{FRQ21}}[[i]]^3}, \{i, 1, 12\} \right];$$

$$\text{ProRQ213} = \text{Table} \left[\frac{2\Delta\lambda e\text{RQ21}[[1]]}{\pi\Delta\lambda(4(\text{De}+\lambda_{\text{exp}}[[i]])-\lambda_{\text{FRQ21}}[[1]])^2+\Delta\lambda^2}, \{i, 1, \text{dim}\} \right];$$

$$\text{ProRQ215} = \text{Table} \left[\frac{2\Delta\lambda e\text{RQ21}[[2]]}{\pi\Delta\lambda(4(\text{De}+\lambda_{\text{exp}}[[i]])-\lambda_{\text{FRQ21}}[[2]])^2+\Delta\lambda^2}, \{i, 1, \text{dim}\} \right];$$

$$\text{ProRQ217} = \text{Table} \left[\frac{2\Delta\lambda e\text{RQ21}[[3]]}{\pi\Delta\lambda(4(\text{De}+\lambda_{\text{exp}}[[i]])-\lambda_{\text{FRQ21}}[[3]])^2+\Delta\lambda^2}, \{i, 1, \text{dim}\} \right];$$

$$\text{ProRQ219} = \text{Table} \left[\frac{2\Delta\lambda e\text{RQ21}[[4]]}{\pi\Delta\lambda(4(\text{De}+\lambda_{\text{exp}}[[i]])-\lambda_{\text{FRQ21}}[[4]])^2+\Delta\lambda^2}, \{i, 1, \text{dim}\} \right];$$

$$\text{IRQ21} = \text{ProRQ213} + \text{ProRQ215} + \text{ProRQ217}; +\text{ProRQ219};$$

“PRP31: RP31: kup=3,5..., jup=2,4,6...,klow=2,4,6..... jlow=3,5....”;

$$\text{PRP31} = \text{Table}[\text{BLF}[2i + 1, 2i]\text{SRP31}[[i]], \{i, 1, 20\}];$$

$$\text{eRP31} = \text{Table} \left[\frac{\text{PRP31}[[i]]}{\lambda_{\text{FRP31}}[[i]]^3}, \{i, 1, 12\} \right];$$

$$\text{ProRP313} = \text{Table} \left[\frac{2\Delta\lambda e\text{RP31}[[1]]}{\pi\Delta\lambda(4(\text{De}+\lambda_{\text{exp}}[[i]])-\lambda_{\text{FRP31}}[[1]])^2+\Delta\lambda^2}, \{i, 1, \text{dim}\} \right];$$

$$\text{ProRP315} = \text{Table} \left[\frac{2\Delta\lambda e\text{RP31}[[2]]}{\pi\Delta\lambda(4(\text{De}+\lambda_{\text{exp}}[[i]])-\lambda_{\text{FRP31}}[[2]])^2+\Delta\lambda^2}, \{i, 1, \text{dim}\} \right];$$

$$\text{ProRP317} = \text{Table} \left[\frac{2\Delta\lambda e\text{RP31}[[3]]}{\pi\Delta\lambda(4(\text{De}+\lambda_{\text{exp}}[[i]])-\lambda_{\text{FRP31}}[[3]])^2+\Delta\lambda^2}, \{i, 1, \text{dim}\} \right];$$

$$\text{ProRP319} = \text{Table} \left[\frac{2\Delta\lambda e\text{RP31}[[4]]}{\pi\Delta\lambda(4(\text{De}+\lambda_{\text{exp}}[[i]])-\lambda_{\text{FRP31}}[[4]])^2+\Delta\lambda^2}, \{i, 1, \text{dim}\} \right];$$

$$\text{IRP31} = \text{ProRP313} + \text{ProRP315} + \text{ProRP317} + \text{ProRP319};$$

“PRQ32: RQ32: kup=3,5..., jup=2,4,6...,klow=2,4,6..... jlow=2,4,6....”;

$$\text{PRQ32} = \text{Table}[\text{BLF}[2i + 1, 2i]\text{SRQ32}[[i]], \{i, 1, 20\}];$$

$$\text{eRQ32} = \text{Table} \left[\frac{\text{PRQ32}[[i]]}{\lambda_{\text{FRQ32}}[[i]]^3}, \{i, 1, 12\} \right];$$

$$\text{ProRQ323} = \text{Table} \left[\frac{2\Delta\lambda e\text{RQ32}[[1]]}{\pi\Delta\lambda(4(\text{De}+\lambda_{\text{exp}}[[i]])-\lambda_{\text{FRQ32}}[[1]])^2+\Delta\lambda^2}, \{i, 1, \text{dim}\} \right];$$

$$\text{ProRQ325} = \text{Table} \left[\frac{2\Delta\lambda e\text{RQ32}[[2]]}{\pi\Delta\lambda(4(\text{De}+\lambda_{\text{exp}}[[i]])-\lambda_{\text{FRQ32}}[[2]])^2+\Delta\lambda^2}, \{i, 1, \text{dim}\} \right];$$

$$\text{ProRQ327} = \text{Table} \left[\frac{2\Delta\lambda e\text{RQ32}[[3]]}{\pi\Delta\lambda(4(\text{De}+\lambda_{\text{exp}}[[i]])-\lambda_{\text{FRQ32}}[[3]])^2+\Delta\lambda^2}, \{i, 1, \text{dim}\} \right];$$

$$\text{ProRQ329} = \text{Table} \left[\frac{2\Delta\lambda e\text{RQ32}[[4]]}{\pi\Delta\lambda(4(\text{De}+\lambda_{\text{exp}}[[i]])-\lambda_{\text{FRQ32}}[[4]])^2+\Delta\lambda^2}, \{i, 1, \text{dim}\} \right];$$

```

IRQ32 = ProRQ323 + ProRQ325 + ProRQ327 + ProRQ329;
IT = IP1 + IP2 + IP3 + IPQ12 + IPQ23 + IPR13 + IQ1 + IQ2 + IQ3+
IQP21 + IQP32 + IQR12 + IQR23 + IR1 + IR2 + IR3 + IRP31 + IRQ21 + IRQ32;
M1 = Max[IT];
IE1 = Table [ { λexp[[i]],  $\frac{IT[[i]]}{M1}$  } , {i, 1, dim} ] ;
I1 = Interpolation[IE1];
M2 = 0.6;
IE2 = Table [ { λexp[[i]],  $\frac{I_{experimental}[[i]]}{MOM2}$  } , {i, 1, dim} ] ;
C3 = Plot [ Evaluate [  $\frac{I0[x]}{MOM2}$ , {x, 630, 654} ] ,
PlotRange → {-0.9, 2}, PlotStyle → {RGBColor[0, 0, 0], Thickness[0.002]};
C4 = Plot[Evaluate[I1[x], {x, 630, 654}],
PlotRange → {-0.9, 1.1}, PlotStyle → {RGBColor[1, 0, 0], Thickness[0.002]};
C5 = Plot [ Evaluate [  $\frac{I0[x]}{MOM2}$  - I1[x], {x, 630, 654} ] ,
PlotRange → {-0.9, 2}, PlotStyle → {RGBColor[0, 0, 1], Thickness[0.002]};
Show[C3, C4, C5]
ClearAll[C3, C4, C5]

```

Appendix G

High-Voltage monitor

In order to measure the current and voltage through our setup, the device shown in Fig. G.1 was designed and constructed by Mr. Nick Dorsey in May 2011.

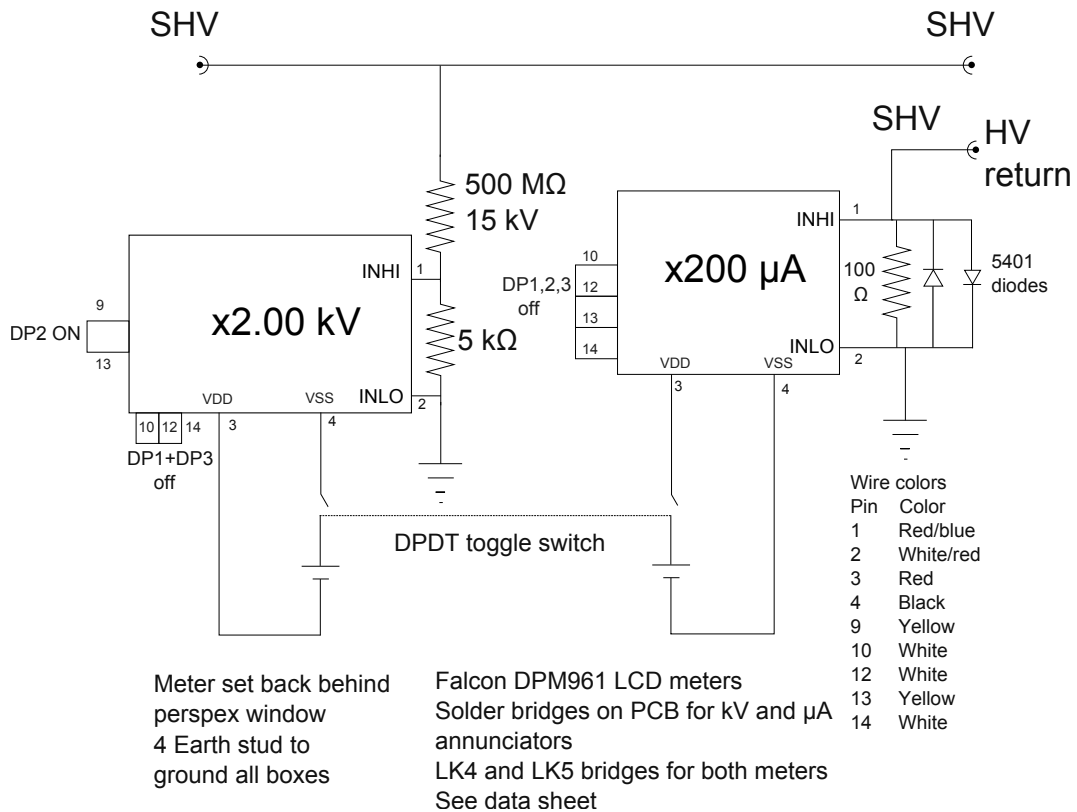


Figure G.1: Electric diagram of the HV monitor designed by Nick Dorsey.

During operation of the device it was suspected that the instrument might need a slight recalibration. For that purpose, a shunt resistor (1 MΩ) was added to the return as shown in Fig. G.2. The result of the recalibration is a linear relation between the current measured by the HV monitor and the reading of the multimeter (assumed to be correctly calibrated). It was found the following relationship between said magnitudes:

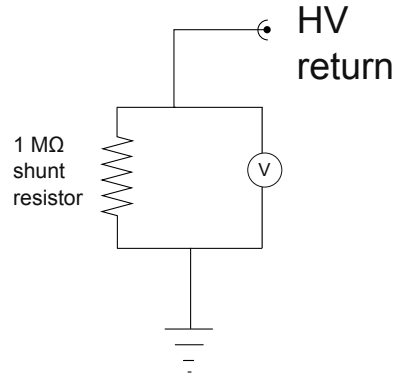


Figure G.2: Additional shunt resistor and voltmeter to measure the current in our setup.

$$I_{\text{mult}} = mI_{\text{HV mon}} + b, \quad (\text{G.1})$$

$$m = 0.9135 \pm 2.46 \times 10^{-4} \quad (\text{G.2})$$

$$b = 0.25 \pm 0.040 \mu\text{A}. \quad (\text{G.3})$$

The currents reported in this work correspond to the corrected, recalibrated value.

Appendix H

Tip after the experiments

The purpose of this section is to show the appearance of the tungsten tip after a given set of experiments.

The photos shown in this Appendix were recorded by Mumin Koc using the focused ion beam (FIB) [37] available to the members of the CMP group.

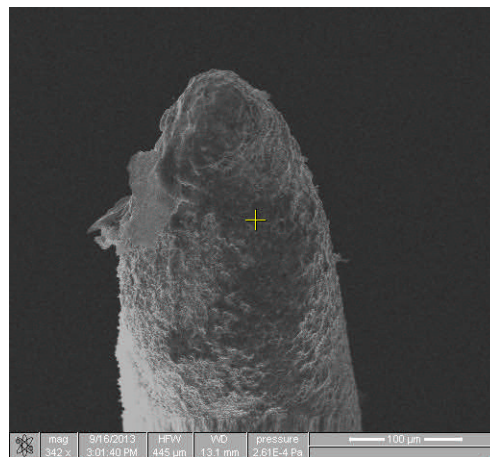


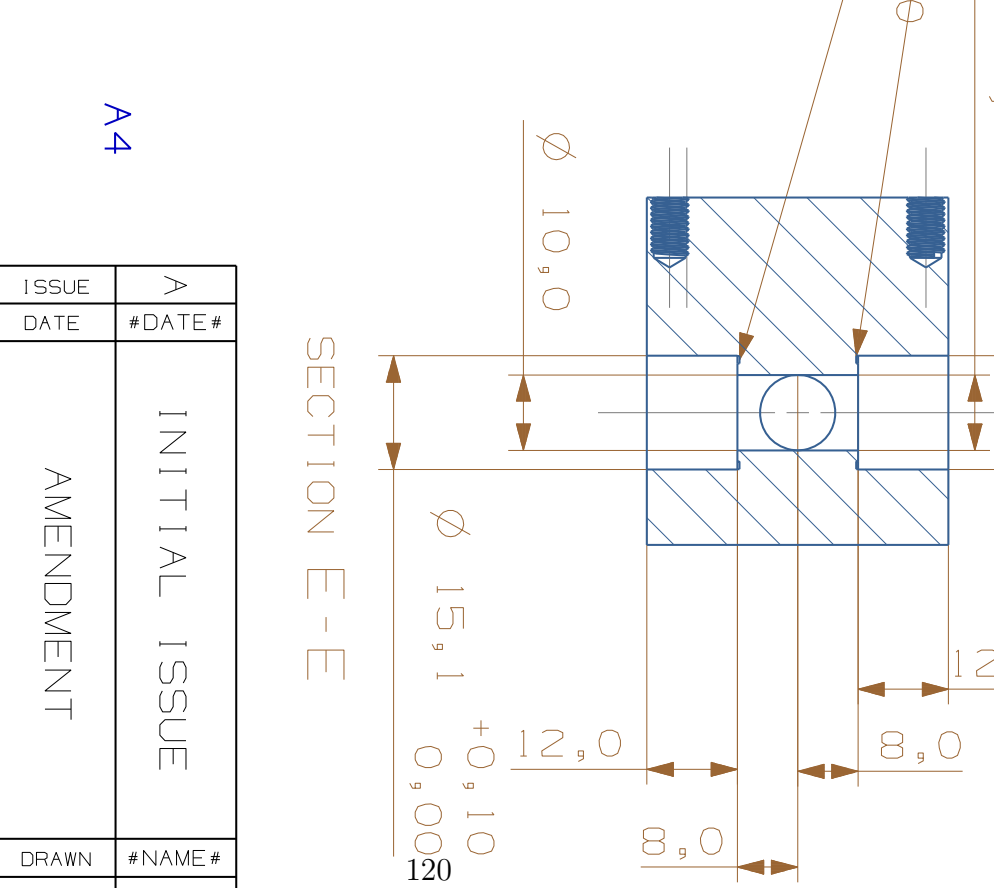
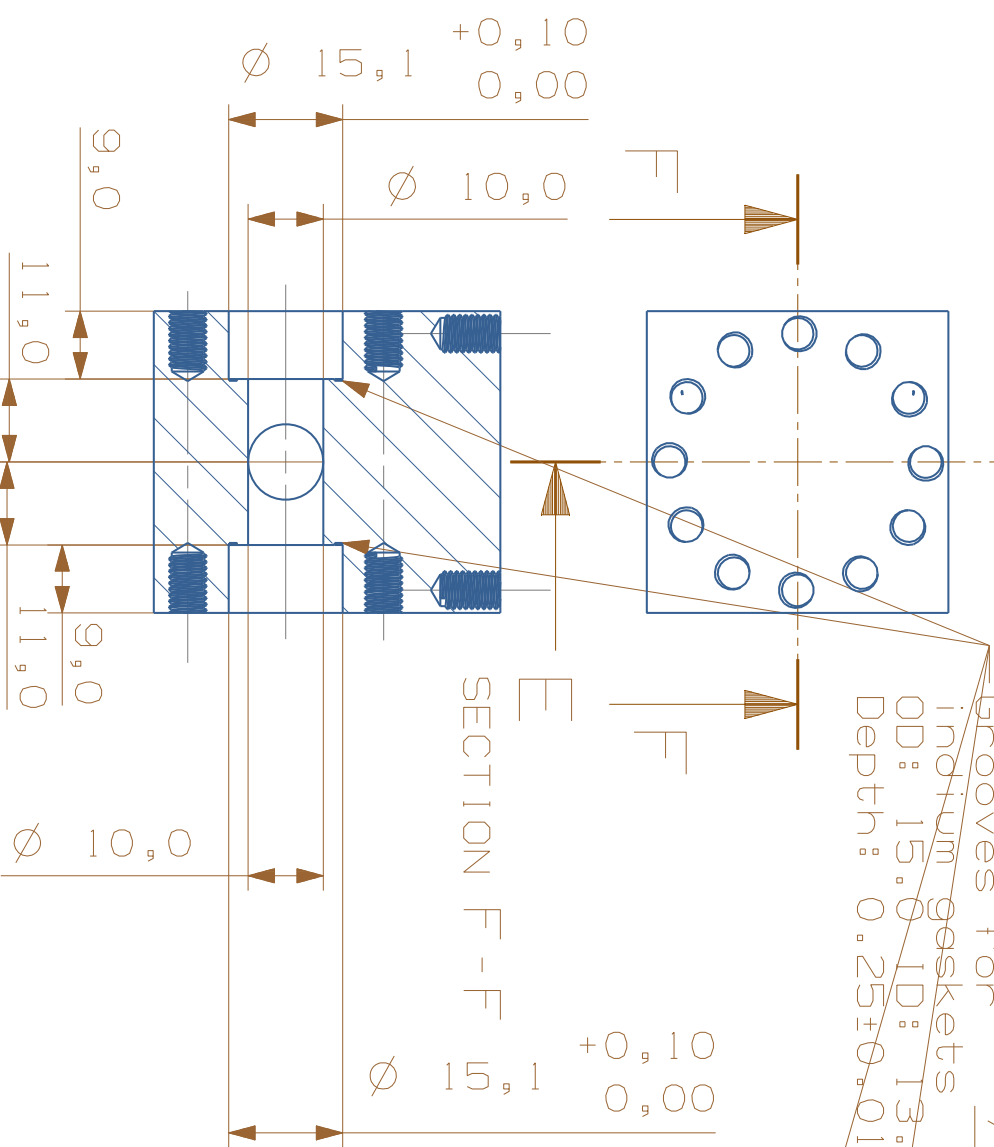
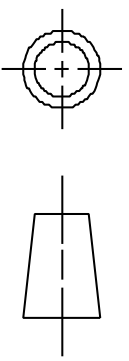
Figure H.1: Top view of the tungsten tip recorded with the FIB technique.

Appendix I

NX designs and technical drawings

This section provides technical drawings for the most relevant parts of our design. The assembly procedure of the device has been explained in Section 3.14. Each of the pieces shown in this Appendix have been designed by us and built by the Mechanical Workshop of the Physics Department at the University of Leicester (except for the Macor pieces, which were outsourced to an external company). The names given in each diagram correspond to the names they were referred to in the body of the text of this work and are self-explanatory insofar as possible.

The pieces given here were designed and modelled using CAD software Siemens NX 6.0.5.3. The names given in the technical drawings also correspond to the filename they adopted in the corresponding NX model files.



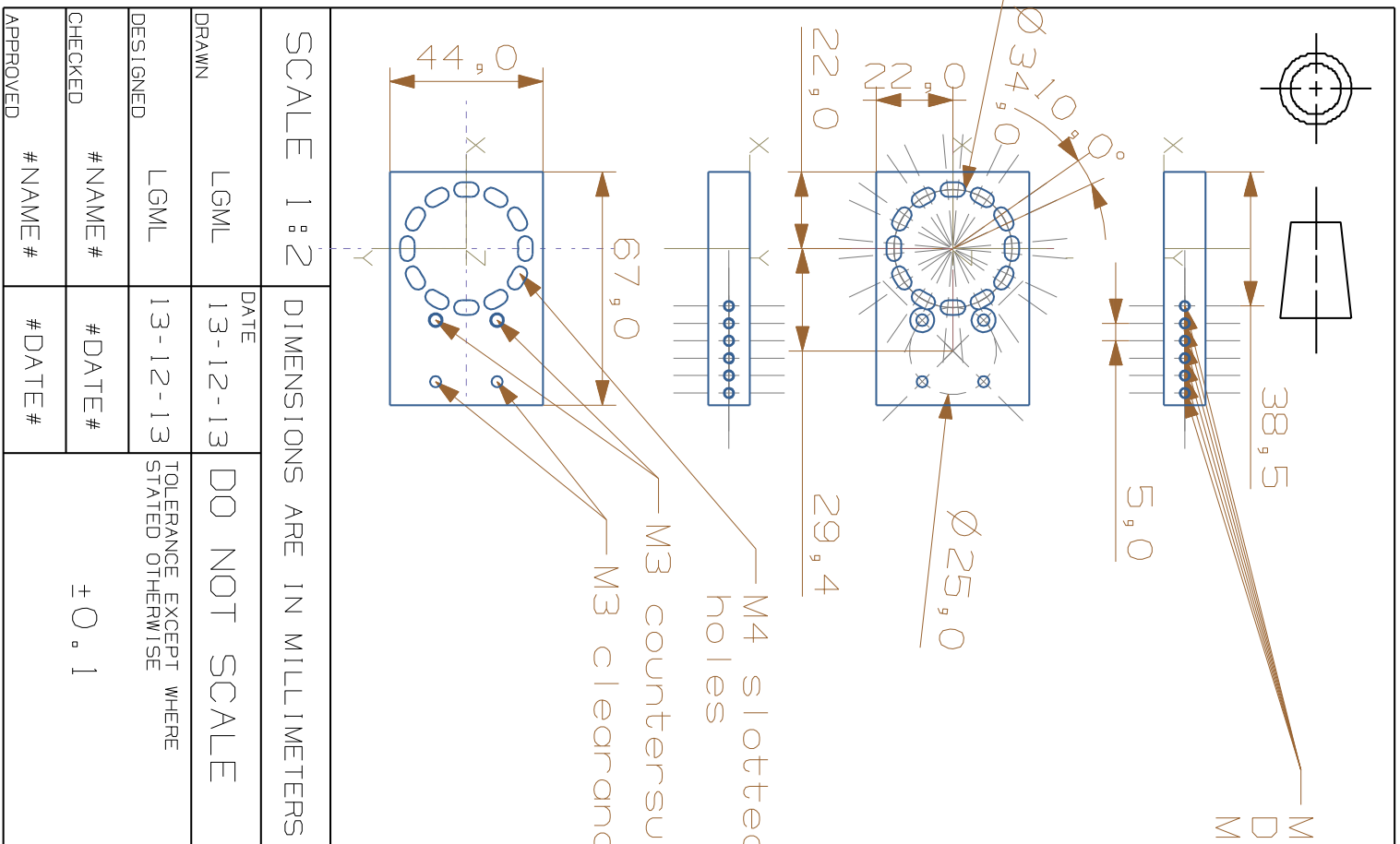
A4

SCALE 1:1	DIMENSIONS ARE IN MILLIMETERS	
DRAWN LGML	DATE 13-12-13	DO NOT SCALE
DESIGNED LGML	13-12-13	TOLERANCE EXCEPT WHERE STATED OTHERWISE
CHECKED #NAME#	#DATE#	±0.1
APPROVED #NAME#	#DATE#	

SHEET 2 OF 2	
USED ON	#USED ON#
DRAWING TYPE	#DRAWING TYPE#
MATERIAL OFHC	
FINISH Gold-plated	

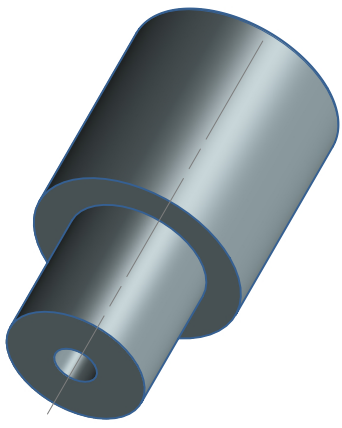
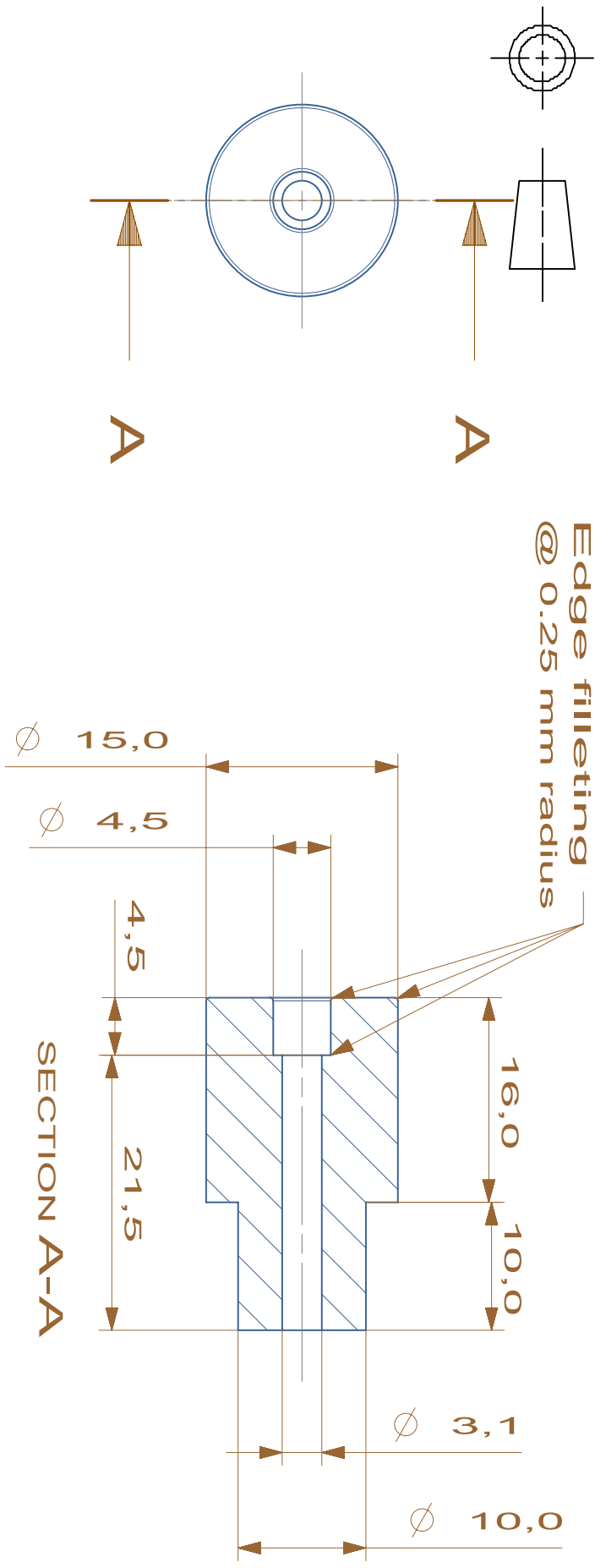
ISSUE A	#DATE#	INITIAL ISSUE	DRAWN #NAME#
DATE		AMENDMENT	APPROVED #NAME#
PROJECT CCD		TITLE cell	
DRG. NO. #DRG NO#		UNIVERSITY OF LEICESTER	





SCALE 1:2	DIMENSIONS ARE IN MILLIMETERS	SHEET 1 OF 1
DRAWN LGML	DATE 13-12-13	USED ON #
DESIGNED LGML	13-12-13	DRAWING TYPE #
CHECKED #NAME #	#DATE #	MATERIAL OFHC
APPROVED #NAME #	#DATE #	FINISH Gold-plated
TOLERANCE EXCEPT WHERE STATED OTHERWISE ±0.1		

University of Leicester PROJECT CCD		TITLE eccentric-concentric2 DRG. NO. # DRG NO#	
ISSUE A	DATE #DATE #	INITIAL	ISSUE
AMENDMENT			
DRAWN	#NAME #		
APPROVED	#NAME #		



SCALE 1:1		DIMENSIONS ARE IN MILLIMETERS	
DRAWN	#NAME#	DATE	#DATE#
DESIGNED	#NAME#	DO NOT SCALE	
CHECKED	#NAME#	TOLERANCE EXCEPT WHERE STATED OTHERWISE	
APPROVED	#NAME#	± 0.2	

SHEET 1 OF 1		A4	
USED ON	#USED ON#	DRAWING TYPE	#DRAWING TYPE#
MATERIAL	#MATERIAL#	FINISH	#FINISH#

ISSUE	A	INITIAL ISSUE	
DATE	#DATE#	AMENDMENT	
DRAWN	#NAME#		
APPROVED	#NAME#		

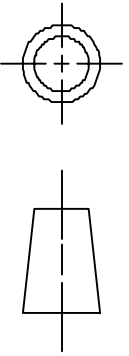


University of Leicester

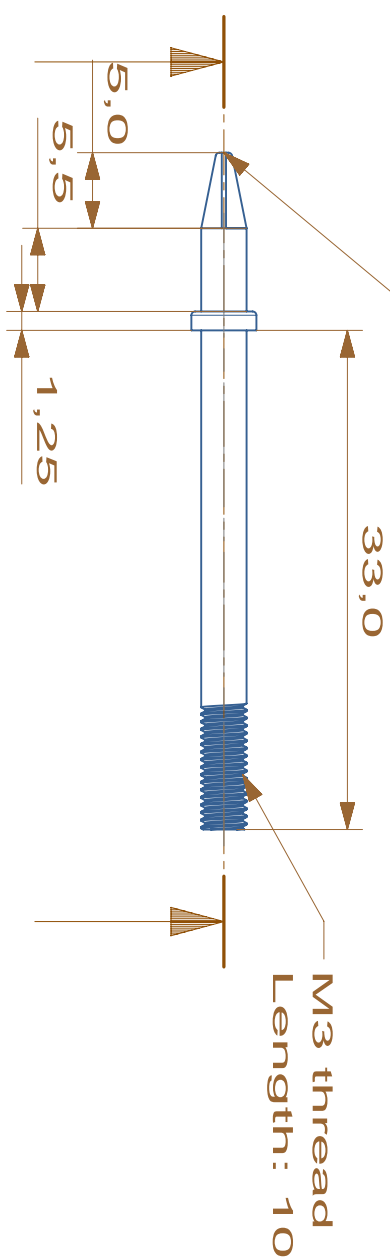
#PROJECT NAME#

#PART NAME#

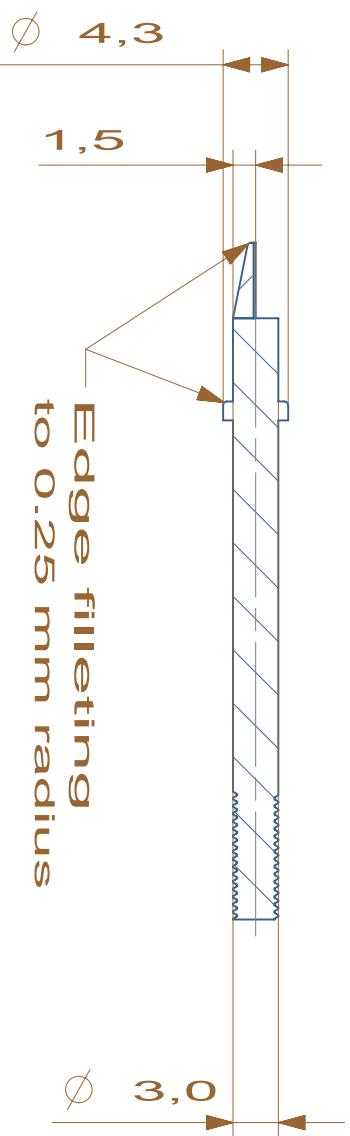
macor



0.28 mm diameter channel



B SECTION B-B B



Edge filletting to 0.25 mm radius

A4



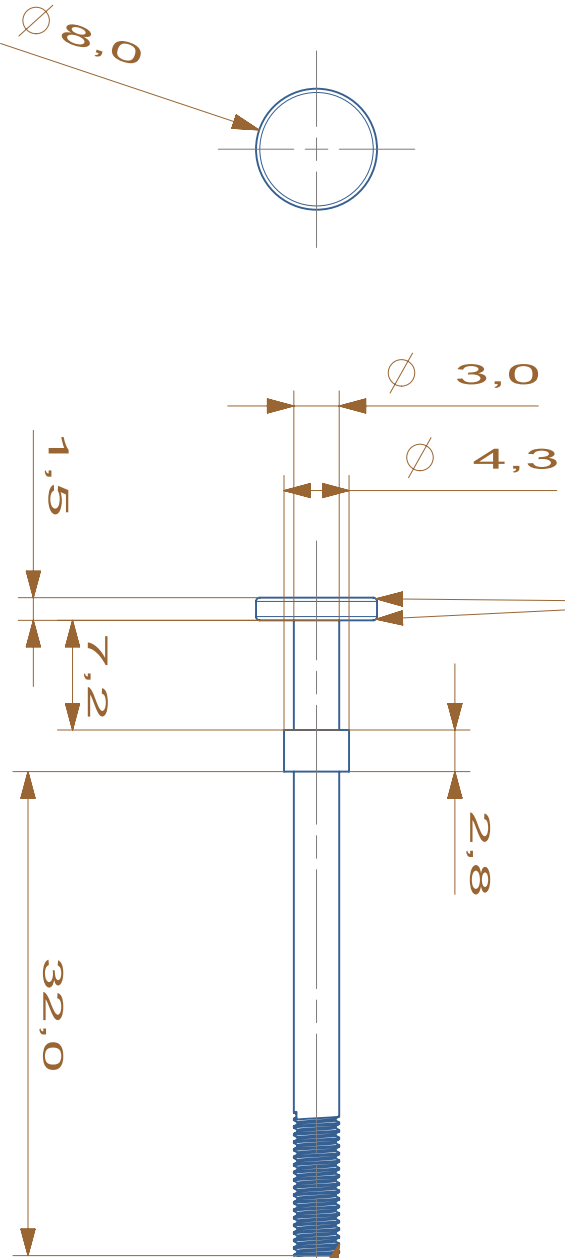
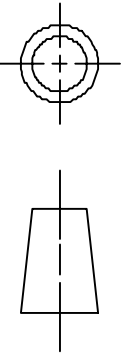
SCALE 1:1		DIMENSIONS ARE IN MILLIMETERS		SHEET 1 OF 1	
DRAWN	#NAME#	DATE	#DATE#	USED ON	#USED ON#
DESIGNED	#NAME#	#DATE#	#DATE#	DRAWING TYPE	#DRAWING TYPE#
CHECKED	#NAME#	#DATE#	#DATE#	MATERIAL	#MATERIAL#
APPROVED	#NAME#	#DATE#	#DATE#	FINISH	#FINISH#
		DO NOT SCALE			
		TOLERANCE EXCEPT WHERE STATED OTHERWISE			
		± 0.1			

ISSUE	A	DATE	#DATE#	INITIAL ISSUE	DRAWN	#NAME#
					APPROVED	#NAME#
				AMENDMENT		



University of Leicester

PROJECT	#PROJECT NAME#
TITLE	tip_electrode_bearer
DRG. NO.	#DRG NO#



M3 thread
Length: 10

A4

SCALE 1:1		DIMENSIONS ARE IN MILLIMETERS		SHEET 1 OF 1	
DRAWN	#NAME#	DATE	#DATE#	DO NOT SCALE	USED ON
DESIGNED	#NAME#	#DATE#	#DATE#		TOLERANCE EXCEPT WHERE STATED OTHERWISE
CHECKED	#NAME#	#DATE#	#DATE#	± 0.1	DRAWING TYPE
APPROVED	#NAME#	#DATE#	#DATE#		MATERIAL
			FINISH		
			#FINISH#		

ISSUE	A	DATE	#DATE#	INITIAL ISSUE	DRAWN	#NAME#
				AMENDMENT	APPROVED	#NAME#

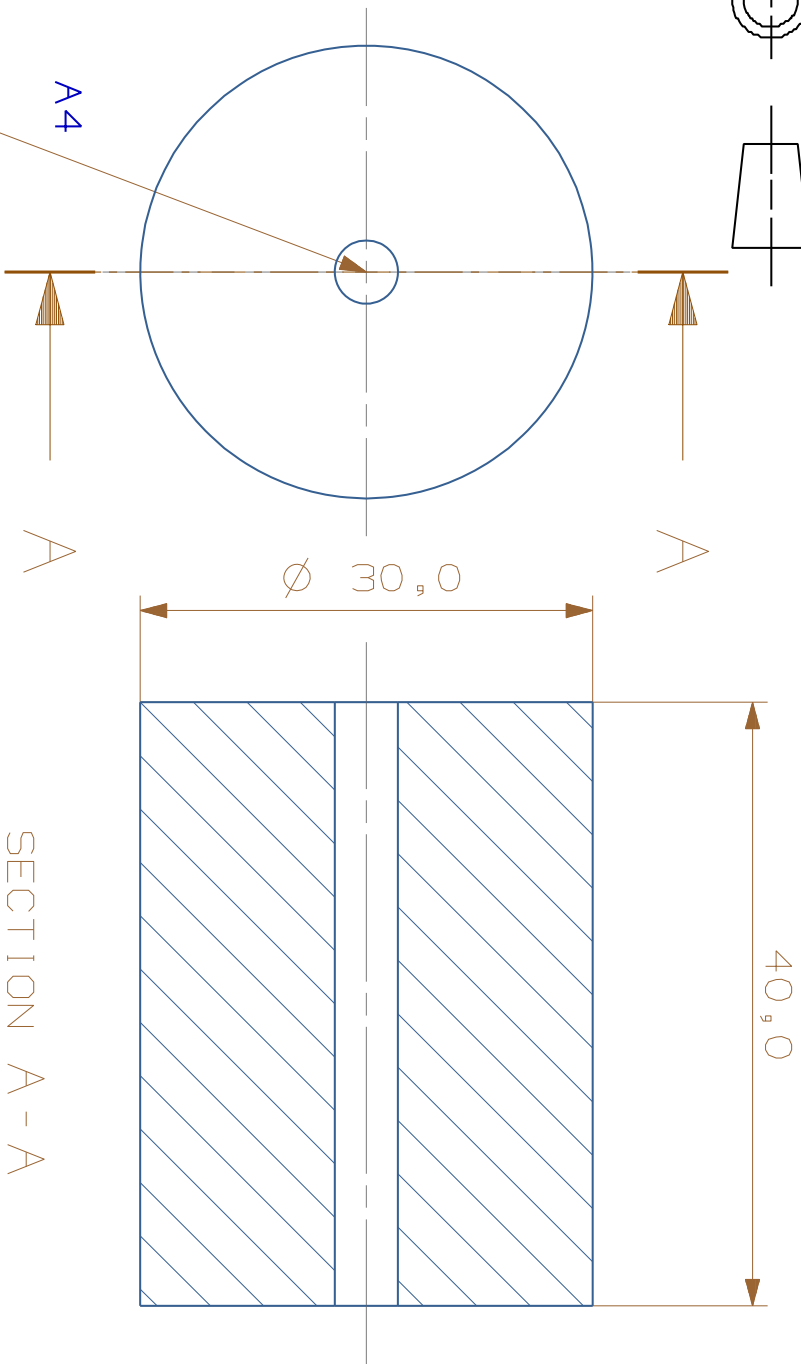
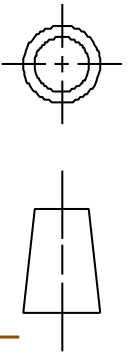


University of Leicester

#PROJECT NAME#

flat_electrode

#DRG NO#



SECTION A - A

Solder a helix of 1/16" SS pipe as per 3D model with at least 15 turns



SCALE 2:1	DIMENSIONS ARE IN MILLIMETERS	
DRAWN LGML	DATE 13-12-13	DO NOT SCALE
DESIGNED LGML	13-12-13	TOLERANCE EXCEPT WHERE STATED OTHERWISE
CHECKED #NAME#	#DATE#	±0.1
APPROVED #NAME#	#DATE#	

SHEET 1 OF 1	
USED ON	#USED ON#
DRAWING TYPE	#DRAWING TYPE#
MATERIAL	REGULAR COPPER
FINISH	#FINISH#

ISSUE A	#DATE#	INITIAL	ISSUE
DATE		AMENDMENT	
DRAWN	#NAME#		
APPROVED	#NAME#		

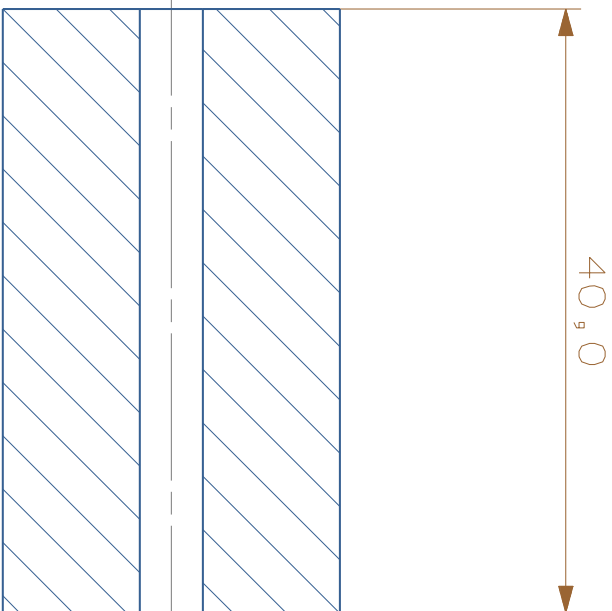
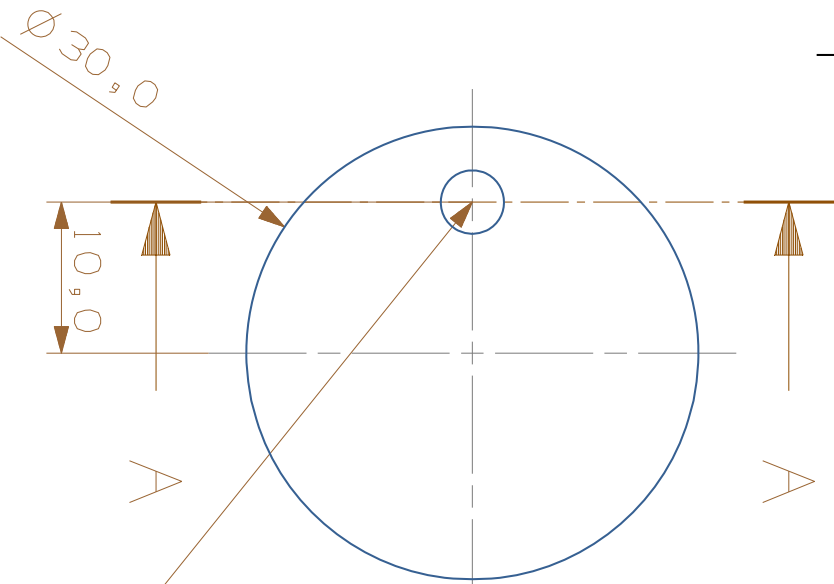
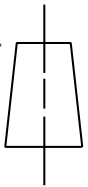
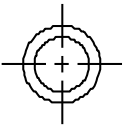


University of Leicester

CCD

hs_point_1

#DRG NO#

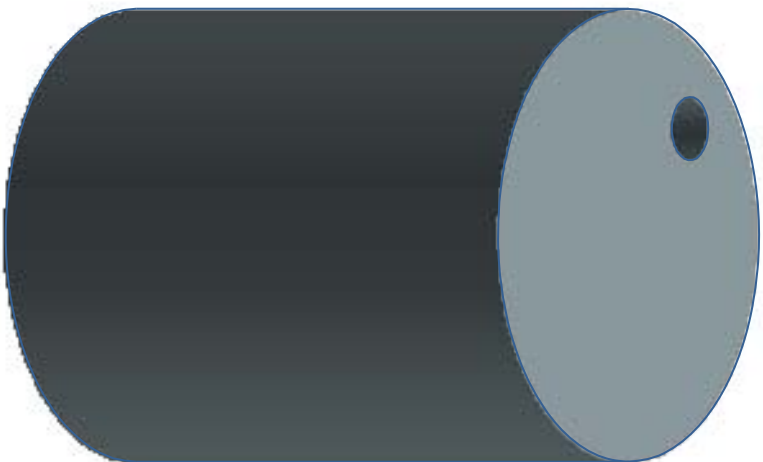


SECTION A - A

Clearance for M4

Solder a helix of 1/16" SS pipe as per 3D model with at least 15 turns

A4



SCALE 2:1		DIMENSIONS ARE IN MILLIMETERS	
DRAWN	LGML	DATE	13-12-13
DESIGNED	LGML	DATE	13-12-13
CHECKED	#NAME #	#DATE #	
APPROVED	#NAME #	#DATE #	
DO NOT SCALE		TOLERANCE EXCEPT WHERE STATED OTHERWISE	
± 0.1			

SHEET 1 OF 1	
USED ON	#USED ON#
DRAWING TYPE	#DRAWING TYPE#
MATERIAL	REGULAR COPPER
FINISH	#FINISH#

ISSUE	A	INITIAL	ISSUE
DATE	#DATE #	AMENDMENT	
UNIVERSITY OF LEICESTER		CCD	
PROJECT		hs_point_2	
TITLE		#DRG NO#	
DRG. NO.			
DRAWN	#NAME #	APPROVED	#NAME #

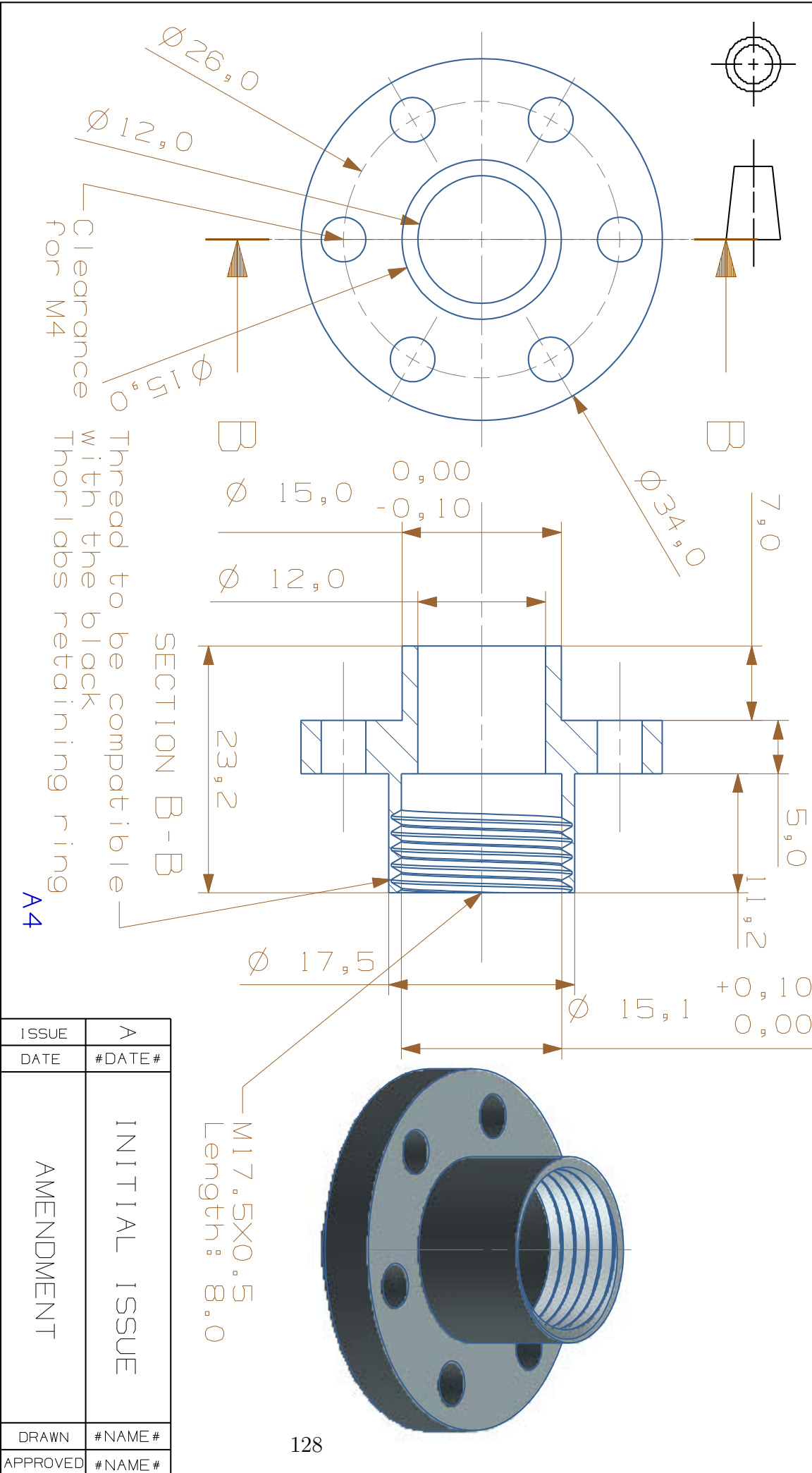


University of Leicester

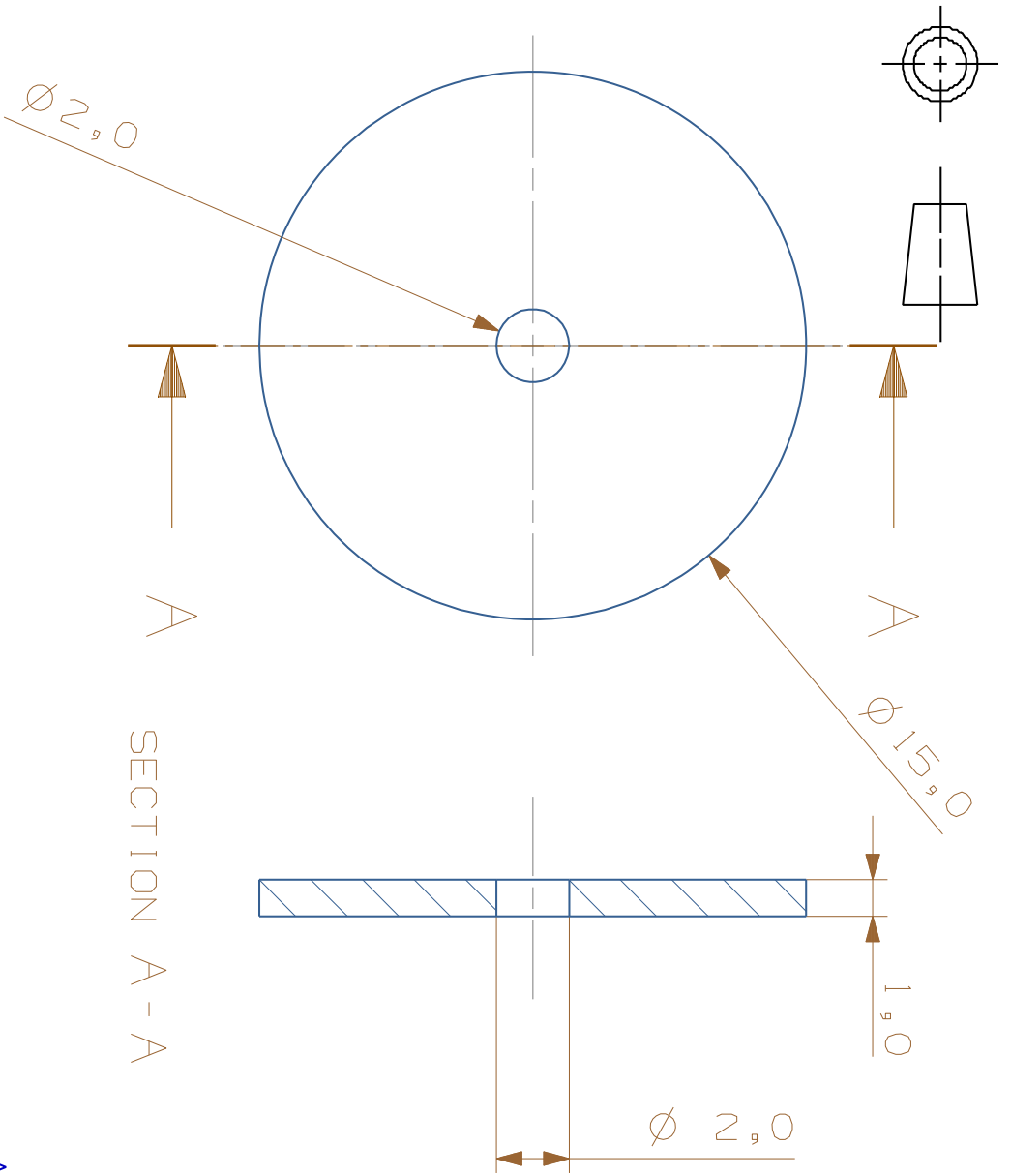
SCALE 2:1	DIMENSIONS ARE IN MILLIMETERS	
DRAWN LGML	DATE 13-12-13	DO NOT SCALE
DESIGNED LGML	13-12-13	TOLERANCE EXCEPT WHERE STATED OTHERWISE
CHECKED #NAME#	#DATE#	±0.1
APPROVED #NAME#	#DATE#	

SHEET 1 OF 1	
USED ON	#USED ON#
DRAWING TYPE	#DRAWING TYPE#
MATERIAL SS	
FINISH	#FINISH#

 University of Leicester	
PROJECT	CCD
TITLE	opt ic_mount_50_mm
DRG. NO.	#DRG NO#



ISSUE	A
DATE	#DATE#
	INITIAL ISSUE
	AMENDMENT
DRAWN	#NAME#
APPROVED	#NAME#



SECTION A - A

A4

SCALE 5 : 1 DIMENSIONS ARE IN MILLIMETERS

SHEET 1 OF 1

UNIVERSITY OF LEICESTER
University of Leicester

DRAWN	LGML	DATE	13-12-13	DO NOT SCALE
-------	------	------	----------	--------------

USED ON	#USED ON#
---------	-----------

PROJECT	CCD
---------	-----

DESIGNED	LGML	13-12-13	TOLERANCE EXCEPT WHERE STATED OTHERWISE
----------	------	----------	---

DRAWING TYPE	#DRAWING TYPE#
--------------	----------------

TITLE	pinhole
-------	---------

CHECKED	#NAME#	#DATE#	$\pm 0,1$
---------	--------	--------	-----------

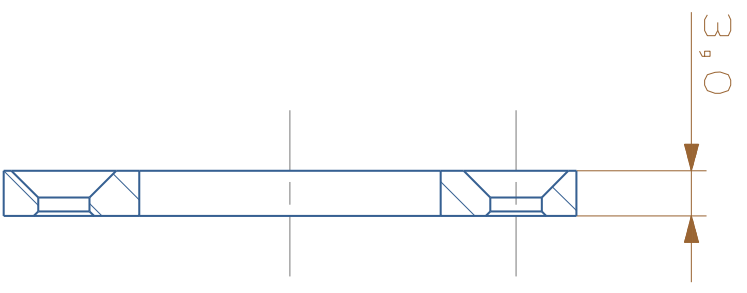
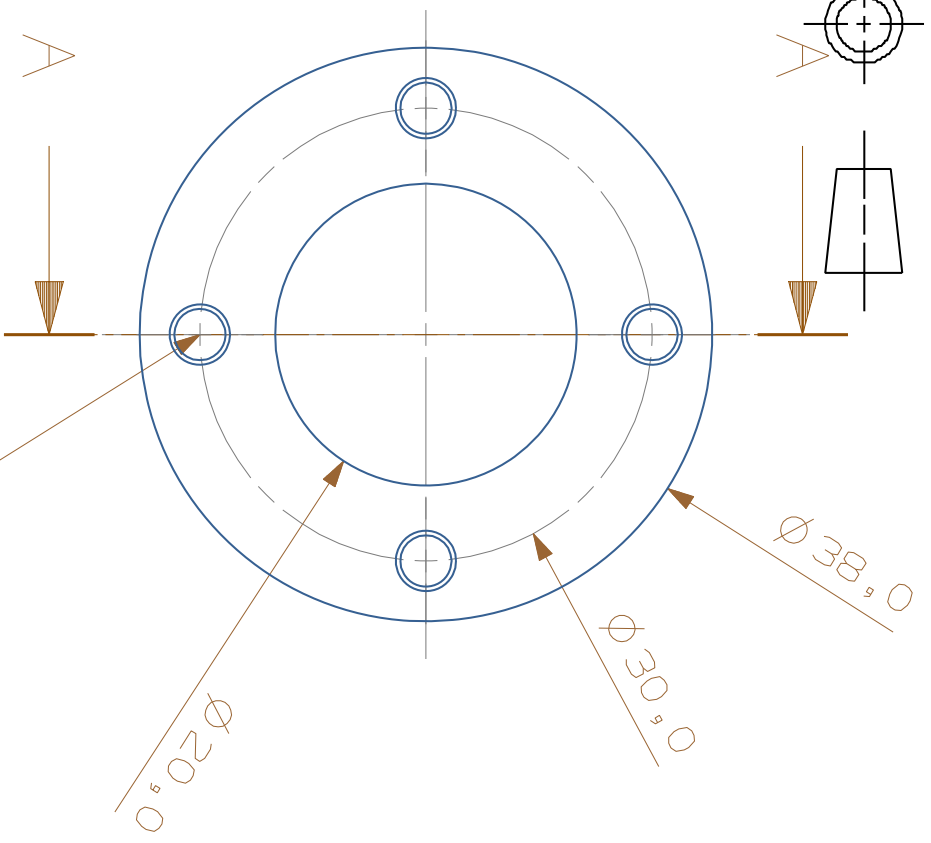
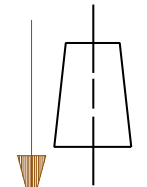
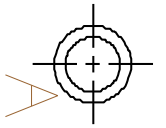
MATERIAL	SS, copper or plastic
----------	-----------------------

DRG. NO.	#DRG NO#
----------	----------

APPROVED	#NAME#	#DATE#
----------	--------	--------

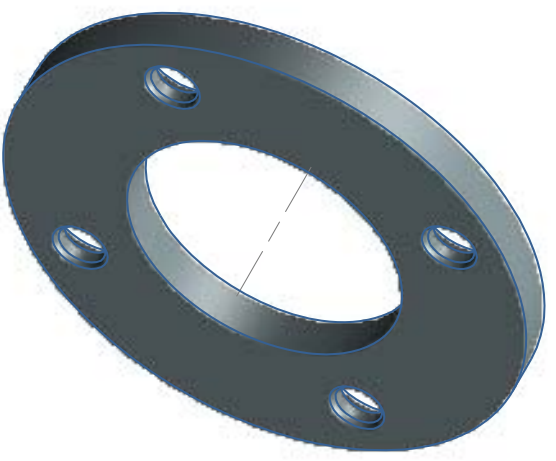
FINISH	#FINISH#
--------	----------

ISSUE	A	INITIAL	ISSUE
DATE	#DATE#	AMENDMENT	
DRAWN	#NAME#		
APPROVED	#NAME#		



SECTION A - A

A4
Clearance for M3
countersunk screws



SCALE 2 : 1		DIMENSIONS ARE IN MILLIMETERS	
DRAWN	LGML	DATE	29-11-13
DESIGNED	LGML	DATE	29-11-13
CHECKED	#NAME #	#DATE #	
APPROVED	#NAME #	#DATE #	
DO NOT SCALE		TOLERANCE EXCEPT WHERE STATED OTHERWISE	
± 0 . 1			

SHEET 1 OF 1	
USED ON	#USED ON#
DRAWING TYPE	#DRAWING TYPE#
MATERIAL	SS
FINISH	#FINISH#

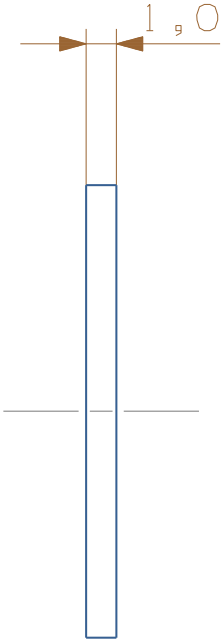
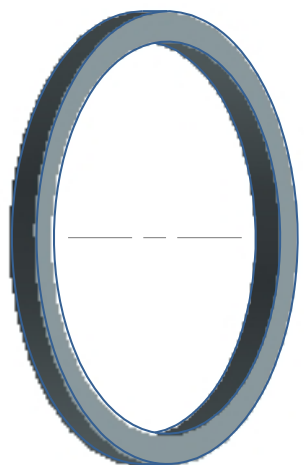
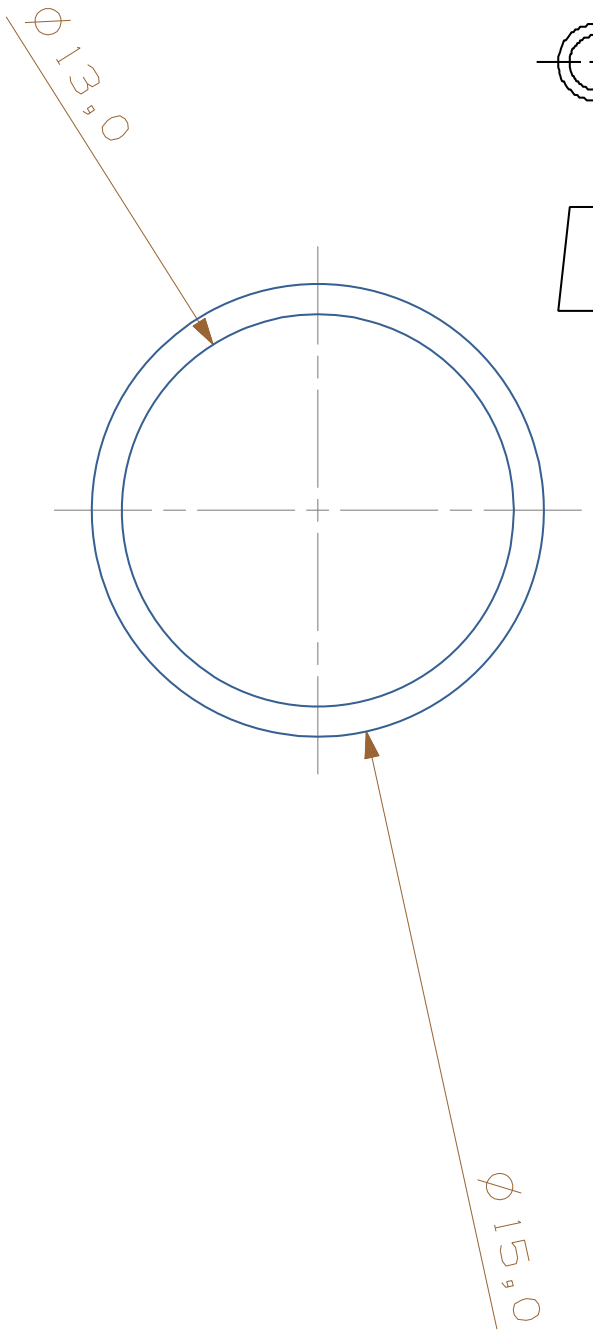
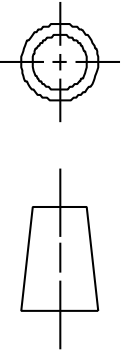
ISSUE	A	DATE	#DATE #
	INITIAL ISSUE		
	AMENDMENT		
DRAWN	#NAME #		
APPROVED	#NAME #		



PROJECT
CCD

TITLE
ring

DRG. NO.
DRG NO



30 OFF

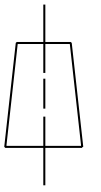
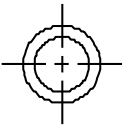
A4

SCALE 4 : 1	DIMENSIONS ARE IN MILLIMETERS	
DRAWN LGML	DATE 13-12-13	DO NOT SCALE
DESIGNED LGML	13-12-13	TOLERANCE EXCEPT WHERE STATED OTHERWISE
CHECKED # NAME #	# DATE #	± 0.1
APPROVED # NAME #	# DATE #	

SHEET 1 OF 1	
USED ON	# USED ON #
DRAWING TYPE	# DRAWING TYPE #
MATERIAL	Peek
FINISH	# FINISH #

ISSUE A	# DATE #	INITIAL ISSUE	DRAWN # NAME #
DATE		AMENDMENT	APPROVED # NAME #
PROJECT		CCD	
TITLE		Spacer	
DRG. NO.		# DRG NO #	

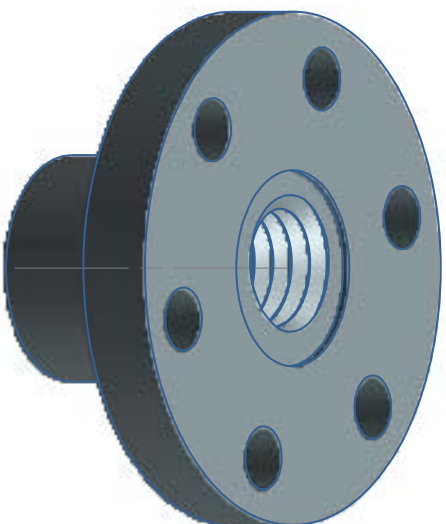
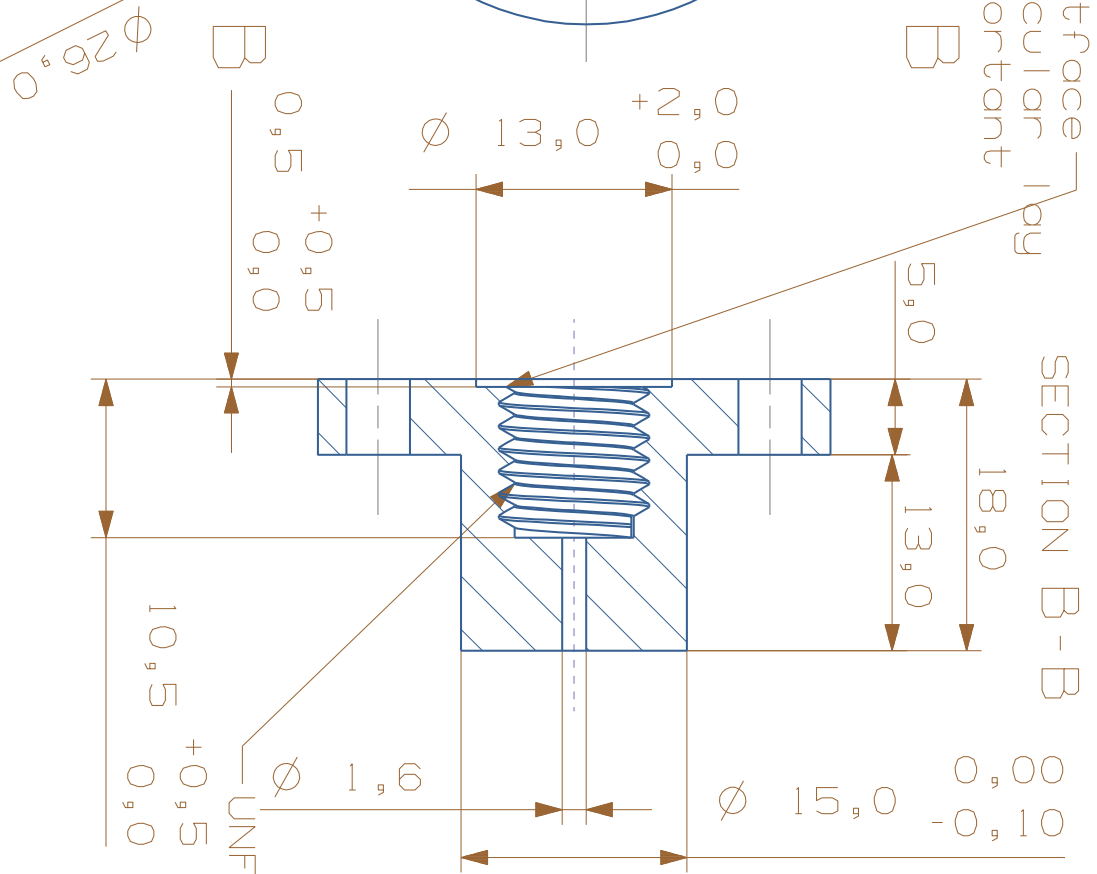
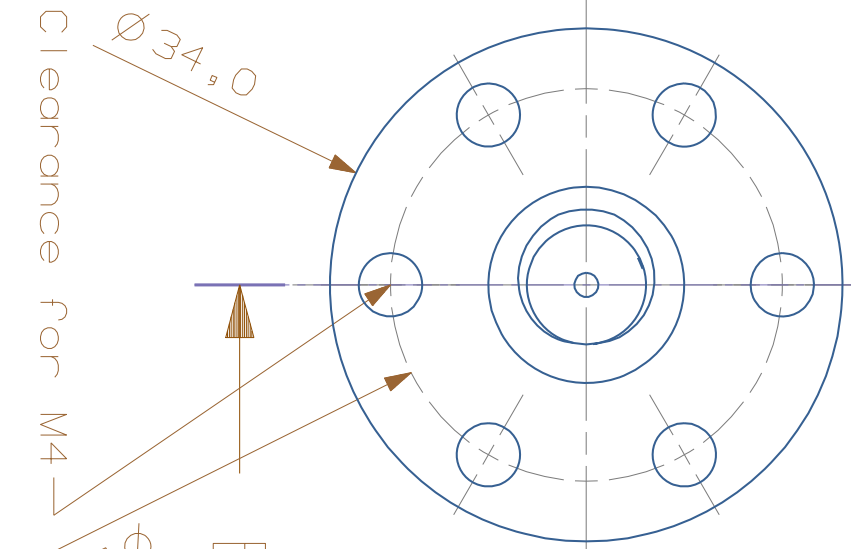




Spotface
Circular
important

B

SECTION B - B



134

SCALE 1 : 1	DIMENSIONS ARE IN MILLIMETERS	
DRAWN LGML	DATE 13-12-13	DO NOT SCALE
DESIGNED LGML	13-12-13	TOLERANCE EXCEPT WHERE STATED OTHERWISE
CHECKED # NAME #	# DATE #	± 0.1
APPROVED # NAME #	# DATE #	

SHEET 1 OF 1	
USED ON	# USED ON #
DRAWING TYPE	# DRAWING TYPE #
MATERIAL SS	
FINISH	# FINISH #

ISSUE A	# DATE #	INITIAL ISSUE
DATE		AMENDMENT
UNF-5/16''-24		
DRAWN	# NAME #	
APPROVED	# NAME #	



University of
Leicester

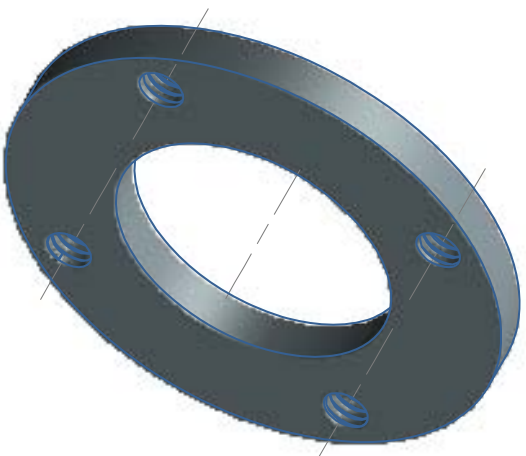
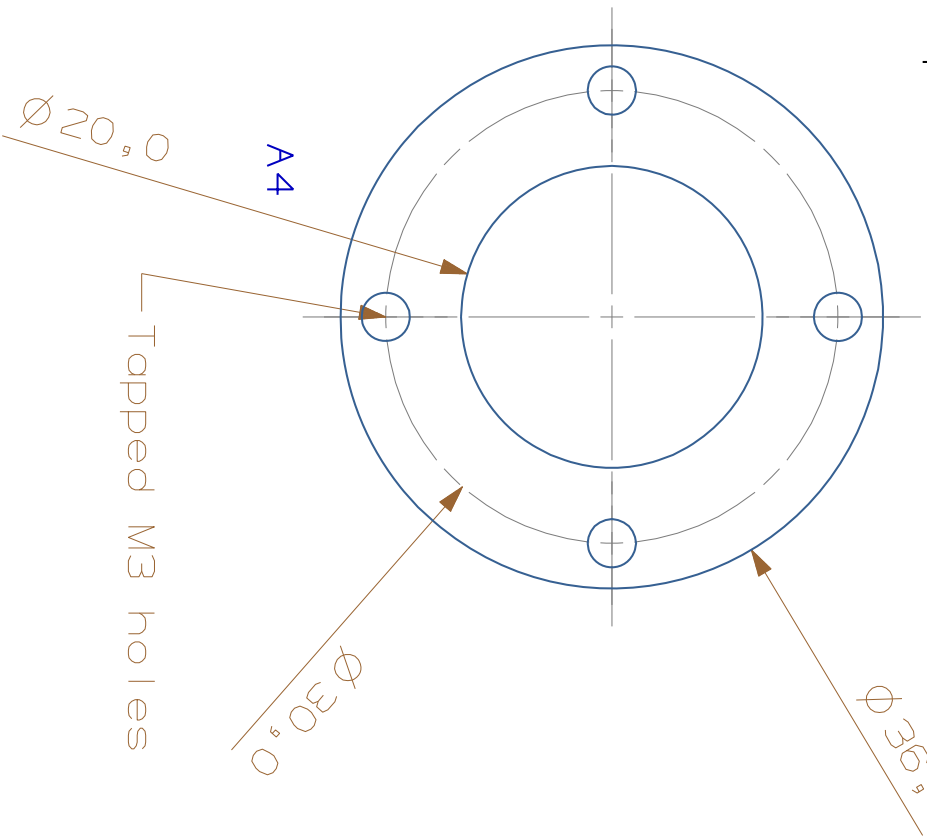
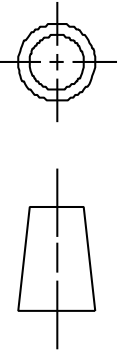
CCD

PROJECT tapped_gas_inlet_flange

DRG NO

DRG. NO.

A4



SCALE 2:1		DIMENSIONS ARE IN MILLIMETERS	
DRAWN	LGML	DATE	13-12-13
DESIGNED	LGML	13-12-13	TOLERANCE EXCEPT WHERE STATED OTHERWISE
CHECKED	#NAME#	#DATE#	± 0.1
APPROVED	#NAME#	#DATE#	

SHEET 1 OF 1	
USED ON	#USED ON#
DRAWING TYPE	#DRAWING TYPE#
MATERIAL	SS
FINISH	#FINISH#

ISSUE	A	DATE	#DATE#	INITIAL	ISSUE	DRAWN	#NAME#
				AMENDMENT		APPROVED	#NAME#

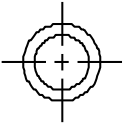


University of Leicester

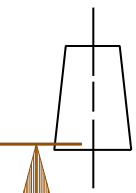
PROJECT
CCD

TITLE
tapped_ring

DRG. NO.
#DRG NO#



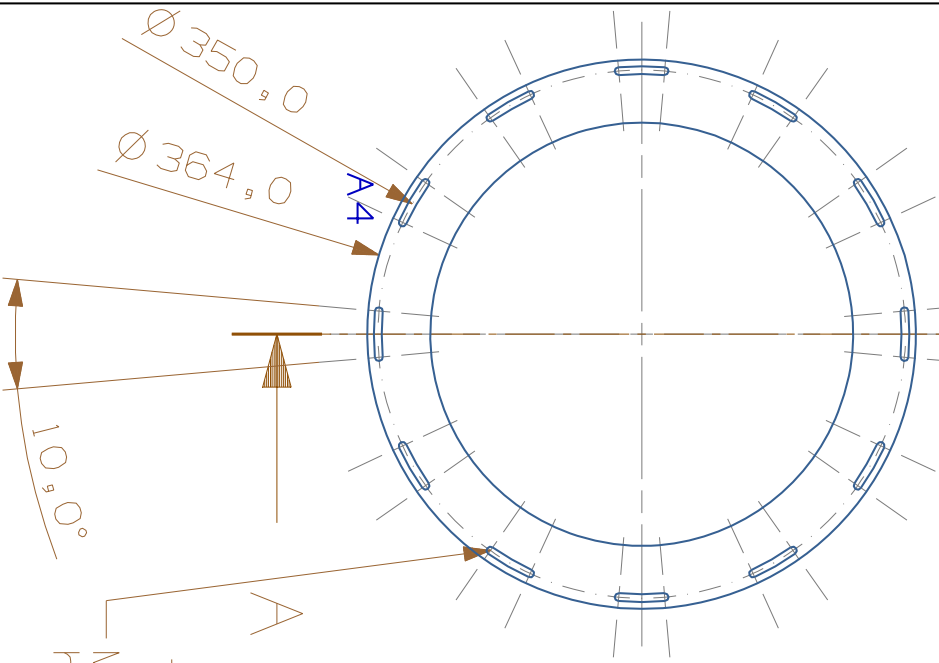
SECTION A - A



A

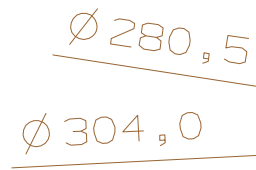
Groove for O-ring.
 ID: 285.0
 OD: 299.4
 Depth: 3.30

Tapped M4 holes.
 Depth: 10

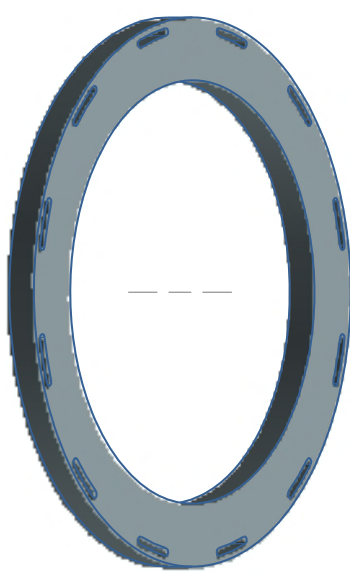


M5 slotted holes

20.0



The groove sides need a finish of 1.6µm and the bore needs 0.8µm finish. Radii in the corners need to be R 0.5-0.00+0.50



SCALE 1:5	DIMENSIONS ARE IN MILLIMETERS	
DRAWN LGML	DATE 13-12-13	DO NOT SCALE
DESIGNED LGML	13-12-13	TOLERANCE EXCEPT WHERE STATED OTHERWISE
CHECKED #NAME#	#DATE#	±0.1
APPROVED #NAME#	#DATE#	

SHEET 1 OF 1	
USED ON	#USED ON#
DRAWING TYPE	#DRAWING TYPE#
MATERIAL SS	
FINISH	#FINISH#

ISSUE A	#DATE#	INITIAL ISSUE	DRAWN #NAME#
DATE		AMENDMENT	APPROVED #NAME#
PROJECT CCD		UNIVERSITY OF LEICESTER	
TITLE Vacuum-chamber-adapter		#DRG NO#	
DRG. NO.			

Bibliography

- [1] Macor: Machinable glass ceramic for industrial applications. http://www.professionalplastics.com/professionalplastics/content/downloads/Macor_Brochure_2014.pdf. Retrieved on 7 July, 2015.
- [2] *Omega pressure transducers catalog*. Omega Engineering.
- [3] *Heliox AC-V ^3He Refrigerator. System manual*. Oxford Instruments, 2005.
- [4] *Temperature Measurement and Control Catalog. Lake Shore Cryotronics Product Catalog*. Lake Shore Cryotronics, 2013.
- [5] ABRAMOWITZ, M., AND STEGUN, I. A. *Handbook of Mathematical Functions*. Dover, New York, 1970.
- [6] AITKEN, F. private communication.
- [7] AITKEN, F., BONIFACI, N., DENAT, A., AND VON HAEFTEN, K. A macroscopic approach to determine electron mobilities in low-density helium. *Journal of Low Temperature Physics* 162, 5-6 (2011), 702–709.
- [8] AITKEN, F., BONIFACI, N., MENDOZA-LUNA, L. G., AND VON HAEFTEN, K. Modelling the mobility of positive ion clusters in normal liquid helium over large pressure ranges. *Phys. Chem. Chem. Phys.* 17 (2015), 18535–18540.
- [9] AITKEN, F., LI, Z.-L., BONIFACI, N., DENAT, A., AND VON HAEFTEN, K. Electron mobility in liquid and supercritical helium measured using corona discharges: a new semi-empirical model for cavity formation. *Phys. Chem. Chem. Phys.* 13 (2011), 719–724.
- [10] ALLARD, N. F., DEGUILHEM, B., GADEA, F. X., BONIFACI, N., AND DENAT, A. Analysis of the He($3\ ^3\text{S}$)-He($2\ ^3\text{P}$) line profile obtained in dense helium plasma. *EPL (Europhysics Letters)* 88, 5 (2009), 53002.
- [11] ALLEN, J. F., AND JONES, H. New phenomena connected with heat flow in helium II. *Nature* 141 (1938), 243.
- [12] ANDRONIKASHVILI, E. L. *J. Phys. USSR* 10 (1946), 201.
- [13] ANNETT, J. F. *Superconductivity, Superfluids and Condensates*. Oxford University Press, 2007.
- [14] ARFKEN, G. B., WEBER, H. J., AND HARRIS, F. E., Eds. *Mathematical Methods for Physicists*, seventh ed. Academic Press, 2013.

- [15] ARNOT, F. L., AND M'EWEN, M. B. The formation of helium molecules. *Proceedings of the Royal Society of London. Series A, Mathematical and Physical Sciences* 166, 927 (1938), pp. 543–551.
- [16] ARNOT, F. L., AND M'EWEN, M. B. The formation of helium molecules. II. *Proceedings of the Royal Society of London. Series A, Mathematical and Physical Sciences* 171, 944 (1939), pp. 106–120.
- [17] ATKINS, K. R. Ions in liquid helium. *Phys. Rev.* 116 (Dec 1959), 1339–1343.
- [18] ATKINS, P., AND DE PAULA, J. *Physical Chemistry*, 8th revised ed. Oxford University Press, Mar. 2006.
- [19] BENDERSKII, A. V., ZADOYAN, R., SCHWENTNER, N., AND APKARIAN, V. A. Photodynamics in superfluid helium: Femtosecond laser-induced ionization, charge recombination, and preparation of molecular Rydberg states. *The Journal of Chemical Physics* 110, 3 (1999), 1542–1557.
- [20] BENNEMANN, K.-H., AND KETTERSON, J. B. *Novel superfluids. Volume 1.* International series of monographs on physics. Oxford Univ. Press, Oxford, 2013.
- [21] BIRKS, J. B. Excimers. *Reports on Progress in Physics* 38, 8 (1975), 903.
- [22] BLANK, C., AND EDWARDS, M. H. Dielectric breakdown of liquid helium. *Phys. Rev.* 119 (Jul 1960), 50–52.
- [23] BOLES, Y. A., AND ÇENGEL, M. A. *Thermodynamics: an engineering approach*, fifth ed. New York: McGraw-Hill, 2006.
- [24] BORGHESEANI, A. F. *Ions and Electrons in Liquid Helium*, first ed. Oxford Science Publications, 2007.
- [25] BROOKS, R. L., AND HUNT, J. L. Helium emission spectra from doped samples of solid hydrogen and deuterium. *The Journal of Chemical Physics* 88, 12 (1988), 7267–7272.
- [26] COELHO, R., AND DEBEAU, J. Properties of the tip-plane configuration. *Journal of Physics D: Applied Physics* 4, 9 (1971), 1266.
- [27] CZERNY, M., AND TURNER, A. Über den astigmatismus bei spiegelspektrometern. *Zeitschrift für Physik* 61, 11-12 (1930), 792–797.
- [28] DENNIS, W. S., DURBIN, E., FITZSIMMONS, W. A., HEYBEY, O., AND WALTERS, G. K. Spectroscopic identification of excited atomic and molecular states in electron-bombarded liquid helium. *Phys. Rev. Lett.* 23 (Nov 1969), 1083–1086.
- [29] ELORANTA, J., AND APKARIAN, V. A. The triplet He_2^* Rydberg states and their interaction potentials with ground state He atoms. *The Journal of Chemical Physics* 115, 2 (2001), 752–760.
- [30] FEYNMAN, R. P. Superfluidity and superconductivity. *Rev. Mod. Phys.* 29 (Apr 1957), 205–212.

- [31] FIEDLER, S., AND ELORANTA, J. Interaction of helium Rydberg state atoms with superfluid helium. *Journal of Low Temperature Physics* 174, 5-6 (2014), 269–283.
- [32] FONTANA, P. R. Spin-orbit and spin-spin interactions in diatomic molecules. I. Fine structure of H₂. *Phys. Rev.* 125 (Jan 1962), 220–228.
- [33] FROCHTENICHT, R., TOENNIES, J., AND VILESOV, A. High-resolution infrared spectroscopy of SF₆ embedded in He clusters. *Chemical Physics Letters* 229, 12 (1994), 1 – 7.
- [34] GAO, J., MARAKOV, A., GUO, W., PAWLOWSKI, B. T., VAN SCIVER, S. W., IHAS, G. G., MCKINSEY, D. N., AND VINEN, W. F. Producing and imaging a thin line of He₂^{*} molecular tracers in helium-4. *Review of Scientific Instruments* 86, 9 (2015), 093904.
- [35] GASIOROWICZ, S. *Quantum Physics*, third ed. John Wiley & Sons, 2003.
- [36] GERHOLD, J. Dielectric breakdown of helium at low temperatures. *Cryogenics* 12, 5 (1972), 370 – 376.
- [37] GIANNUZZI, L. A., Ed. *Introduction to Focused Ion Beams. Instrumentation, Theory, Techniques and Practice*. Springer US, 2005.
- [38] GINTER, M. L. Spectrum and structure of the He₂ molecule. I. Characterization of the states associated with the UAO's 3pσ and 2s. *The Journal of Chemical Physics* 42, 2 (1965), 561–568.
- [39] GINTER, M. L. The spectrum and structure of the He₂ molecule: Part II. Characterization of the singlet states associated with the UAO's 3s and 2pπ. *Journal of Molecular Spectroscopy* 17, 2 (1965), 224 – 239.
- [40] GINTER, M. L. The spectrum and structure of the He₂ molecule: Part III. Characterization of the triplet states associated with the UAO's 3s and 2pπ. *Journal of Molecular Spectroscopy* 18, 3 (1965), 321 – 343.
- [41] GINTER, M. L., AND BATTINO, R. Potential-energy curves for the He₂ molecule. *The Journal of Chemical Physics* 52, 9 (1970), 4469–4474.
- [42] GOLDMAN, M., GOLDMAN, A., AND SIGMOND, R. S. The corona discharge, its properties and specific uses. *Pure and Applied Chemistry* 57, 9 (1985), 1353–1362.
- [43] GOLDSTEIN, H. *Classical mechanics*. World student series. Addison-Wesley, Reading (Mass.), Menlo Park (Calif.), Amsterdam, 1980.
- [44] GOUGH, T. E., MENGEL, M., ROWNTREE, P. A., AND SCOLES, G. Infrared spectroscopy at the surface of clusters: SF₆ on Ar. *The Journal of Chemical Physics* 83, 10 (1985), 4958–4961.
- [45] GOYAL, S., ROBINSON, G. N., SCHUTT, D. L., AND SCOLES, G. Infrared spectroscopy of sulfur hexafluoride in and on argon clusters in an extended range of cluster sizes: finite-size particles attaining bulklike properties. *The Journal of Physical Chemistry* 95, 11 (1991), 4186–4189.

- [46] GOYAL, S., SCHUTT, D. L., AND SCOLES, G. Vibrational spectroscopy of sulfur hexafluoride attached to helium clusters. *Phys. Rev. Lett.* *69* (Aug 1992), 933–936.
- [47] GRAU, V., BARRANCO, M., MAYOL, R., AND PI, M. Electron bubbles in liquid helium: Density functional calculations of infrared absorption spectra. *Phys. Rev. B* *73* (Feb 2006), 064502.
- [48] GREBENEV, S., TOENNIES, J. P., AND VILESOV, A. F. Superfluidity within a small helium-4 cluster: The microscopic Andronikashvili experiment. *Science* *279*, 5359 (1998), 2083–2086.
- [49] GRIFFITHS, O. J., HENDRY, P. C., MCCLINTOCK, P. V. E., AND NICHOL, H. A. *Liquid ^4He and its superfluidity*. Department of Physics, Lancaster University.
- [50] GRIMES, C. C., AND ADAMS, G. Infrared-absorption spectrum of the electron bubble in liquid helium. *Phys. Rev. B* *45* (Feb 1992), 2305–2310.
- [51] HARMS, J., HARTMANN, M., TOENNIES, J., VILESOV, A. F., AND SARTAKOV, B. Rotational structure of the IR spectra of single SF_6 molecules in liquid ^4He and ^3He droplets. *Journal of Molecular Spectroscopy* *185*, 1 (1997), 204 – 206.
- [52] HARTMANN, M., MIELKE, F., TOENNIES, J. P., VILESOV, A. F., AND BENEDEK, G. Direct spectroscopic observation of elementary excitations in superfluid He droplets. *Phys. Rev. Lett.* *76* (Jun 1996), 4560–4563.
- [53] HARTMANN, M., MILLER, R. E., TOENNIES, J. P., AND VILESOV, A. Rotationally resolved spectroscopy of SF_6 in liquid helium clusters: A molecular probe of cluster temperature. *Phys. Rev. Lett.* *75* (Aug 1995), 1566–1569.
- [54] HARTMANN, M., MILLER, R. E., TOENNIES, J. P., AND VILESOV, A. F. High-resolution molecular spectroscopy of van der Waals clusters in liquid helium droplets. *Science* *272*, 5268 (1996), 1631–1634.
- [55] HERZBERG, G. *Molecular spectra and Molecular Structure. Vol. I: Spectra of Diatomic Molecules*, second ed. Krieger Publishing Company, 1950.
- [56] HICKMAN, A. P., AND LANE, N. F. Localized excited states of helium in liquid helium. *Phys. Rev. Lett.* *26* (May 1971), 1216–1219.
- [57] HICKMAN, A. P., STEETS, W., AND LANE, N. F. Nature of excited helium atoms in liquid helium: A theoretical model. *Phys. Rev. B* *12* (Nov 1975), 3705–3717.
- [58] HILL, J. C., HEYBEY, O., AND WALTERS, G. K. Evidence of metastable atomic and molecular bubble states in electron-bombarded superfluid liquid helium. *Phys. Rev. Lett.* *26* (May 1971), 1213–1216.
- [59] HIROIKE, K., KESTNER, N. R., RICE, S. A., AND JORTNER, J. Study of the properties of an excess electron in liquid helium. II. A refined description of configuration changes in the liquid. *The Journal of Chemical Physics* *43*, 8 (1965), 2625–2632.

- [60] HODBY, E. *The Superfluid Properties of a Bose-Einstein Condensed Gas*. PhD thesis, University of Oxford, 2002.
- [61] HOLLAS, J. M. *Modern Spectroscopy*. John Wiley & Sons, Ltd, 2004.
- [62] HORNBECK, J. A., AND MOLNAR, J. P. Mass spectrometric studies of molecular ions in the noble gases. *Phys. Rev.* *84* (Nov 1951), 621–625.
- [63] HUBER, K. P., AND HERZBERG, G. *Molecular Spectra and Molecular Structure IV. Constants of Diatomic Molecules*. Van Nostrand Reinhold, New York, 1950.
- [64] INGUSCIO, M., STRINGARI, S., AND WIEMAN, C. E., Eds. *Bose-Einstein Condensation in Atomic Gases: Proceedings of the International School of Physics Enrico Fermi. Course CXL*. Società Italiana di Fisica, 1999.
- [65] JORTNER, J., KESTNER, N. R., RICE, S. A., AND COHEN, M. H. Study of the properties of an excess electron in liquid helium. I. The nature of the electron-helium interactions. *The Journal of Chemical Physics* *43*, 8 (1965), 2614–2625.
- [66] KAPITZA, P. L. Viscosity of liquid helium below the λ -point. *Nature* *141* (1938), 74.
- [67] KESTNER, N. R., AND SINANOLU, O. Intermolecular-potential-energy curve-theory and calculations on the helium-helium potential. *The Journal of Chemical Physics* *45*, 1 (1966), 194–207.
- [68] KETO, J. W., SOLEY, F. J., STOCKTON, M., AND FITZSIMMONS, W. A. Dynamic properties of neutral excitations produced in electron-bombarded superfluid helium. II. Afterglow fluorescence of excited helium molecules. *Phys. Rev. A* *10* (Sep 1974), 887–896.
- [69] KITTEL, C., AND KROEMER, H. *Thermal physics*, second ed. W. H. Freeman, 1980.
- [70] KOVÁCS, I. *Rotational Structure in the spectra of diatomic molecules*. Adam Higer Ltd., 1969.
- [71] KRAMERS, H. Zur struktur der multiplett-S-zustände in zweiatomigen molekülen. I. *Zeitschrift für Physik* *53*, 5-6 (1929), 422–428.
- [72] KRAMIDA, A., YU. RALCHENKO, READER, J., AND NIST ASD TEAM. NIST Atomic Spectra Database (ver. 5), [Online]. Available: <http://physics.nist.gov/asd> [2015, January 7]. National Institute of Standards and Technology, Gaithersburg, MD., 2014.
- [73] KUPER, C. G. Theory of negative ions in liquid helium. *Phys. Rev.* *122* (May 1961), 1007–1011.
- [74] KUPPER, J., AND MERRITT, J. M. Spectroscopy of free radicals and radical containing entrance-channel complexes in superfluid helium nanodroplets. *International Reviews in Physical Chemistry* *26*, 2 (2007), 249–287.

- [75] KWON, Y., HUANG, P., PATEL, M. V., BLUME, D., AND WHALEY, K. B. Quantum solvation and molecular rotations in superfluid helium clusters. *The Journal of Chemical Physics* 113, 16 (2000), 6469–6501.
- [76] LANDAU, L. The theory of superfluidity of helium II. *J. Phys. USSR* 5, 1 (1941), 71–90.
- [77] LANDAU, L. Theory of the superfluidity of helium II. *Phys. Rev.* 60 (Aug 1941), 356–358.
- [78] LANDAU, L. D., AND LIFSHITZ, E. M. *Fluid Mechanics. Volume 6 of Course of Theoretical Physics*. Pergamon Press, 1987.
- [79] LEMMON, E. W., MCLINDEN, M. O., AND FRIEND, D. G. Thermophysical Properties of Fluid Systems. In *NIST Chemistry WebBook, NIST Standard Reference Database Number 69*, P. J. Linstrom and W. G. Mallard, Eds. National Institute of Standards and Technology, Gaithersburg MD, 20899. <http://webbook.nist.gov>, retrieved (July 3, 2015).
- [80] LI, Z. *Décharge couronne dans l'hélium liquide et gaz dense dans champ intense: pré-claquage, transport de charge, spectroscopie d'émission*. PhD thesis, Université Joseph Fourier, 2008.
- [81] LI, Z.-L., BONIFACI, N., AITKEN, F., DENAT, A., VON HAEFTEN, K., ATRAZHEV, V. M., AND SHAKHATOV, V. A. Spectroscopic investigation of liquid helium excited by a corona discharge: evidence for bubbles and red satellites. *The European Physical Journal Applied Physics* 47 (8 2009), 22821.
- [82] LI, Z. L., BONIFACI, N., DENAT, A., ATRAZHEV, V. M., AND SHAKHATOV, V. A. Spectroscopic study of the negative corona discharge in the liquid 4He . *AIP Conference Proceedings* 874, 1 (2006), 217–220.
- [83] MANDRU, A. Tungsten tip preparation. <http://www.phy.ohiou.edu/~asmith/lab/stm-tip-prep.pdf>.
- [84] MARQUARDT, E., LE, J., AND RADEBAUGH, R. Cryogenic material properties database. In *Cryocoolers 11*, J. Ross, R.G., Ed. Springer US, 2002, pp. 681–687.
- [85] MC CARTY, R. D. Thermodynamic properties of helium 4 from 2 to 1500 k at pressures to 108 pa. *Journal of Physical and Chemical Reference Data* 2, 4 (1973), 923–1042.
- [86] MILLER, R. E. Spiers memorial lecture. Comparative studies of cluster dynamics in the gas and condensed phases. *Faraday Discuss.* 118 (2001), 1–17.
- [87] MULLIKEN, R. S. The Rydberg states of molecules. 1a parts I-VIb. *Journal of the American Chemical Society* 86, 16 (1964), 3183–3197.
- [88] NEESER, S., TIETZ, R., SCHULZ, M., AND LANGHOFF, H. Lifetime of the $\text{He}_2(e)$, $\text{He}_2(d)$ and $\text{He}_2(f)$ states. *Zeitschrift für Physik D Atoms, Molecules and Clusters* 31, 1 (1994), 61–65.

- [89] PAGE, D., PRAKASH, M., LATTIMER, J. M., AND STEINER, A. W. Rapid cooling of the neutron star in Cassiopeia A triggered by neutron superfluidity in dense matter. *Phys. Rev. Lett.* 106 (Feb 2011), 081101.
- [90] POBELL, F. *Matter and Methods at Low Temperatures*, third ed. Springer-Verlag Berlin Heidelberg, 2007.
- [91] RADZIG, A. A., AND SMIRNOV, B. M. *Reference Data on Atoms, Molecules, and Ions*. Springer-Verlag, 1985.
- [92] RINCÓN-LIÉBANA, R. Certificado de realización de estancia breve. Tech. rep., 2011.
- [93] SANSONETTI, J. E., AND MARTIN, W. C. Handbook of basic atomic spectroscopic data. *Journal of Physical and Chemical Reference Data* 34, 4 (2005), 1559–2259.
- [94] SARTAKOV, B. G., TOENNIES, J. P., AND VILESOV, A. F. Infrared spectroscopy of carbonyl sulfide inside a pure ^3He droplet. *The Journal of Chemical Physics* 136, 13 (2012), 134316.
- [95] SCHLAPP, R. Fine structure in the $^3\Sigma$ ground state of the oxygen molecule, and the rotational intensity distribution in the atmospheric oxygen band. *Phys. Rev.* 51 (Mar 1937), 342–345.
- [96] SIGMOND, R. S. Simple approximate treatment of unipolar space-charge-dominated coronas: The Warburg law and the saturation current. *Journal of Applied Physics* 53, 2 (1982), 891–898.
- [97] SOLEY, F. J., AND FITZSIMMONS, W. A. Pressure shifts and quenching of atomic and molecular states produced in electron-bombarded liquid helium. *Phys. Rev. Lett.* 32 (May 1974), 988–991.
- [98] SPIVAK, M. *Calculus*. Cambridge University Press, 1994.
- [99] SU, J. F., AND NICOL, J. L. Pressure shift of the helium triplet line lambda 706.5 nm. *Journal of Physics B: Atomic, Molecular and Optical Physics* 26, 2 (1993), 255.
- [100] SURIN, L. A., POTAPOV, A. V., DUMESH, B. S., SCHLEMMER, S., XU, Y., RASTON, P. L., AND JÄGER, W. Rotational study of carbon monoxide solvated with helium atoms. *Phys. Rev. Lett.* 101 (Dec 2008), 233401.
- [101] SURKO, C. M., AND REIF, F. Investigation of a new kind of energetic neutral excitation in superfluid helium. *Phys. Rev.* 175 (Nov 1968), 229–241.
- [102] TANAKA, Y., AND YOSHINO, K. Absorption spectrum of the He_2 molecule in the 510–611 Å range. *The Journal of Chemical Physics* 50, 7 (1969), 3087–3098.
- [103] TARCHOUNA, H. G., BONIFACI, N., AITKEN, F., MENDOZA LUNA, L. G., AND HAEFTEN, K. V. Formation of positively charged liquid helium clusters in supercritical helium and their solidification upon compression. *The Journal of Physical Chemistry Letters* 6 (2015), 3036–3040.

- [104] TISZA, L. Sur la théorie des liquides quantiques. Application a l'hélium liquide. *J. Phys. Radium* 1, 5 (1940), 164–172.
- [105] TOENNIES, J. P., AND VILESOV, A. F. Superfluid helium droplets: A uniquely cold nanomatrix for molecules and molecular complexes. *Angewandte Chemie International Edition* 43, 20 (2004), 2622–2648.
- [106] TOKARYK, D. W., WAGNER, G. R., BROOKS, R. L., AND HUNT, J. L. Infrared emission spectra from cryogenic proton-irradiated helium gas. *The Journal of Chemical Physics* 103, 24 (1995), 10439–10444.
- [107] TÜXEN, O. Massenspektrographische untersuchungen negativer ionen in gasentladungen bei höheren drucken. *Zeitschrift für Physik* 103, 7-8 (1936), 463–484.
- [108] VON HAEFTEN, K. *Struktur und Energielaxation elektronisch angeregter ^3He - und ^4He -Cluster*. PhD thesis, Universität Hamburg, 1999.
- [109] VON HAEFTEN, K., DE CASTRO, A. R. B., JOPPIEN, M., MOUSSAVIZADEH, L., VON PIETROWSKI, R., AND MÖLLER, T. Discrete visible luminescence of helium atoms and molecules desorbing from helium clusters: The role of electronic, vibrational, and rotational energy transfer. *Phys. Rev. Lett.* 78 (Jun 1997), 4371–4374.
- [110] VON HAEFTEN, K., LAARMANN, T., WABNITZ, H., AND MÖLLER, T. Bubble formation and decay in ^3He and ^4He clusters. *Phys. Rev. Lett.* 88 (May 2002), 233401.
- [111] VON HAEFTEN, K., RUDOLPH, S., SIMANOVSKI, I., HAVENITH, M., ZIL- LICH, R. E., AND WHALEY, K. B. Probing phonon-rotation coupling in helium nanodroplets: Infrared spectroscopy of CO and its isotopomers. *Phys. Rev. B* 73 (Feb 2006), 054502.
- [112] WANG, C. A novel three-stage 4 K pulse tube cryocooler. In *Cryocoolers 14*, S. Miller and R. G. Ross, Jr., Eds. International Cryocooler Conference, 2007, pp. 163–169.
- [113] WELLENSTEIN, H. F., AND ROBERTSON, W. W. Collisional relaxation processes for the n=3 states of helium. II. Associative ionization. *The Journal of Chemical Physics* 56, 3 (1972), 1077–1082.
- [114] WHITE, G. K. *Experimental Techniques in Low-Temperature Physics*, third ed. Clarendon Press Oxford, 1979.
- [115] WHITEHEAD, S. *Dielectric phenomena Vol. 1. Electrical discharges in gases*. D. Van Nostrand, 1927.
- [116] WHITTLE, E., DOWS, D. A., AND PIMENTEL, G. C. Matrix isolation method for the experimental study of unstable species. *The Journal of Chemical Physics* 22, 11 (1954), 1943–1943.

- [117] WIKIMEDIA COMMONS, P. D. (unofficial) vacuum symbols library for svg schematics drawing. https://upload.wikimedia.org/wikipedia/commons/7/71/Vacuum_symbols_library.svg. Retrieved on 29th April, 2015.
- [118] WOODCRAFT, A. L. An introduction to cryogenics. <http://woodcraft.lowtemp.org>. Retrieved on 7th January, 2015.
- [119] YOUNG, D. A. *Phase Diagrams of the Elements*. University of California Press, 1991.